Supporting Information for: Modular Access to Nucleobase GFP-Surrogates: pH-Responsive Smart Probes for Ratiometric Nucleic Acid Diagnostics

Keenan T. Regan,[†#] Austin Pounder,[‡#] Ryan E. Johnson,[†] Makay T. Murray,[‡] Hannah X. Glowacki,[†] Stacey D. Wetmore,*[,‡] and Richard A. Manderville*[,†]

[†]Departments of Chemistry & Toxicology, University of Guelph, Guelph, Ontario, Canada N1G 2W1
[‡]Department of Chemistry & Biochemistry, University of Lethbridge, Lethbridge, Alberta, Canada T1K 3M4

List of Figures

List of Tables

Experimental.

Materials and Methods: Unless otherwise specified, all starting materials including, 6-hydroxy-indanone (6HI), morpholine, (*R*)-(+)-glycidol, DNA synthesis reagents and solvents and canonical phosphoramidites, aldehydes, unmodified oligonucleotides, and solvents were purchased and used as received from commercial sources. Buffers were prepared with their designated salts and ultra-pure water from an 18.2MΩ purification system. Neutralization to described pH was performed with 5M Aq. HCl/NaOH using a Thermo Orion 320 Basic PerpHect LogR pH meter. Modified oligonucleotides were synthesized on a 1 μmol scale with DMT-ON protection using an ABI394 DNA/RNA synthesizer with trityl monitor. To ensure the coupling of the modified oligonucleotide sequences, the 2'OMe RNA amidite coupling times were increased to 15 minutes, while the LNA modified amidites were allowed to couple for 6 minutes. Ultraviolet−visible (UV−Vis) spectra were obtained on a Cary 300-Bio UV−Vis spectrophotometer equipped with a 6 × 6 multicell block Peltier temperature control unit. Fluorescence measurements were acquired on either a Cary Eclipse Fluorescence spectrophotometer or an Edinburgh spectrofluorometer FS5 at ambient temperature. NMR spectra were recorded on Bruker Avance 300 or 400 MHz spectrometers at room temperature. Mass spectra were acquired on a Thermo Fisher LTQ XL Ion trap mass spectrometer using an electrospray ionization source (ESI) or on a Bruker Autoflex maX MALDI-TOF/TOF using 3-hydroxypropionic acid as the matrix. CD spectra were acquired using a Jasco J-815 CD spectrophotometer equipped with quartz cells (110-QS), featuring a 1 mm light path. Monitoring occurred within the range of 200 to 400 nm, employing a bandwidth of 1 nm and a scanning speed of 100 nm/min, all conducted at ambient temperature. A minimum of five scans were collected and averaged and the spectra were smoothed using the Jasco Spectra Analyzer software by Savitzky-Golay function with 19 convolutions.

On-Strand Aldol Condensations: Aldehyde stock solutions were prepared in DMSO to a concentration of 1 M. 20 μL of the aldehyde solution was combined with 40 μL of the modified oligo (~1 mM) containing the 6HI handle. To this mixture, 7.5 μL of morpholine was added and vortexed to ensure proper dispersal. The reaction mixture was heated at 70°C for ~4 hours with mixing via vortex every 1 hour. After the reaction was completed, the mixture was allowed to cool to room temperature. The DNA was precipitated by adding 20 μL of 5 M NaCl and 180 μL of absolute ethanol and allowing the solution to rest in a freezer (-20°C) overnight. After 1 hour of centrifugation at 13,400 RPM the supernatant was decanted and the oligo was allowed to air dry. The pellet was redissolved in 18.2 MΩ water and purified via HPLC.

Oligonucleotide Purification: Purification of oligos after solid-phase synthesis was performed using Glen-Pak DNA purification cartridges or RP-HPLC on an Agilent 1200 series HPLC system equipped with a diode array detector, fluorescence detector, autosampler, and fraction collector. HPLC purification was carried out at 70 °C using a 5 μm reversed phase semipreparative C18 column (100 × 10 mm^2) with a flow rate of 3.3 mL/min or a 8 μm PLRP-S column (7.5 × 150 mm^2) with a flow rate of 2.7 mL/min in various gradients of buffer A in buffer B (buffer A = 30:70 aqueous 50mM TEAA, pH 7.2/acetonitrile; buffer B = 95:5 aqueous 50 mM TEAA, pH 7.2/acetonitrile). Peaks showing high absorbance at both 254 nm (DNA) and 375-550 nm (chalcone modification) were collected. Yields were estimated using the relative integrals of product and reactant DNA peaks. Following purification, the collected samples were lyophilized to dryness and desalted using a Glen Gel-Pak (Glen Research) desalting column with elution in purified water. Samples were subsequently lyophilized to dryness and dissolved in 18.2 MW water for quantification by UV-vis measurements at three different concentrations. Molar absorption coefficients (ε_{260}) for native strands were obtained from the following website:

http://www.idtdna.com/analyzer/applications/oligoanalyzer. The ε_{260} value for native DNA was used to estimate the concentrations of the modified samples for determination of the molar absorption coefficient (ε_{max}) for the internal GFP-surrogate (absorbance at 390-450 nm ÷ concentration determined at 260 nm using ε_{260} for native strand). Purified samples were analyzed by ESI-MS or MALDI-TOF.

Thermal Melting and Spectroscopic Measurements: All fluorescent/UV−vis spectra and thermal melting measurements (T_m values) were carried out using a 10 mm light path quartz glass cells with a baseline correction. For thermal melting measurements, DNA stock solutions were diluted to 2 μM in binding buffer (1X PBS, pH 7.4 for *Narl*12 substrates, or 10 mM Tris·HCl pH 8.0, containing 50 mM KCl and 50 mM $MgCl_2$ for TBA15 substrates) to which 2 equivalent of complementary strand (FL DNA with cytosine opposite the probe, N-1 DNA or 2'-OMe-RNA) was added to afford duplex samples. UV absorbance was monitored at 260 nm for duplex samples or 295 nm for G-quadruplex samples as a function of temperature with five alternating ramps from 10−90 and 90−10 °C at a heating/cooling rate of 0.5 °C/min. Average T_m values were calculated using hyperchromicity calculations performed with the Varian Thermal melting software. Relative fluorescent quantum yields (Φ_{fl}) for the chalcone modification in duplex samples were determined at three different concentrations using the comparative method (following *Nat. Protoc*. **2013**, *8*, 1535-1550) using the fluorescent standards quinine sulfate (Φ_{fl} = 0.56) in 0.1 M H_2SO_4 for PhOH6HI and DiMePhOH6HI; perylene (Φ_{fl} = 0.94) in cyclohexane for NapOH6HI or coumarin 6 (Φ_{fl} = 0.78) in ethanol FPhOH6HI and DFPhOH6HI. Photophysical data for the probes free in solution were determined in spectroscopic grade methanol (ThermoFisher Scientific).

Phosphoramidite Synthesis: The 6HI-phosphoramidite (**3**, Scheme S1) needed for solid-phase insertion of the 6HI handle for on-strand Aldol condensation, was available in our laboratory or synthesized according to Scheme S1. Full synthetic details with NMR spectra (^1H, ^{13}C and ^{31}P) and HRMS analysis for compounds **1**, **2** and **3** have been previously published by us (*Chem. Sci*. **2023**, *14*, 4832–4844).

Scheme S1. Pathway for 6-hydroxy-indanone phosphoramidite synthesis.

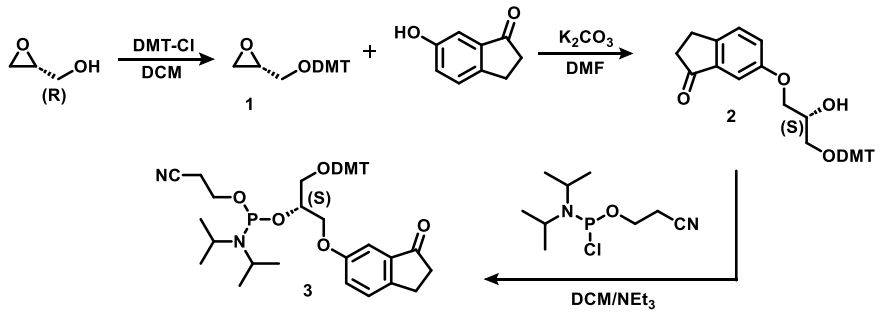

Free Dye Synthesis: All chalcone free dye surrogates were synthesized from 6-methoxyindanone (6MI, 0.5 mmol) and the appropriate aldehyde (0.5 mmol) in 5 mL of anhydrous ethanol. To the combined mixture, 5-7 drops of piperidine were added and the reaction mixture was allowed to reflux with constant stirring for 4-6 hours. After allowing to cool to room temperature, in all cases a free-flowing precipitate was observed within the reaction flask and was collected by vacuum filtration. The precipitate was washed with excess, ice-cold, ethanol. No further purification was needed for all dyes. In all cases, only the *E*-isomer was obtained, as evidenced by NMR.

PhOH6MI: ^{1}H NMR (400 MHz, DMSO-d_6): δ 10.14, 7.65 (d, 2H, *J* = 8.67 Hz), 7.57 (d, 2H, *J* = 8.21 Hz), 7.47 (m, 1H), 7.29 (dd, 1H, *J* = 8.47, 2.21 Hz), 7.24 (d, 1H, *J* = 2.42), 6.91 (d, 2H, *J* = 8.23 Hz), 3.97 (m, 2H), 3.84 (s, 3H). ^{13}C NMR (101 MHz, DMSO-d_6): δ 193.6, 159.9, 159.6, 142.8, 139.3, 133.7, 133.4, 132.8, 127.9, 126.4, 123.4, 116.5, 105.9, 55.9, 31.7 ppm. MS (ESI) m/z: $[M-H]^-$ calculated for $C_{17}H_{13}O_3$ = 265.09, found 265.07.

FPhOH6MI: ^{1}H NMR (400 MHz, DMSO-d_6): δ 10.56 (s, 1H), 7.61-7.57 (m, 2H), 7.48-7.45 (m, 2H), 7.29 (dd, 1H, *J* = 8.41, 2.59 Hz), 7.23 (d, 1H, *J* = 2.49 Hz), 7.07 (t, 1H, *J* = 8.68 Hz), 3.99 (m, 2H), 3.84 (s, 3H). ^{13}C NMR (101 MHz, DMSO-d_6): δ 193.5, 159.6, 152.6, 150.2, 147.5, 142.9, 139.1, 134.2, 132.6, 128.8, 127.9, 127.1, 123.7, 118.5, 105.9, 55.9, 31.5 ppm. ^{19}F NMR (282.4 MHz), DMSO-d_6): δ -135 (dd, 1F, *J* = 10.88, 3.18 Hz) ppm. MS (ESI) m/z: $[M-H]^-$ calculated for $C_{17}H_{12}FO_3$ = 283.08, found 283.07.

DFPhOH6MI: ^{1}H NMR (400 MHz, DMSO-d_6): δ 10.94 (s, 1H), 7.59 (d, 1H, *J* = 8.02 Hz), 7.54-7.48 (m, 2H), 7.44 (m, 1H), 7.31 (dd, 1H, *J* = 8.31, 2.65 Hz), 7.25 (d, 1H, *J* = 2.40 Hz), 4.03 (m, 2H), 3.84 (s, 3H). ^{13}C NMR (101 MHz, DMSO-d_6): δ 193.5, 159.6, 153.8, 151.1, 143.1, 138.9, 135.8, 131.6, 128.0, 125.9, 123.9, 114.7, 106.1, 55.9, 31.1 ppm. ^{19}F NMR (282.4 MHz), DMSO-d_6): δ -131 (d, 2F, *J* = 9.4 Hz) ppm. MS (ESI) m/z: $[M-H]^-$ calculated for $C_{17}H_{11}F_2O_3$ = 301.07, found 301.05.

DMePhOH6MI: ^{1}H NMR (400 MHz, DMSO-d_6): δ 7.59 (d, 1H, *J* = 8.21 Hz), 7.39 (m, 3H), 7.28 (dd, 1H, *J* = 8.23, 3.04), 7.22 (d, 1H, *J* = 2.43 Hz), 3.97 (m, 2H), 3.84 (s, 3H), 2.24 (s, 6H). ^{13}C NMR (101 MHz, DMSO-d_6): δ 193.5, 159.6, 156.1, 142.8, 139.4, 134.0, 132.7, 132.1, 127.9, 126.4, 125.2, 123.3, 105.9, 55.9, 31.7, 31.1, 17.1 ppm. MS (ESI) m/z: $[M-H]^-$ calculated for $C_{19}H_{17}O_3$ = 293.12, found 293.12.

NapOH6MI: ^{1}H NMR (400 MHz, DMSO-d_6): δ 10.08 (s, 1H), 8.24 (s, 1H), 7.90 (d, 1H, *J* = 8.68 Hz), 7.79 (s, 2H,), 7.63 (m, 2H), 7.32 (dd, 1H, *J* = 8.38, 2.46 Hz), 7.27 (d, 1H, *J* = 2.52 Hz), 7.17 (m, 2H), 4.14 (m, 2H), 3.86 (s, 3H). ^{13}C NMR (101 MHz, DMSO-d_6): δ 193.6, 159.6, 157.5, 143.1, 139.2, 135.6, 135.0, 133.9, 132.2, 131.0, 129.9, 128.1, 127.9, 127.2, 123.7, 119.9, 109.3, 106.1, 55.9, 31.2 ppm. MS (ESI) m/z: $[M-H]^-$ calculated for $C_{21}H_{15}O_3$ = 315.10, found 315.11.

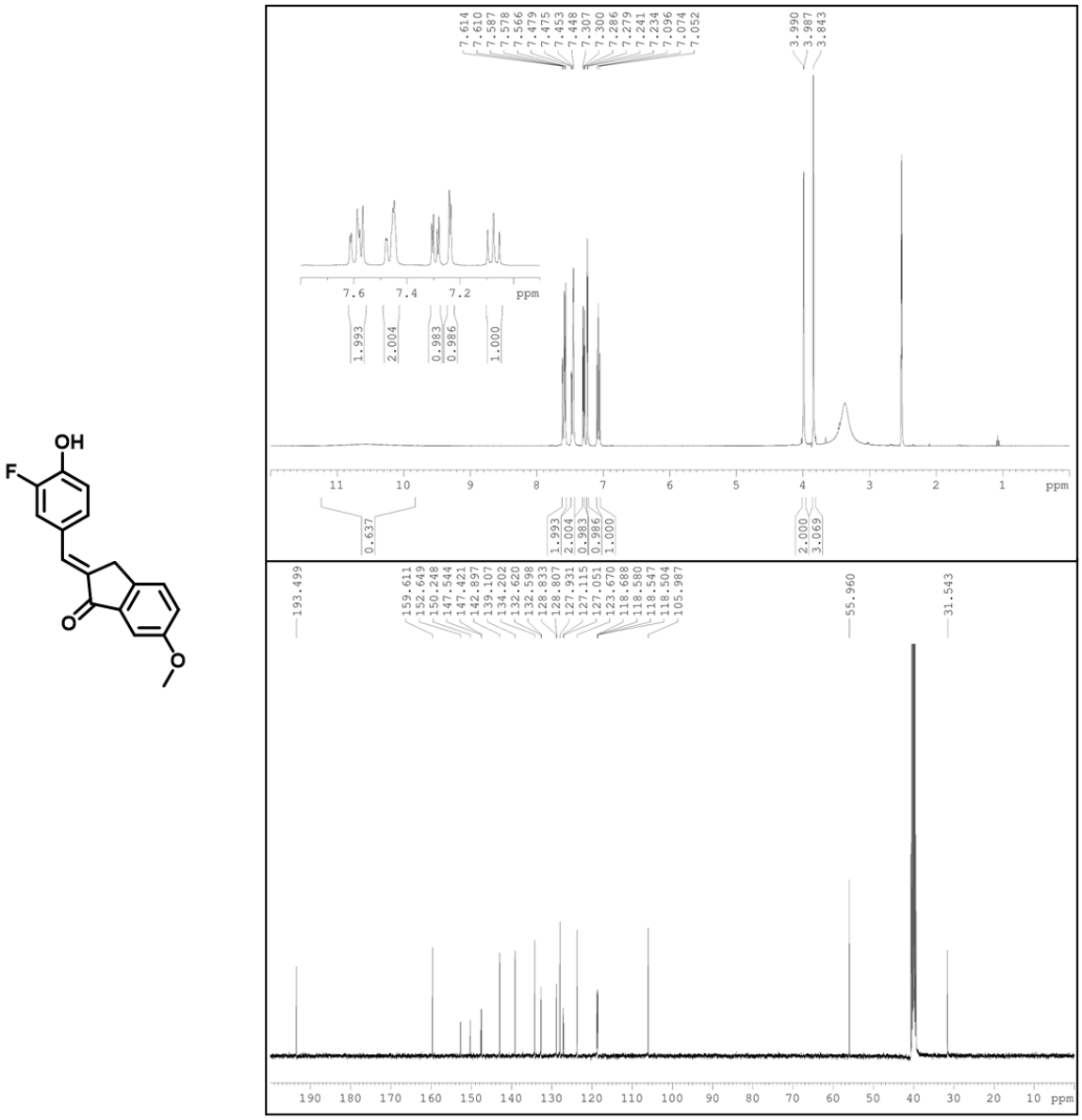

Figure S1. ^{1}H NMR (top) and ^{13}C NMR spectra (bottom) for FPhOH6MI (left structure) (400 MHz and 101 MHz spectra, respectively, in DMSO-d_6).

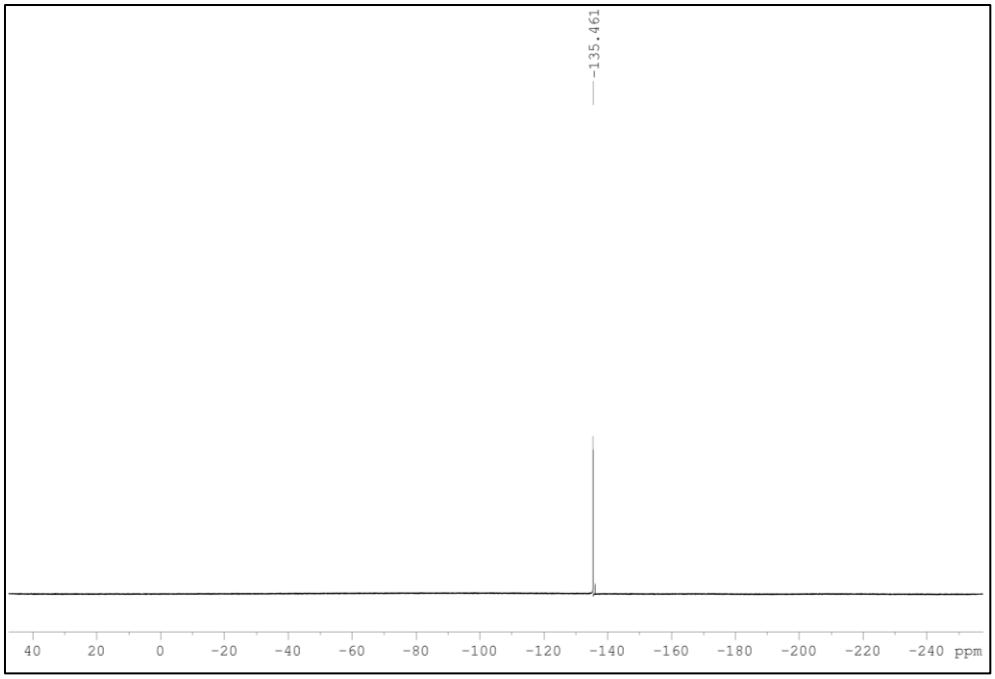

Figure S2. ^{19}F NMR for FPhOH6MI (282.4 MHz, DMSO-d_6)

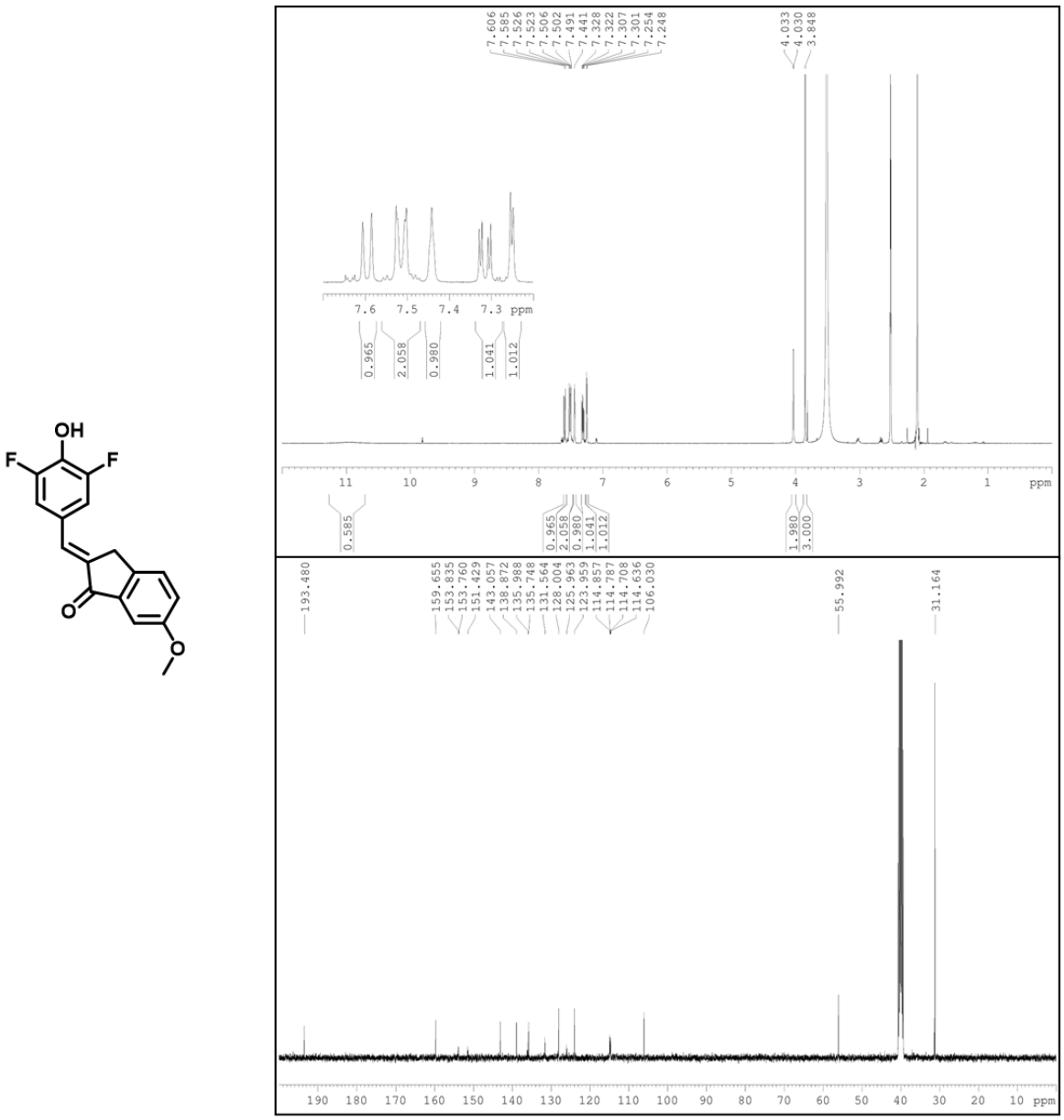

Figure S3. ^{1}H NMR (top) and ^{13}C NMR spectra (bottom) for DFPhOH6MI (left structure) (400 MHz and 101 MHz spectra, respectively, in DMSO-d_6).

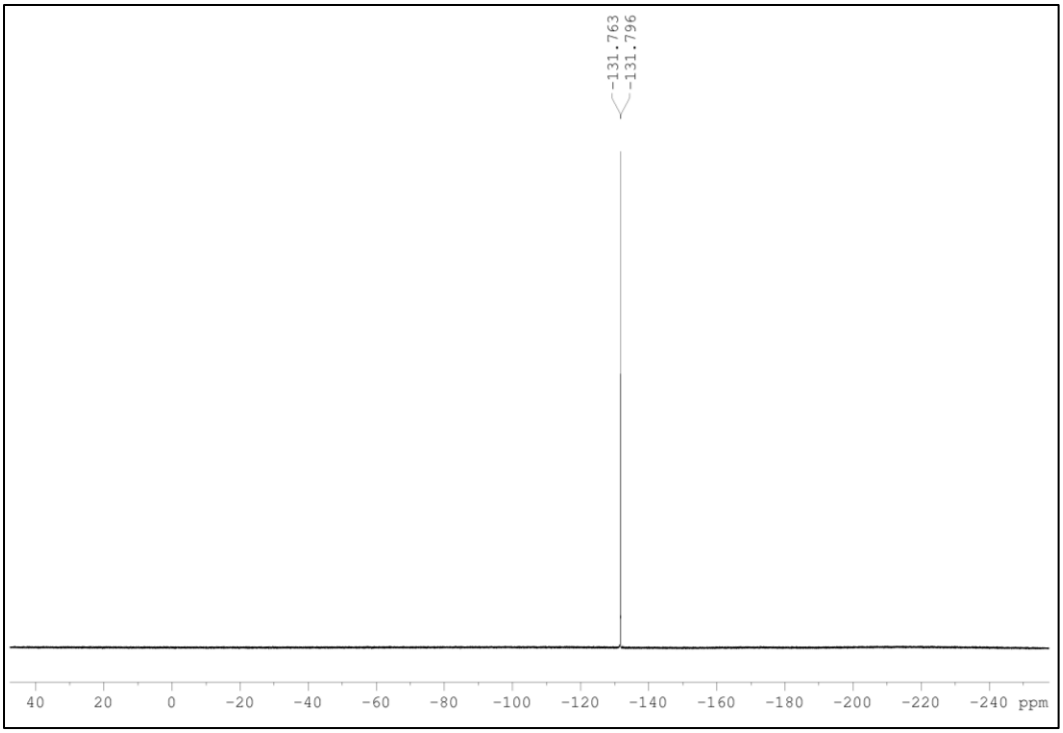

Figure S4: ^{19}F NMR for DFPhOH6MI (282.4 MHz, DMSO-d_6)

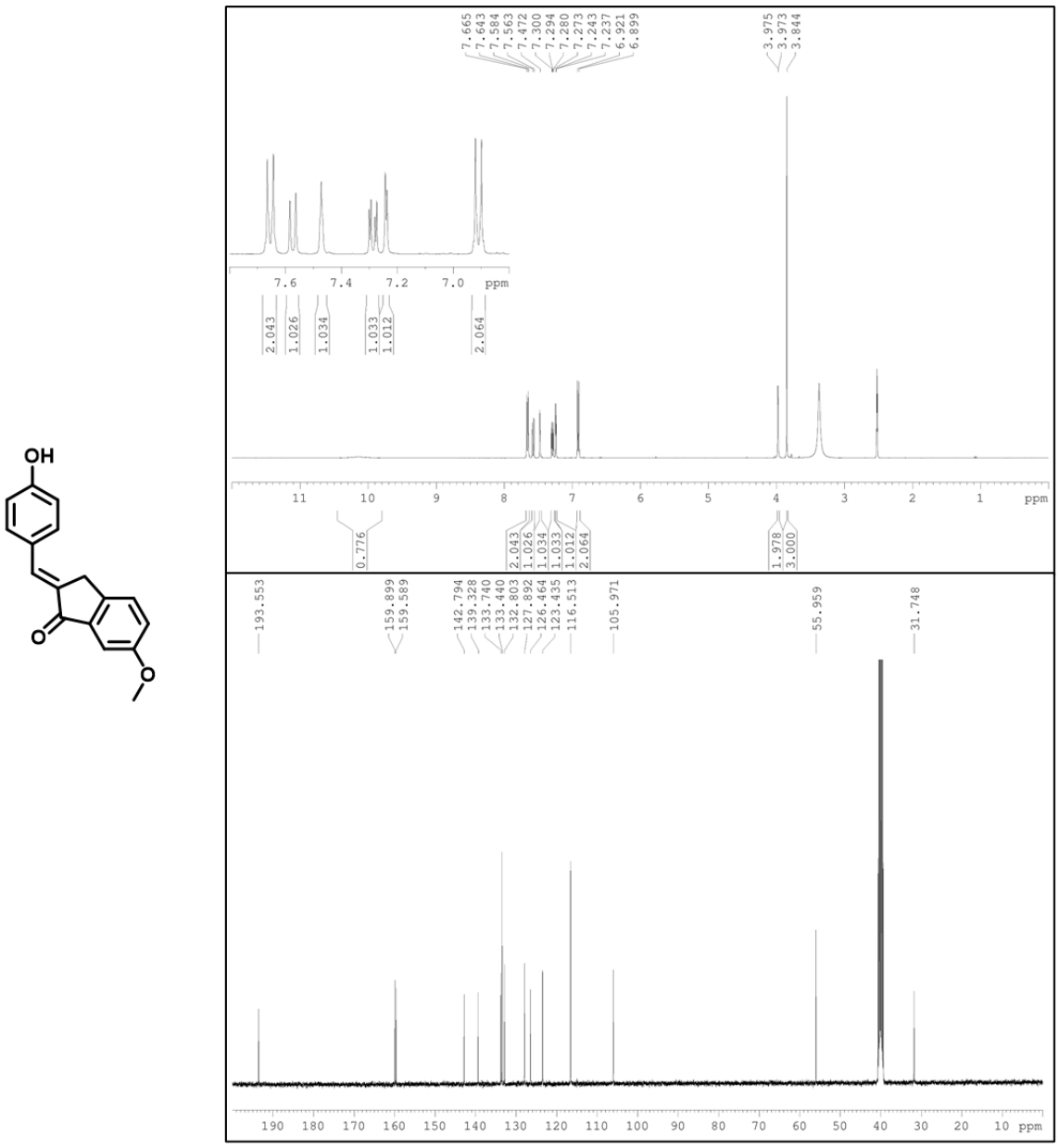

Figure S5. ^{1}H NMR (top) and ^{13}C NMR spectra (bottom) for PhOH6MI (left structure) (400 MHz and 101 MHz spectra, respectively, in DMSO-d_6).

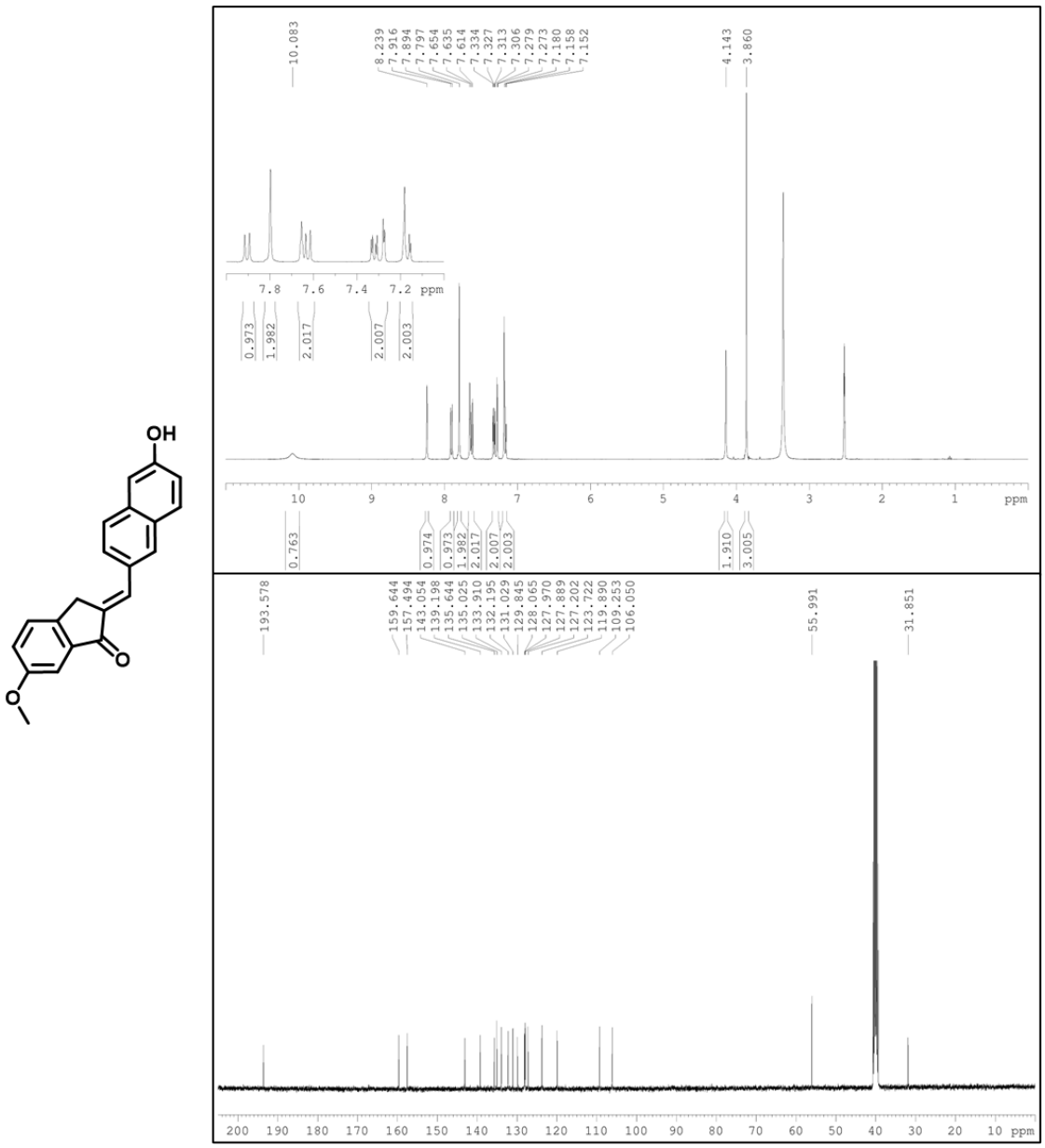

Figure S6. ^{1}H NMR (top) and ^{13}C NMR spectra (bottom) for 6-OH-2-Nap6MI (left structure) (400 MHz and 101 MHz spectra, respectively, in DMSO-d_6).

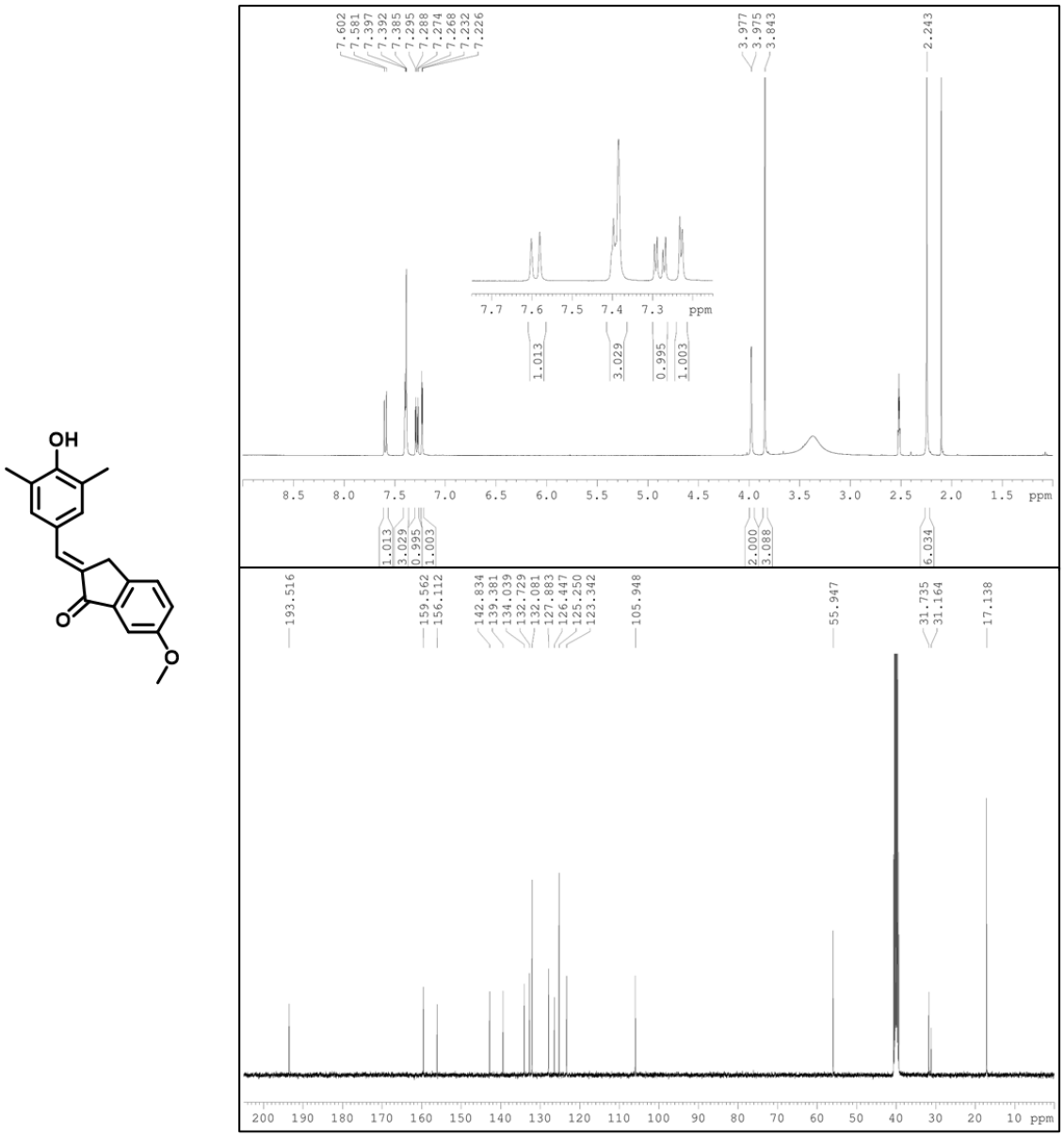

Figure S7. ^{1}H NMR (top) and ^{13}C NMR spectra (bottom) for DMePhOH6MI (left structure) (400 MHz and 101 MHz spectra, respectively, in DMSO-d_6).

Table S1. Photophysical Properties of O-Donor-6MI Chalcones.

Donor	ROH $\lambda_{max}/\varepsilon_{max}$[a] nm/cm^{-1}M^{-1}	RO$^-$ $\lambda_{max}/\varepsilon_{max}$[a] nm/cm^{-1}M^{-1}	ROH* λ_{em} (nm)	RO$^-$* λ_{em} (nm)	pK_a (pK_a)[b]	pK_a*[c]	I_{rel}[d]
PhOH	373/32597	437/48194	471	556	8.26 (7.61)	1.15	8 (.20)
FPhOH	366/33094	430/47709	469	561	7.11 (6.52)	> 0	6 (.12)
DFPhOH	351/29703	425/43984	502	564	5.90 (5.27)	< 0	4 (.05)
DMePhOH	370/46786	472/67039	485	565	– (8.48)	> 0	12 (.25)
NapOH	390/45937	448/50800	538	698	– (8.60)	> 0	4 (1)

[a] Recorded in MeOH. [b] pK_a values for PhOH6MI, FPhOH6MI and DFPhOH6MI were obtained through UV-vis pH titrations in aqueous buffer at room temperature; values in brackets are from the literature for the parent aldehydes used to make the chalcone probes. [c] pK_a* value for PhO6MI was determined using the Förster cycle where pK_a* = pK_a – $NAhc$/2.303RT [$\tilde{\nu}$ArOH – $\tilde{\nu}$ArO–] in which the overlay of the fluorescence and absorbance spectra of the acidic and basic solutions are used to determine $\Delta\tilde{\nu}$. For the other probes their ability to undergo ESPT in MeOH dictated whether they have pK_a* values less than or greater than 0. Only DFPhOH6MI was able to undergo ESPT in MeOH. [d] Relative emission intensity in 25:75 MeOH:glycerol versus 100% MeOH; values in brackets represent relative emission in MeOH, in which the brightest probe was NapOH6MI with Φ_{fl} = 0.16 for B = (0.16)(45937) = 7,350 cm^{-1} M^{-1}, using perylene (Φ_{fl} = 0.94) in cyclohexane as fluorescent standard.

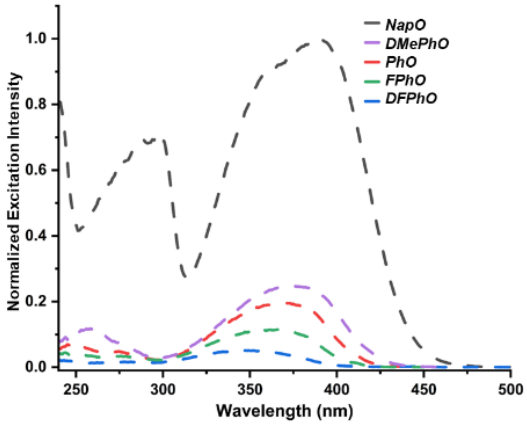

Figure S8. Normalized excitation spectra of 6-methoxy Indanone free dyes (10 μM) in MeOH

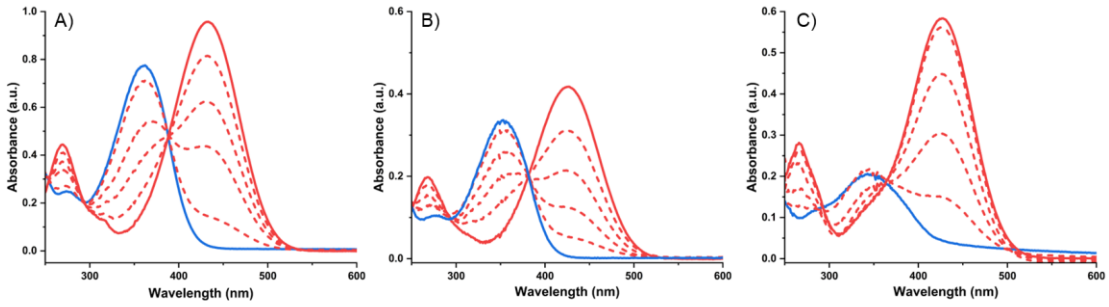

Figure S9. UV-Vis Spectra for pK_a determinations of free dyes, pH's ranging from 11.0 – 2.7. A) PhOH6MI B) FPhOH6MI C) DFPhOH6MI.

Table S2. Yields and MS Analysis of Modified *NarI* Oligonucleotides.

Oligo	On-Strand Yield (%)	Formula	Calc. Mass	Exptl (m/z) (ESI^-)	Exptl Mass
***NarI*FT 6HI**	-	$C_{118}H_{150}N_{35}O_{73}P_{11}$	3565.62	$[M-4H]^{4-}$ = 890.57	3566.28
***NarI*FT PhOH6HI**	49	$C_{125}H_{154}N_{35}O_{74}P_{11}$	3669.65	$[M-4H]^{4-}$ = 916.59	3670.36
***NarI*FT FPhOH6HI**	29	$C_{125}H_{153}FN_{35}O_{74}P_{11}$	3687.64	$[M-4H]^{4-}$ = 921.09	3688.36
***NarI*FT DFPHOH6HI**	21	$C_{125}H_{152}F_2N_{35}O_{74}P_{11}$	3705.63	$[M-4H]^{4-}$ = 925.61	3706.44
***NarI*FT DMePhOH6HI**	51	$C_{127}H_{158}N_{35}O_{74}P_{11}$	3697.68	$[M-4H]^{4-}$ = 923.58	3698.32
***NarI*FT 6OHNap6HI**	60	$C_{129}H_{156}N_{35}O_{74}P_{11}$	3719.66	$[M-4H]^{4-}$ = 929.11	3720.44
***NarI*FC PhOH6HI**	45	$C_{123}H_{152}N_{37}O_{72}P_{11}$	3639.35	$[M-4H]^{4-}$ = 908.97	3639.88
***NarI*FG PhOH6HI**	41	$C_{125}H_{152}N_{41}O_{72}P_{11}$	3719.66	$[M-4H]^{4-}$ = 928.63	3718.51
****NarI*FA PhOH6HI**	48	$C_{125}H_{152}N_{41}O_{70}P_{11}$	3688.67		3687.784

*Mass acquired using MALDI-TOF.

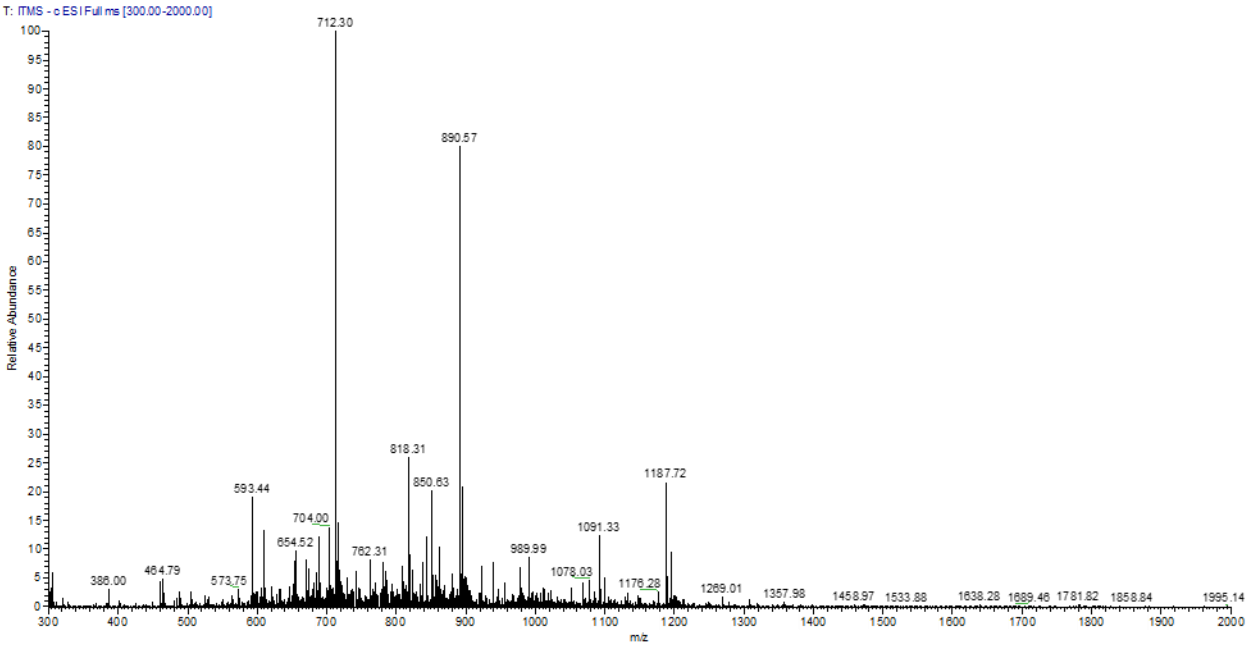

Figure S10. ESI^- MS spectrum for Nar1FT 6HI.

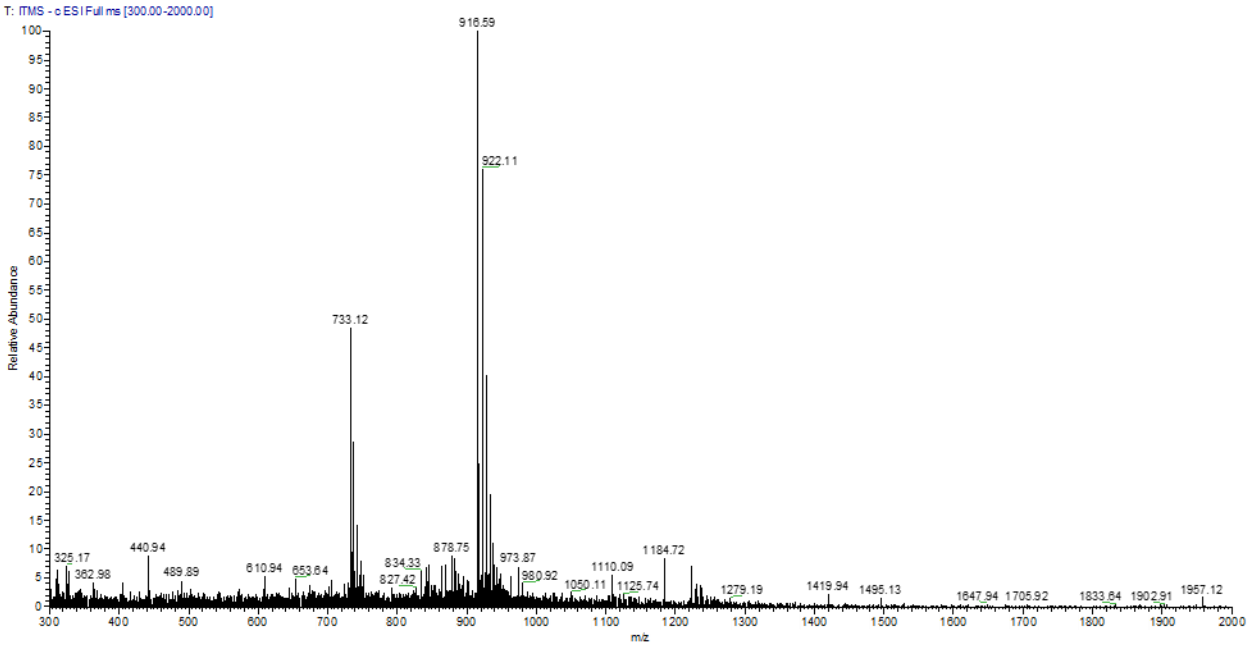

Figure S11. ESI$^-$ MS spectrum for Nar1FT PhOH6HI.

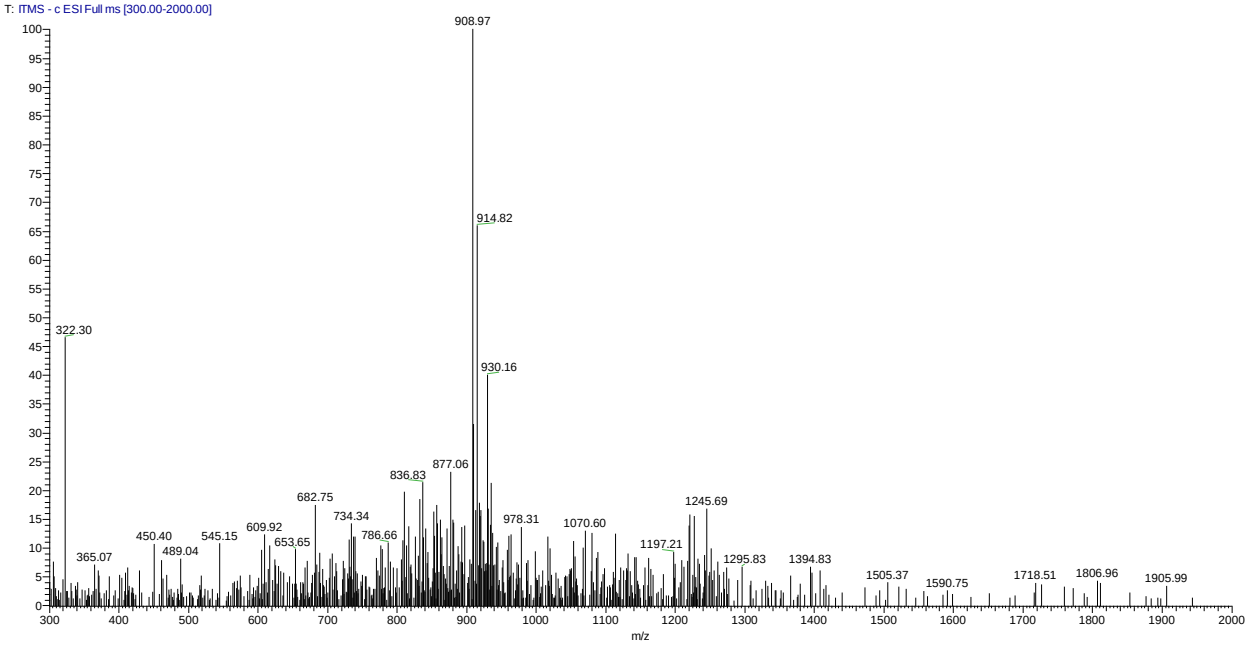

Figure S12. ESI$^-$ MS spectrum for Nar1FC PhOH6HI.

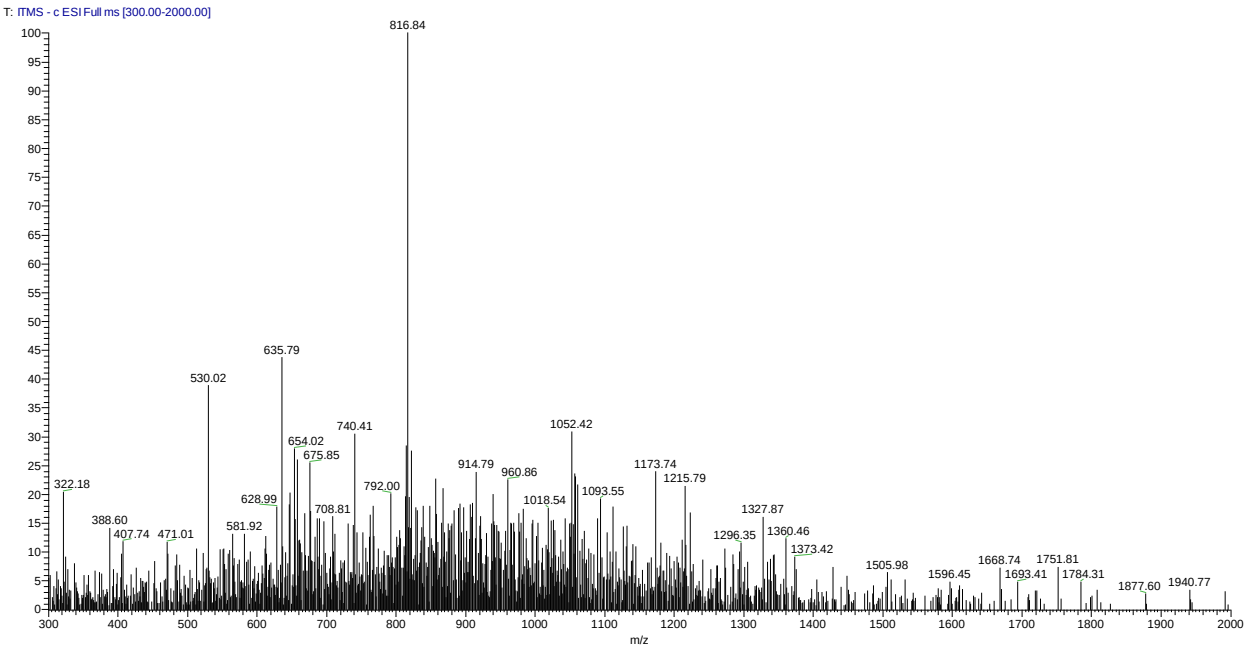

Figure S13. ESI$^-$ MS spectrum for Nar1FG PhOH6HI.

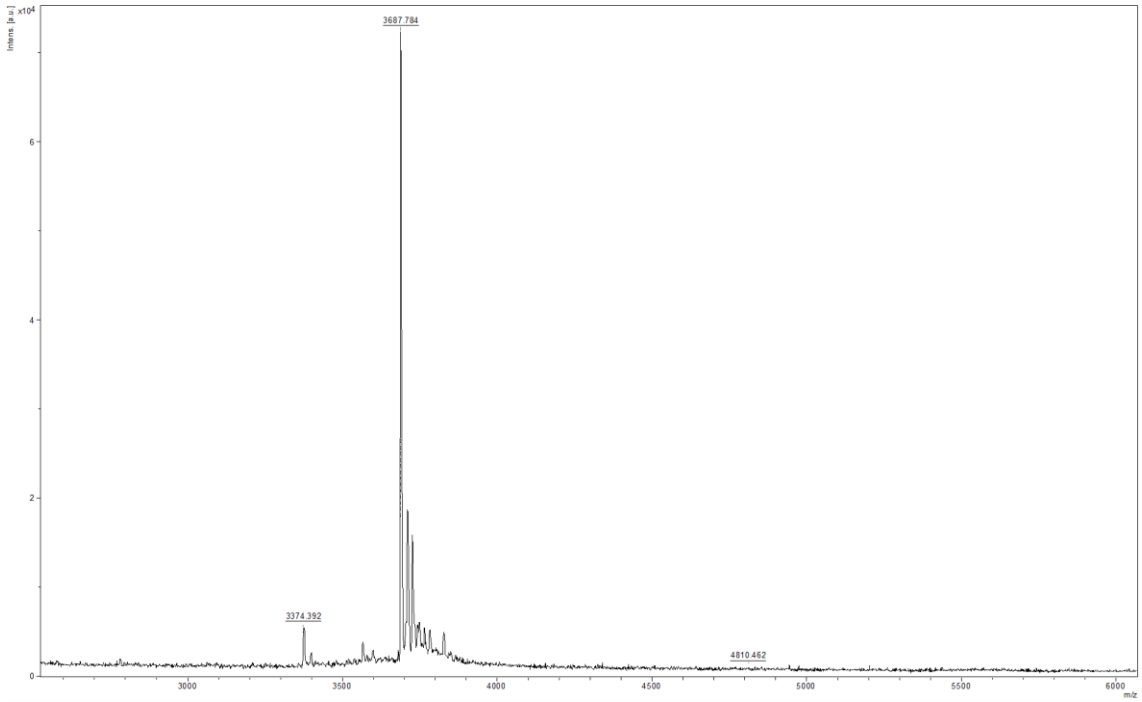

Figure S14. MALDI-TOF MS spectrum for Nar1FA PhOH

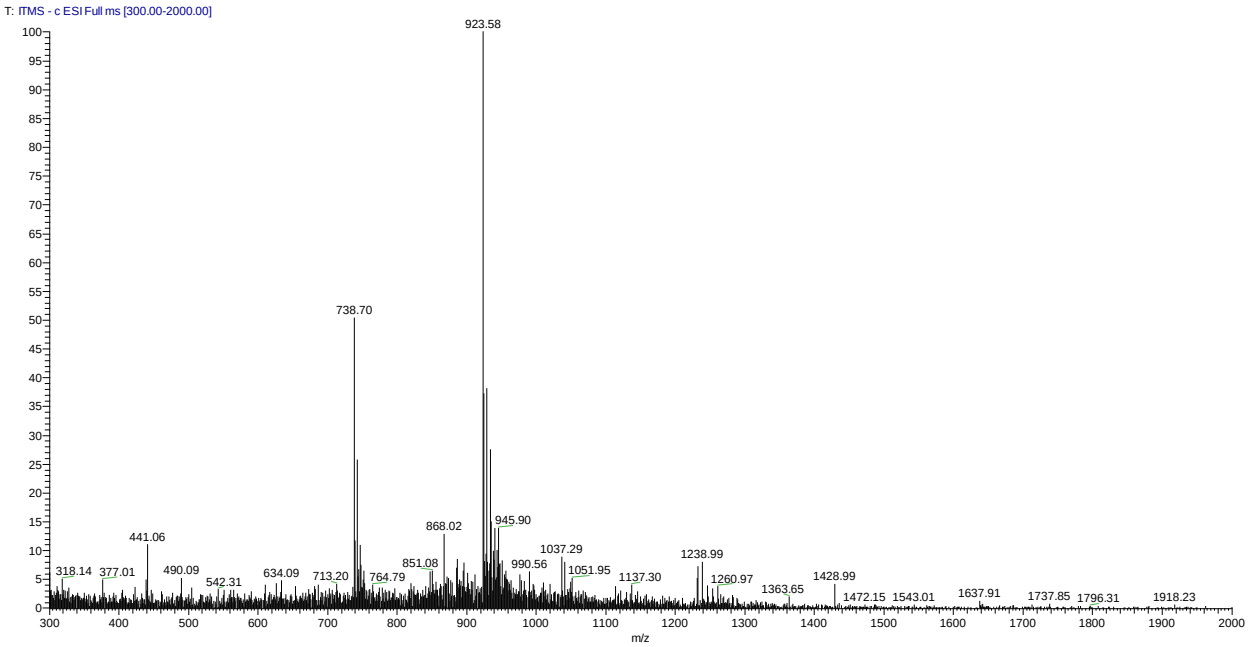

Figure S15. ESI$^-$ MS spectrum for Nar1FT DMePhOH6HI.

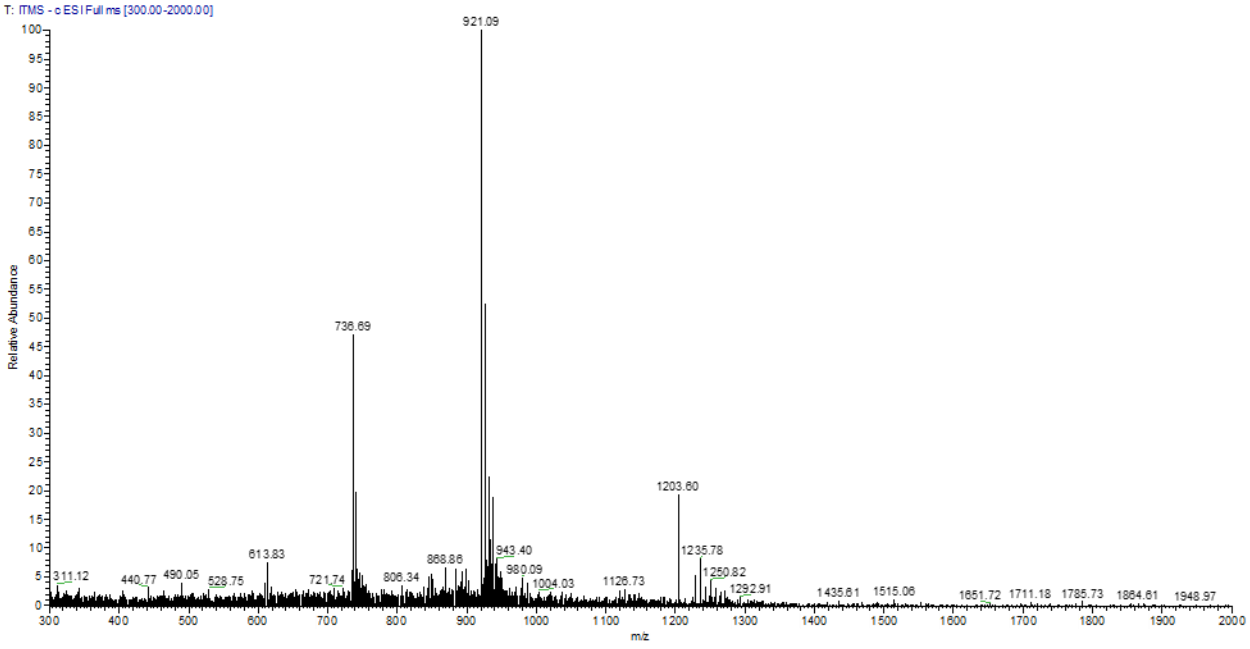

Figure S16. ESI$^-$ MS spectrum for Nar1FT FPhOH6HI.

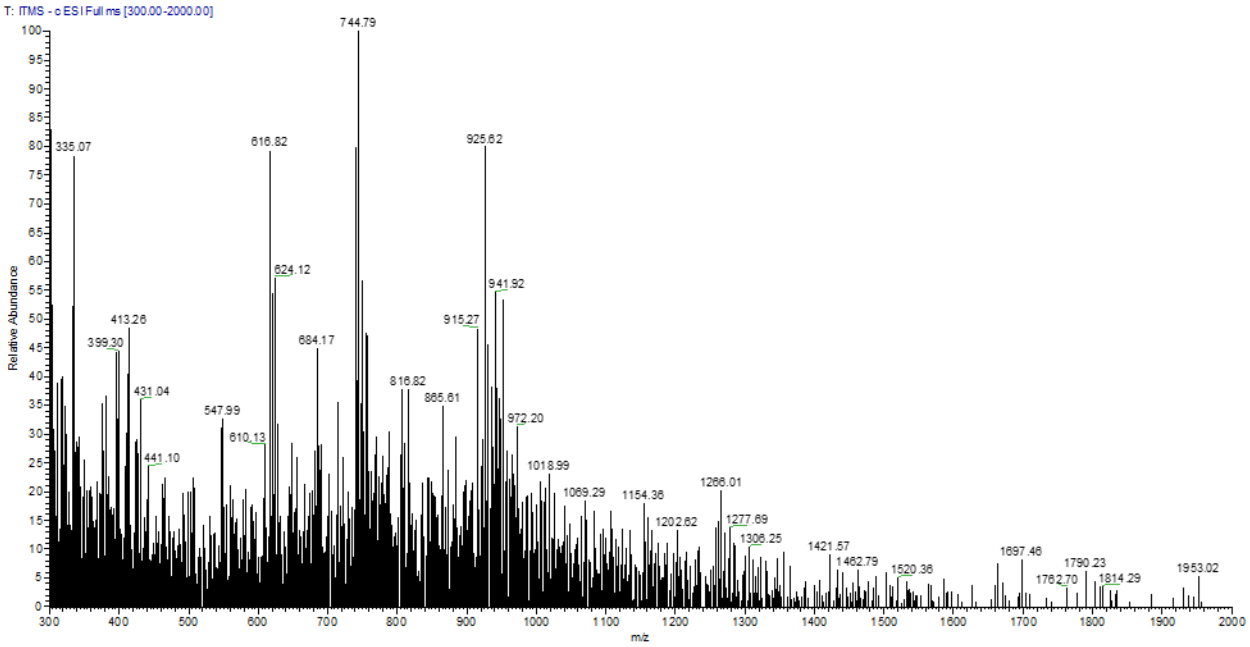

Figure S17. ESI$^-$ MS spectrum for Nar1FT DFPhOH6HI.

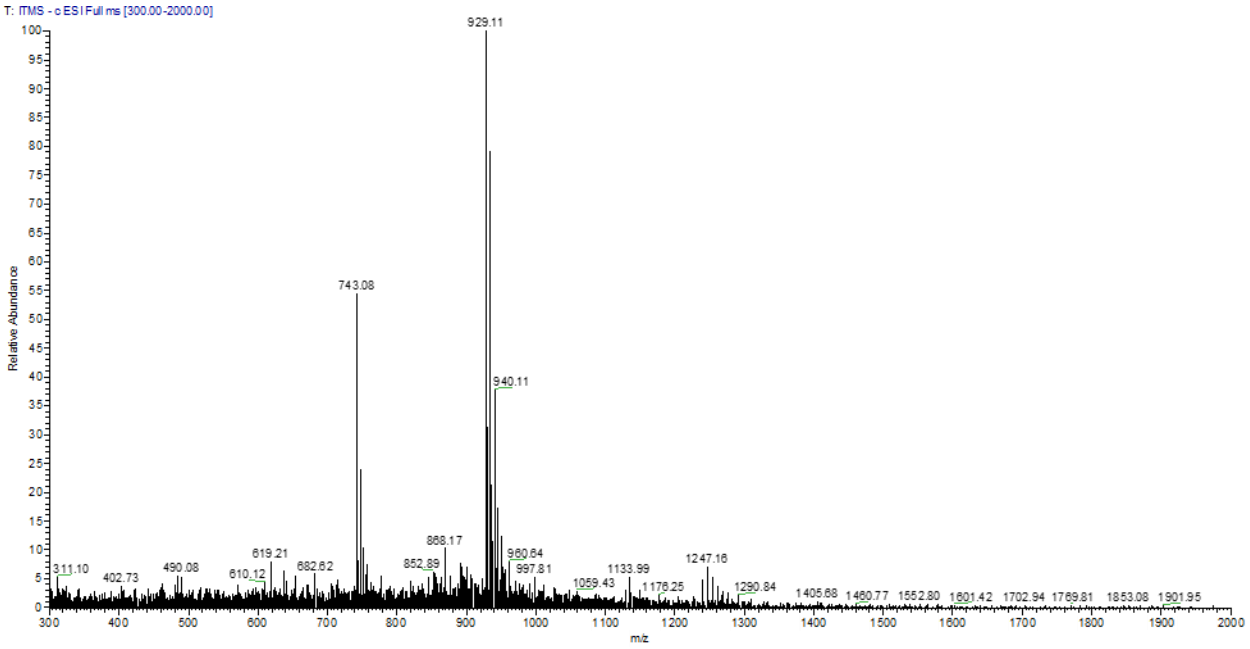

Figure S18. ESI$^-$ MS spectrum for Nar1FT 6OHNap6HI

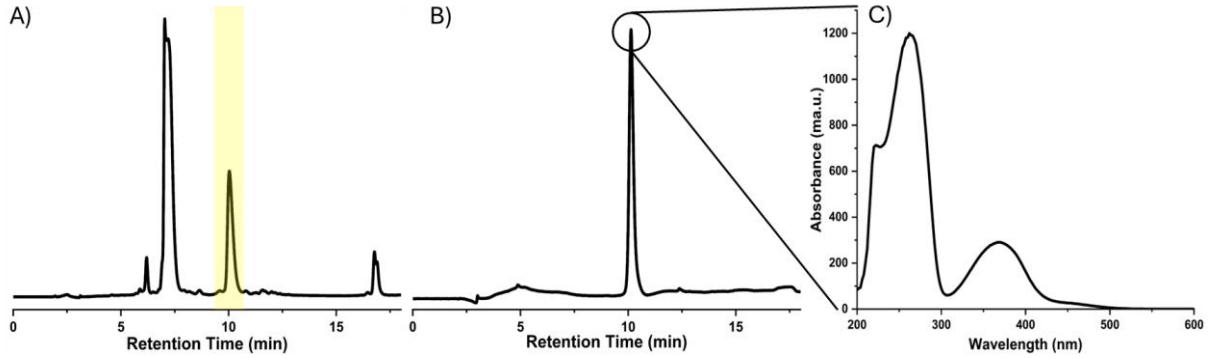

Figure S19. Nar1FT PhOH A) Crude HPLC trace, post on strand synthesis and ethanol precipitation. Collected fraction is highlighted in yellow. B) HPLC trace of collected, purified product. C) Corresponding UV-Vis Spectra of collected trace.

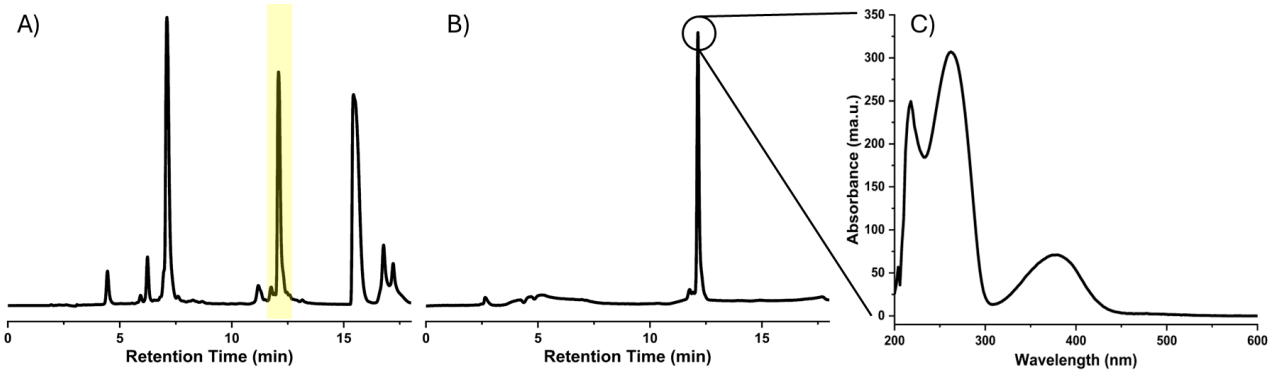

Figure S20. Nar1FT DMePhOH A) Crude HPLC trace, post on strand synthesis and ethanol precipitation. Collected fraction is highlighted in yellow. B) HPLC trace of collected, purified product. C) Corresponding UV-Vis Spectra of collected trace.

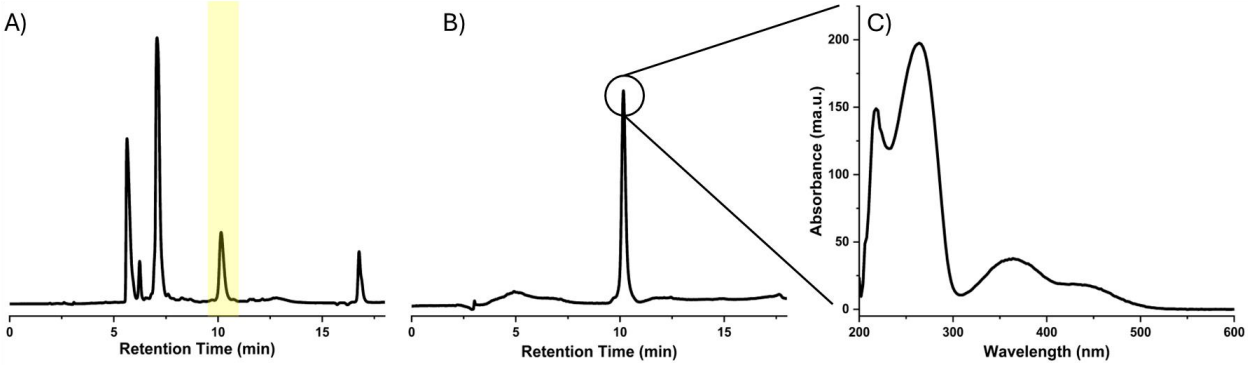

Figure S21. Nar1FT FPOH A) Crude HPLC trace, post on strand synthesis and ethanol precipitation. Collected fraction is highlighted in yellow. B) HPLC trace of collected, purified product. C) Corresponding UV-Vis Spectra of collected trace.

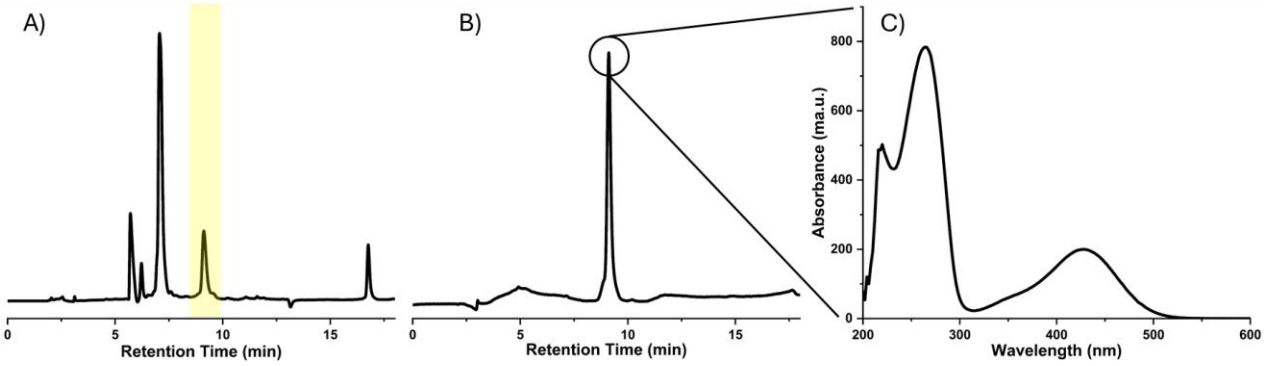

Figure S22. Nar1FT DFPhOH A) Crude HPLC trace, post on strand synthesis and ethanol precipitation. Collected fraction is highlighted in yellow. B) HPLC trace of collected, purified product. C) Corresponding UV-Vis Spectra of collected trace.

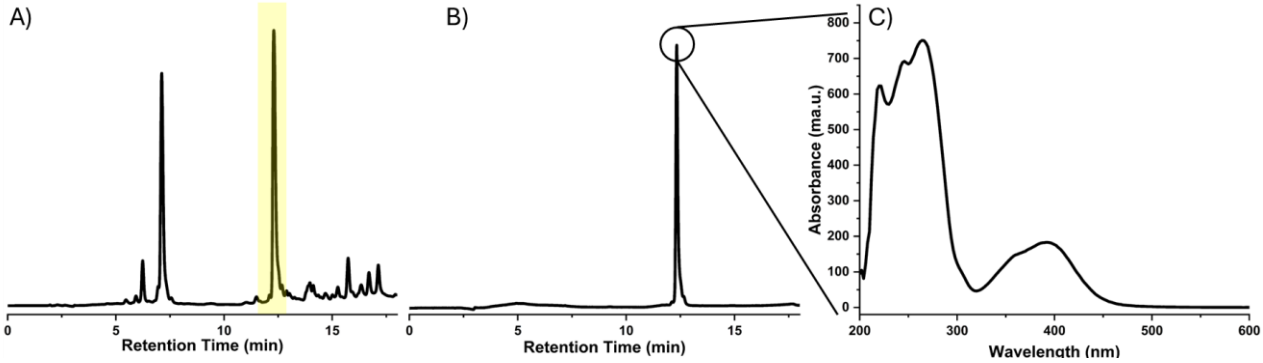

Figure S23. Nar1FT 6OHNap A) Crude HPLC trace, post on strand synthesis and ethanol precipitation. Collected fraction is highlighted in yellow. B) HPLC trace of collected, purified product. C) Corresponding UV-Vis Spectra of collected trace.

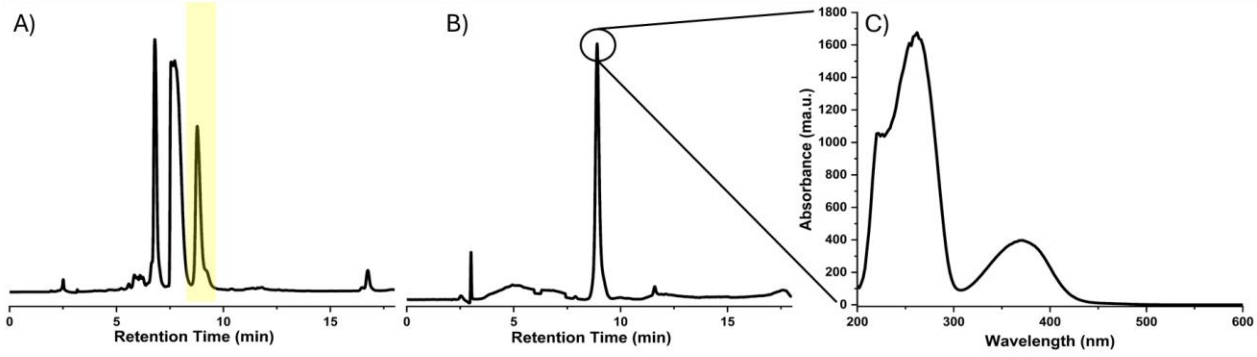

Figure S24. Nar1FA PhOH A) Crude HPLC trace, post on strand synthesis and ethanol precipitation. Collected fraction is highlighted in yellow. B) HPLC trace of collected, purified product. C) Corresponding UV-Vis Spectra of collected trace.

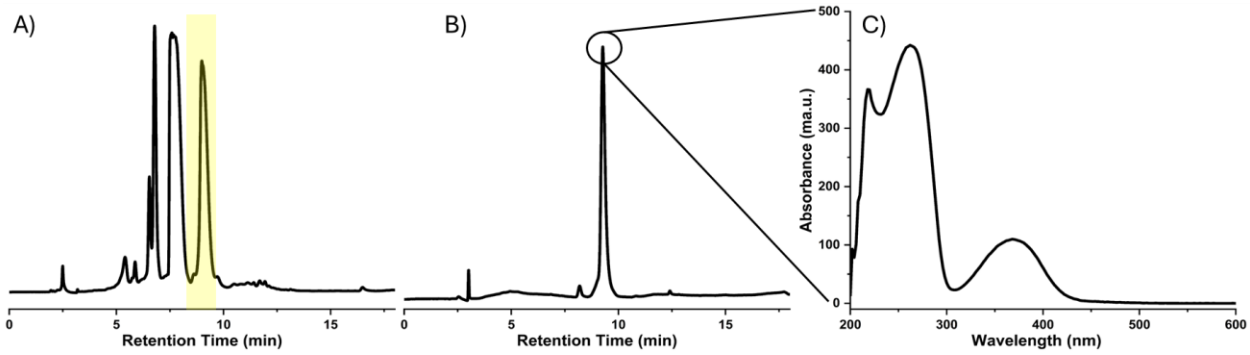

Figure S25. Nar1FC PhOH A) Crude HPLC trace, post on strand synthesis and ethanol precipitation. Collected fraction is highlighted in yellow. B) HPLC trace of collected, purified product. C) Corresponding UV-Vis Spectra of collected trace.

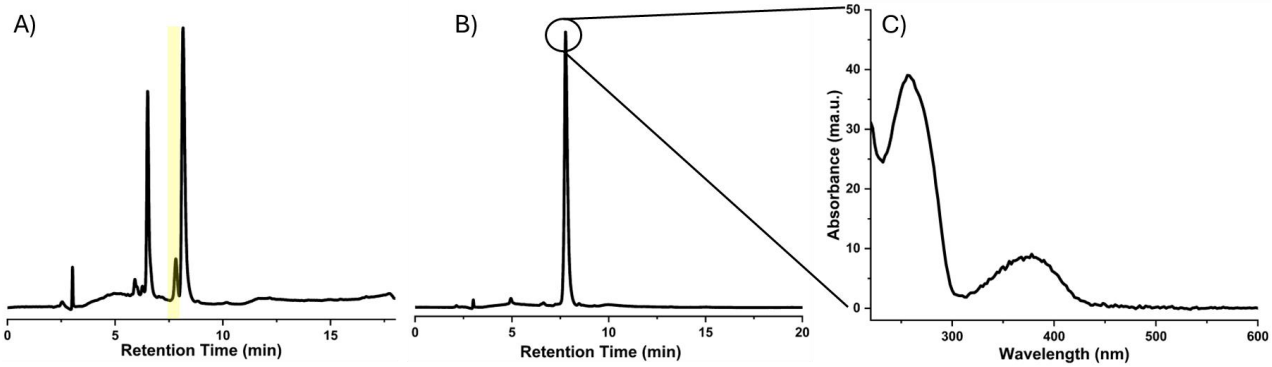

Figure S26. Nar1FG PhOH A) Crude HPLC trace, post on strand synthesis and ethanol precipitation. Collected fraction is highlighted in yellow. B) HPLC trace of collected, purified product. C) Corresponding UV-Vis Spectra of collected trace.

Table S3. Melting temperatures and photophysical properties of TXT *Narl*12 DNA and DNA:RNA hybrid duplexes.

5'-CTC-GGT-X-TCA-TC-3' 3'-GAG-CCA-C-AGT-AG-5'	5'-CTC-GGT-X-TCA-TC-3' 3'-GAG-CCA---AGT-AG-5'	5'-CTC-GGT-X-TCA-TC-3' 3'-GAG-CCA-C-AGU-AG-5'
(FL)	(N-1)	(RNA)

X[a]	DS[b]	T_m (ΔT_m)[c]	λ_{ex} ROH/RO$^-$[d]	λ_{em} ROH*/RO^{-*}[e]	$\Delta\nu$[f]	I_{rel}[g]	Φ_{fl}[h]	ε_{max}[i]	B[j]
PhOH	FL	58.3 (1.3)	390/–	493/562$^{2.0}$	103/172	5	0.21	10.5	2210
PhOH	N-1	58.1 (1.1)	390/–	493/570$^{0.8}$	103/180	6	0.22	24.9	5480
PhOH	RNA	46.9 (–4.1)	390/–	495/–	105	20	0.27	26.4	7130
DMePhOH	FL	53.0 (–4.0)	397/–	505/584$^{2.3}$	108/187	6	0.12	23.0	2760
DMePhOH	N-1	52.9 (–4.1)	400/–	505/595$^{1.4}$	105/195	6	0.18	18.8	3390
DMePhOH	RNA	46.6 (–4.4)	397/–	505/592$^{3.2}$	108/195	17	0.34	26.6	9040
NapOH	FL	53.7 (–3.3)	405/–	565/–	160	4	0.06	29.0	1740
NapOH	N-1	52.6 (–4.4)	407/–	552/–	145	7	0.13	14.0	1820
NapOH	RNA	46.4 (–4.6)	406/–	564/–	158	7	0.12	21.0	2520
FPhOH	FL	49.6 (–7.4)	378/462$^{5.3}$	–/575	197/113	6	0.30	13.0	3900
FPhOH	N-1	50.3 (–6.7)	380/464$^{3.3}$	–/570	190/106	10	0.31	20.0	6200
FPhOH	RNA	45.1 (–5.9)	381/465$^{7.8}$	–/588	207/123	6	0.10	34.0	3400
DFPhOH	FL	48.8 (–8.2)	371/451$^{0.38}$	–/572	201/121	3	0.15	17.0	2550
DFPhOH	N-1	48.9 (–8.1)	362/448$^{0.24}$	–/569	207/121	5	0.12	25.3	3040
DFPhOH	RNA	39.5 (–11.5)	374/452$^{1.5}$	–/578	204/126	8	0.26	20.0	5200

[a] See Figure 2 for surrogate abbreviations. [b] Double strand, RNA complement contains 2'-OMe groups. [c] T_m values in °C of *Narl*12 DS (2 mM) measured at 260 nm in 1X PBS buffer, pH 7.4, heating rate of 0.5 °C/min, errors are ±1 °C; ΔT_m = T_m (modified DS with probe (X) opposite N = C (FL) or paired with N-1 complement) – 57 °C (T_m of native *Narl*12 DS containing X = G paired with N = C) or – 51 °C (T_m of native DNA:RNA hybrid DS). [d] Excitation maximum in nm for ROH or RO$^-$, for FPhOH and DFPhOH I_{ROH}/I_{RO-} values are given as superscripts. [e] Emission maximum in nm for ROH* or RO^{*-}, for PhOH and DMePhOH I_{ROH^*}/I_{RO-^*} values are given as superscripts. [f] Stokes' shift in nm. [g] Relative emission intensity in the DS versus SS. [h] Fluorescence quantum yield of chalcone probes in the DS measured by the comparative method using quinine sulfate (Φ_{fl} = 0.56) in 0.1 M H_2SO_4 for PhOH, DMePhOH, perylene (Φ_{fl} = 0.94) in cyclohexane for NapOH, and coumarin 6 (Φ_{fl} = 0.78) in ethanol for FPhOH and DFPhOH, errors are ± 5% obtained from three measurements via titration of labeled *Narl*12 into excess complementary oligo. [i] Probe absorption coefficients in DS (10^{-3} cm^{-1}M^{-1}). [j] Probe brightness (Φ_{fl}• ε_{max}) in cm^{-1}M^{-1}. All spectra were acquired in 1X PBS buffer, pH 7.4 at room temperature with 2 μM modified *Narl*12 in the presence of 2 equiv. complementary strand.

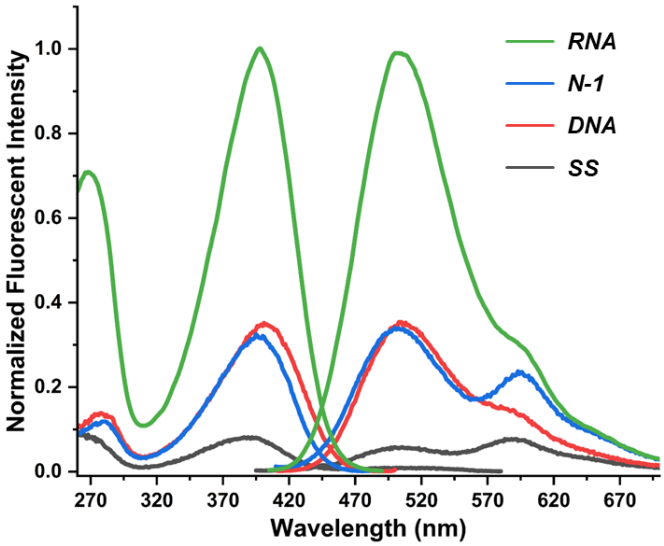

Figure S27. Normalized Fluorescence intensity for *Narl*12 DMePhOH6HI bound to FL DNA (red), N-1 DNA (blue) and RNA (green) complementary strands. Spectra were acquired in 1X PBS buffer, pH 7.4 at room temperature with 2 μM modified *Narl*12 (black trace is SS) in the presence of 2 equiv. complementary strand.

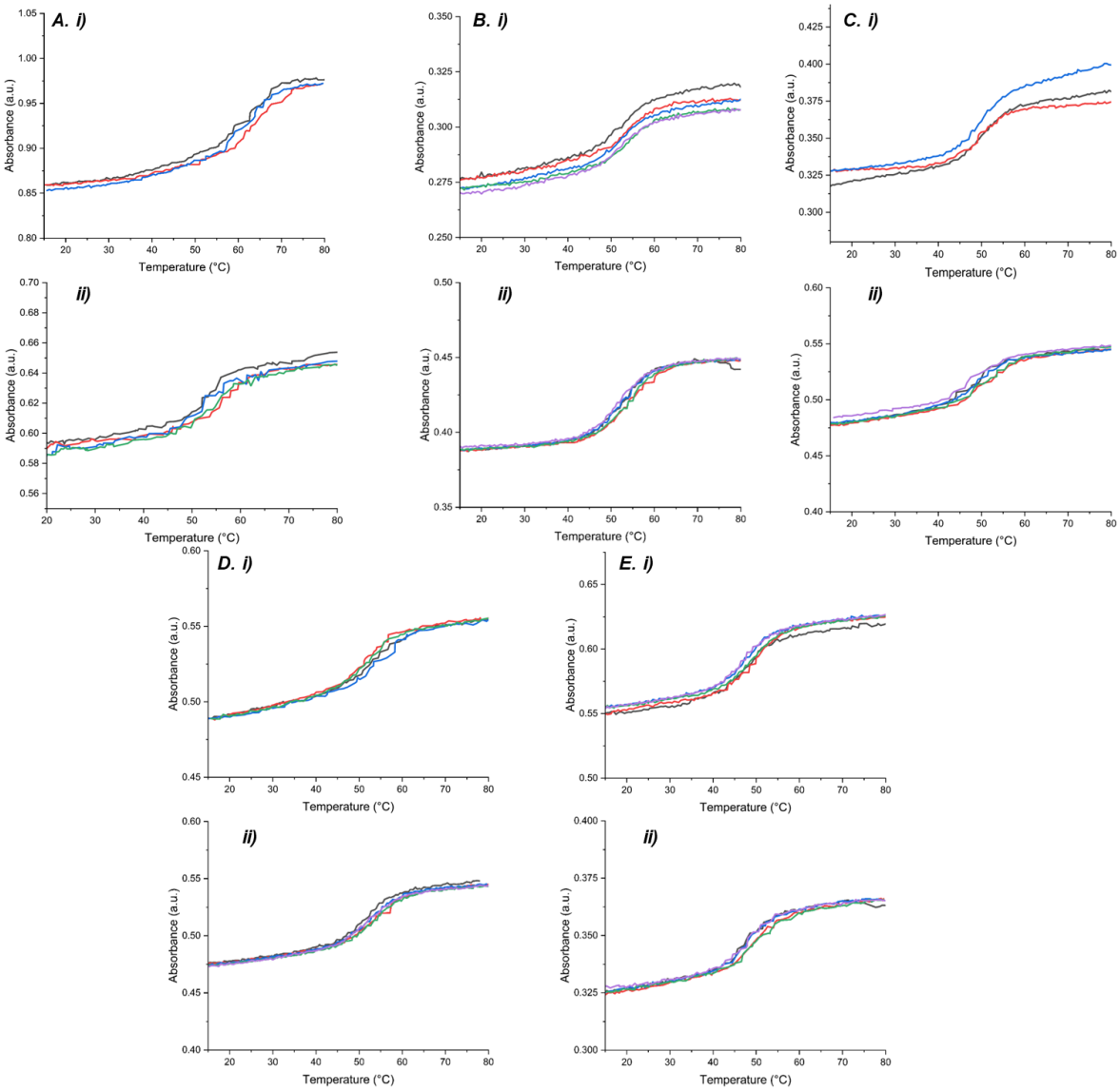

Figure S28. Thermal melting curves for A) Nar1FT PhOH B) Nar1FT FPhOH C) Nar1FT DFPhOH D) Nar1FT DMePhOH and E) Nar1FT 6OHNap, with i) full DNA complement and ii) N-1 complement.

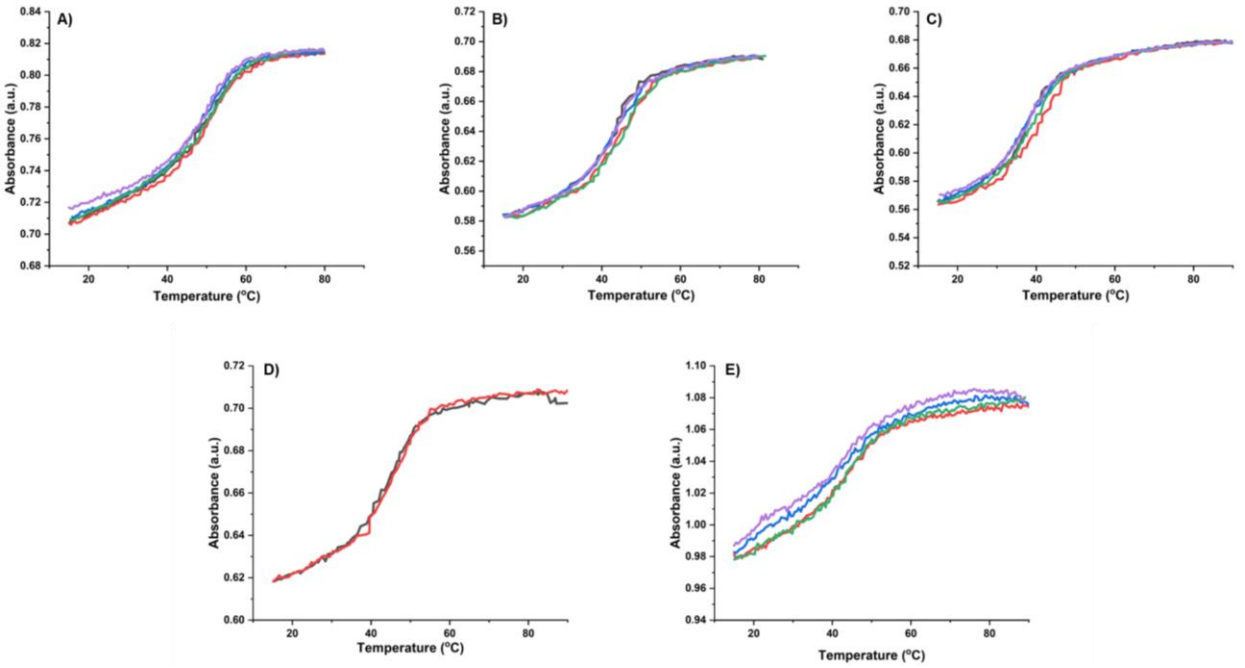

Figure S29. Thermal melting curves for A) Nar1FT PhOH B) Nar1FT FPhOH C) Nar1FT DFPhOH D) Nar1FT DMePhOH and E) Nar1FT 6OHNap with RNA complement

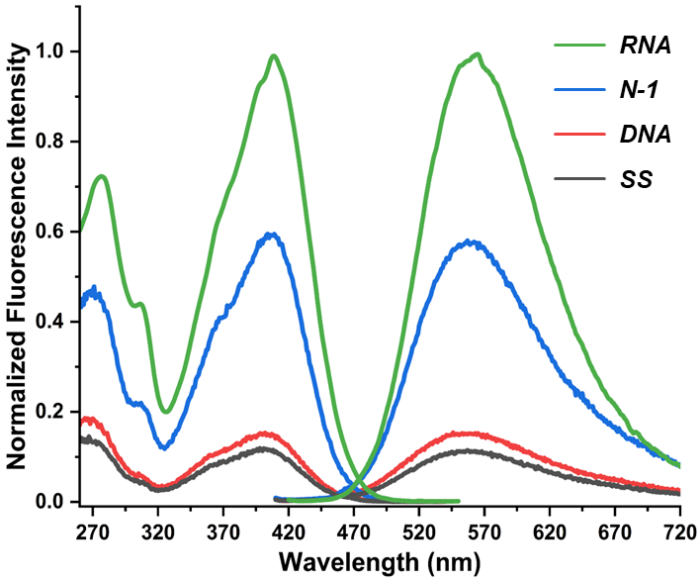

Figure S30. Normalized Fluorescence intensity for *Narl*12 NapOH6HI bound to FL DNA (red), N-1 DNA (blue) and RNA (green) complementary strands. Spectra were acquired in 1X PBS buffer, pH 7.4 at room temperature with 2 μM modified *Narl*12 (black trace is SS) in the presence of 2 equiv. complementary strand.

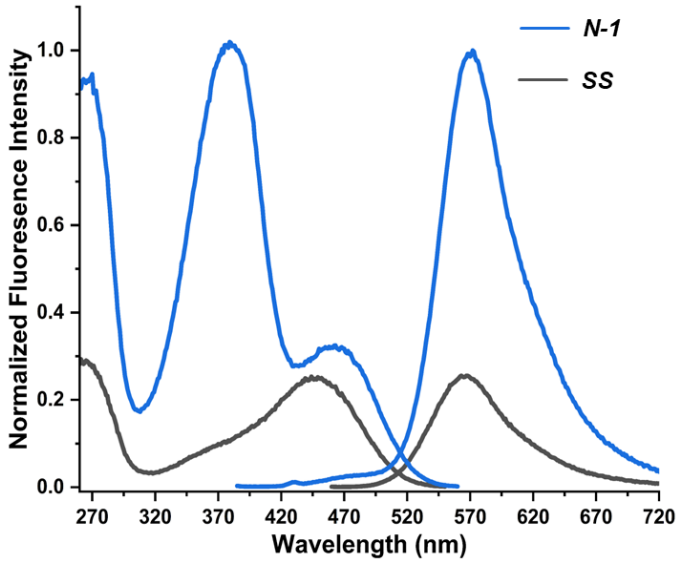

Figure S31. Normalized Fluorescence intensity for *Narl*12 FPhOH bound to N-1 DNA (blue) complementary strand. Spectra were acquired in 1X PBS buffer, pH 7.4 at room temperature with 2 μM modified *Narl*12 (black trace is SS) in the presence of 2 equiv. complementary strand.

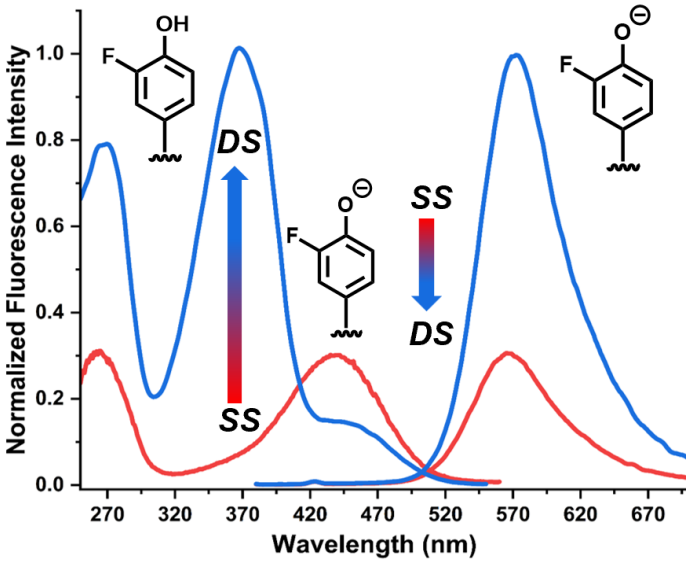

Figure S32. Normalized excitation/emission spectra for *Narl*12 FPhOH6HI bound to FL DNA (blue) complementary strand. Spectra were acquired in 1X PBS buffer, pH 7.4 at room temperature with 2 μM modified *Narl*12 (red trace is SS) in the presence of 2 equiv. complementary strand. Spectra highlight ratiometric excitation response to hybridization by FPhOH6HI.

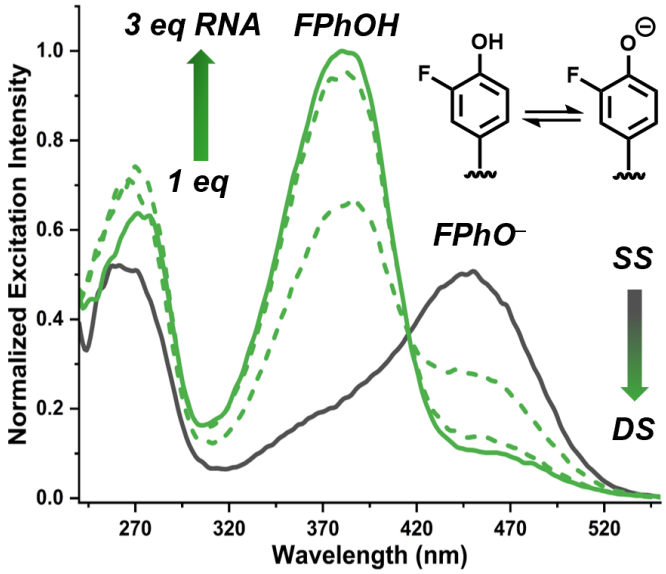

Figure S33. Excitation spectra for FPhOH6HI displaying phenolate ($FPhO^-$) excitation in the SS (black trace) to predominately phenol (FPhOH) excitation in the DNA:RNA hybrid duplex (green traces) at pH 7.4. Spectra were acquired in 1X PBS buffer, pH 7.4 at room temperature with 2 μM modified *Narl*12 (black trace is SS) in the presence of 3 equiv. RNA complementary strand.

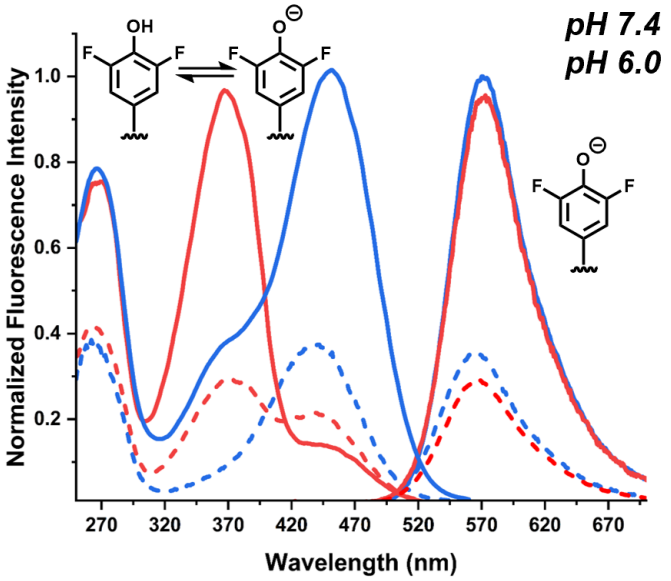

Figure S34. Excitation/emission spectra for DFPhOH6HI in the *Narl*12 SS at pH 7.4 (dashed blue traces) and pH 6.0 (dashed red traces) vs. the FL DNA duplex at pH 7.4 (solid blue traces) and pH 6.0 (solid red traces).

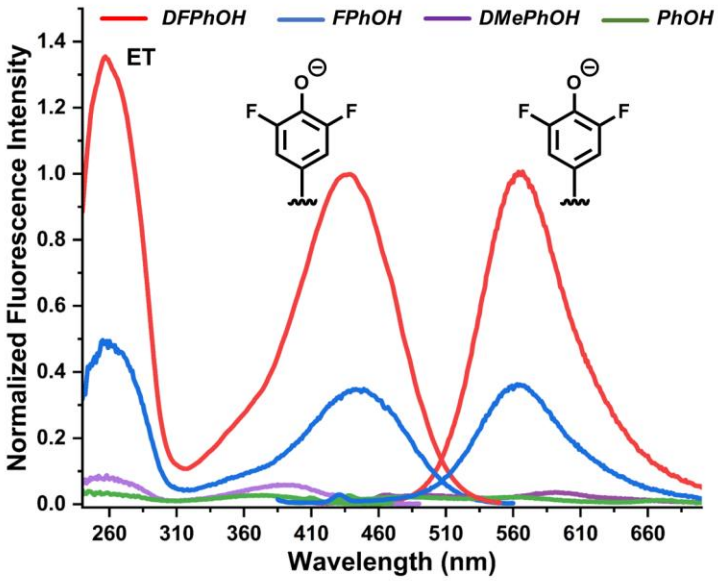

Figure S35. Excitation/emission spectra for DFPhOH6I, FPhOH6HI, DMePhOH6HI, and PhOH6HI at G8 of TBA15 recorded in Tris.HCl pH 8.0, 50 mM KCl, 50 mM MgCl2.

Table S4. Yields and MS Analysis of Modified TBA15 Oligonucleotides.

***TBA*15**	**On-Strand Yield (%)**	**Formula**	**Calc. Mass**	**Exptl (m/z) (ESI^-)**	**Exptl Mass**
6HI	-	$C_{152}H_{188}N_{52}O_{94}P_{14}$	4675.81	$[M-6H+Na^+]^{5-}$ = 783.23	4682.4
PhOH6HI	62	$C_{161}H_{195}N_{51}O_{94}P_{14}$	4781.82	$[M-4H]^{4-}$ = 1194.7	4782.8
FPhOH6HI	34	$C_{161}H_{194}FN_{51}O_{94}P_{14}$	4799.83	$[M-5H]^{5-}$ = 959.3	4801.5
DFPHOH6HI	36	$C_{161}H_{193}F_2N_{51}O_{94}P_{14}$	4816.82	$[M-5H]^{5-}$ = 963.0	4820.0
DMePhOH6HI	64	$C_{161}H_{196}N_{52}O_{95}P_{14}$	4811.85	$[M-6H+Na^+]^{5-}$ = 804.7	4811.4
T_L 6HI	-	$C_{153}H_{188}N_{52}O_{95}P_{14}$	4707.78	$[M-6H+K^+]^{5-}$ = 790.04	4707.2
T_L PhOH6HI	50	$C_{160}H_{192}N_{52}O_{96}P_{14}$	4812.81		4810.460
T_L DMePhOH	53	$C_{162}H_{196}N_{52}O_{96}P_{14}$	4840.84	$[M-6H]^{6-}$ = 805.7	4840.1

*Mass acquired using MALDI-TOF

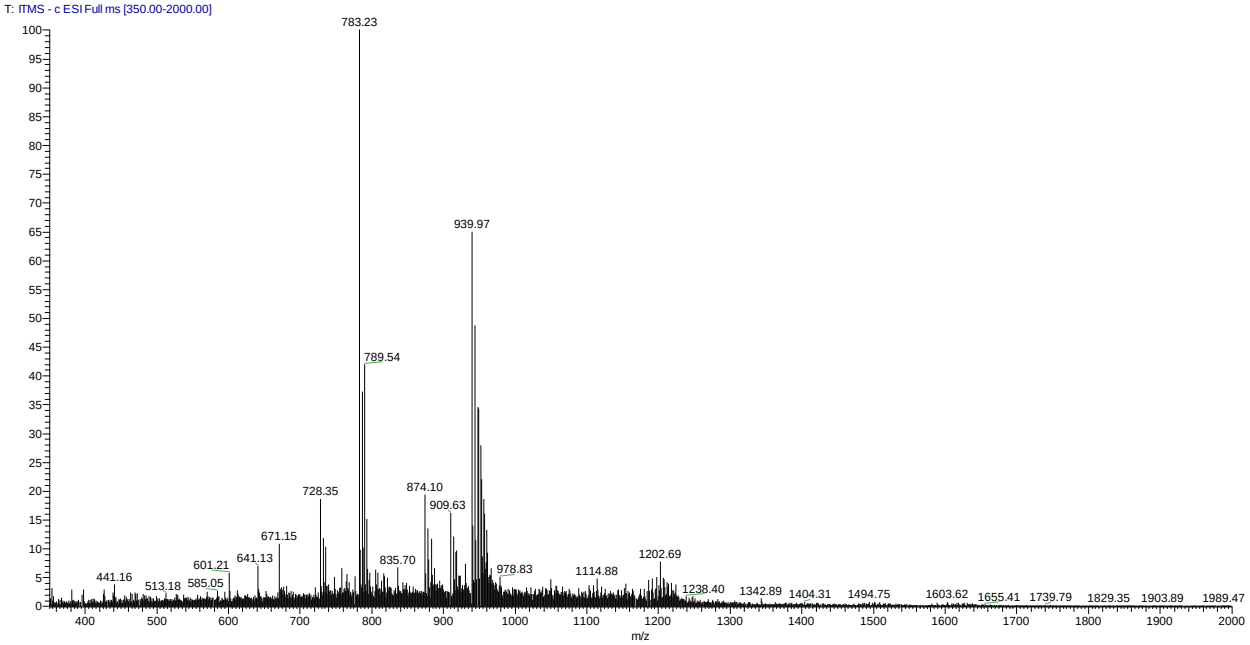

Figure S36. ESI^- MS spectrum for TBA15 6HI.

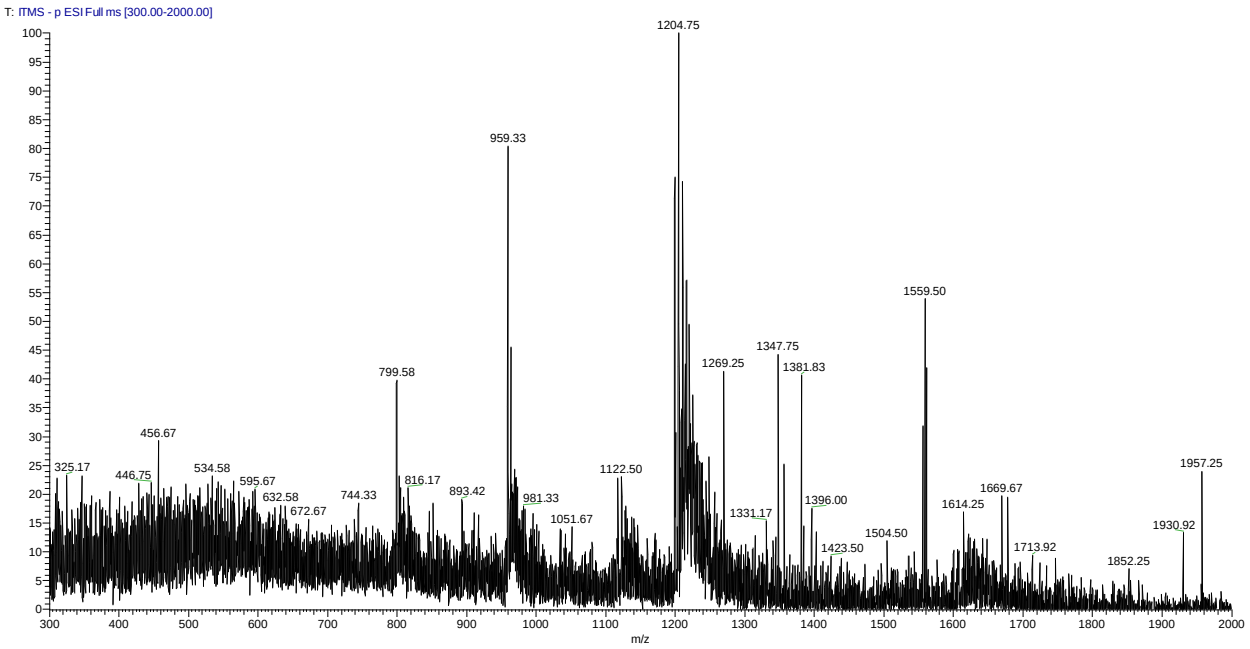

Figure S37. ESI$^-$ MS spectrum for TBA15 PhOH6HI.

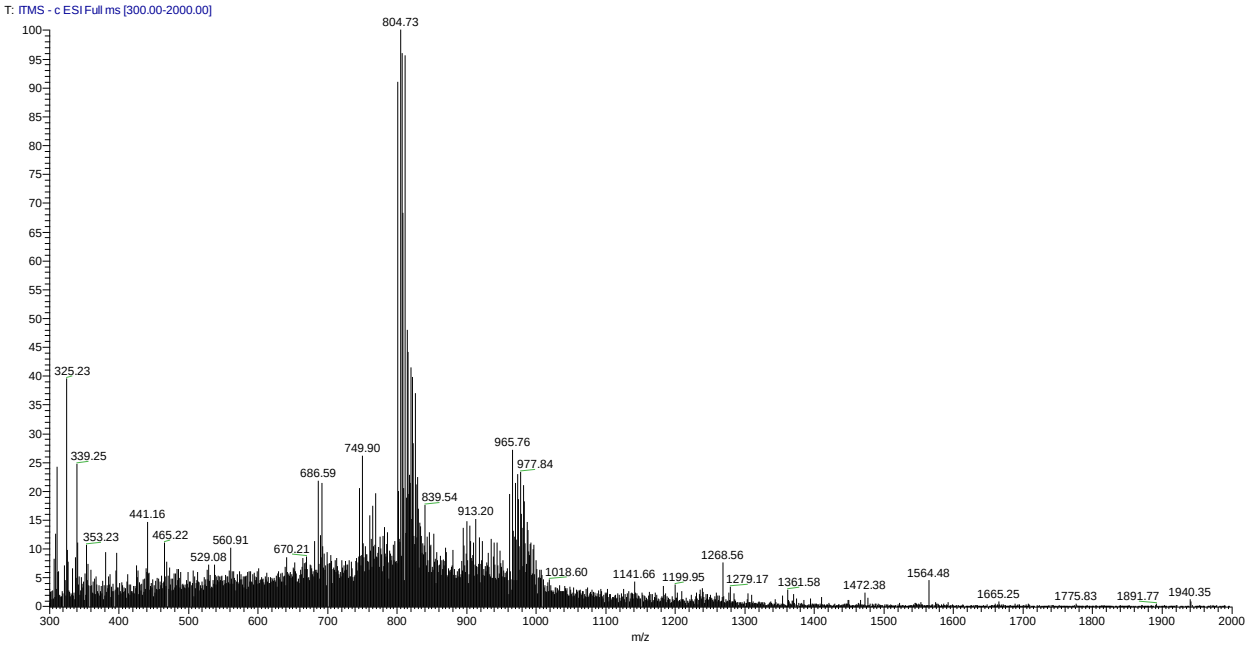

Figure S38. ESI$^-$ MS spectrum for TBA15 DMePhOH6HI.

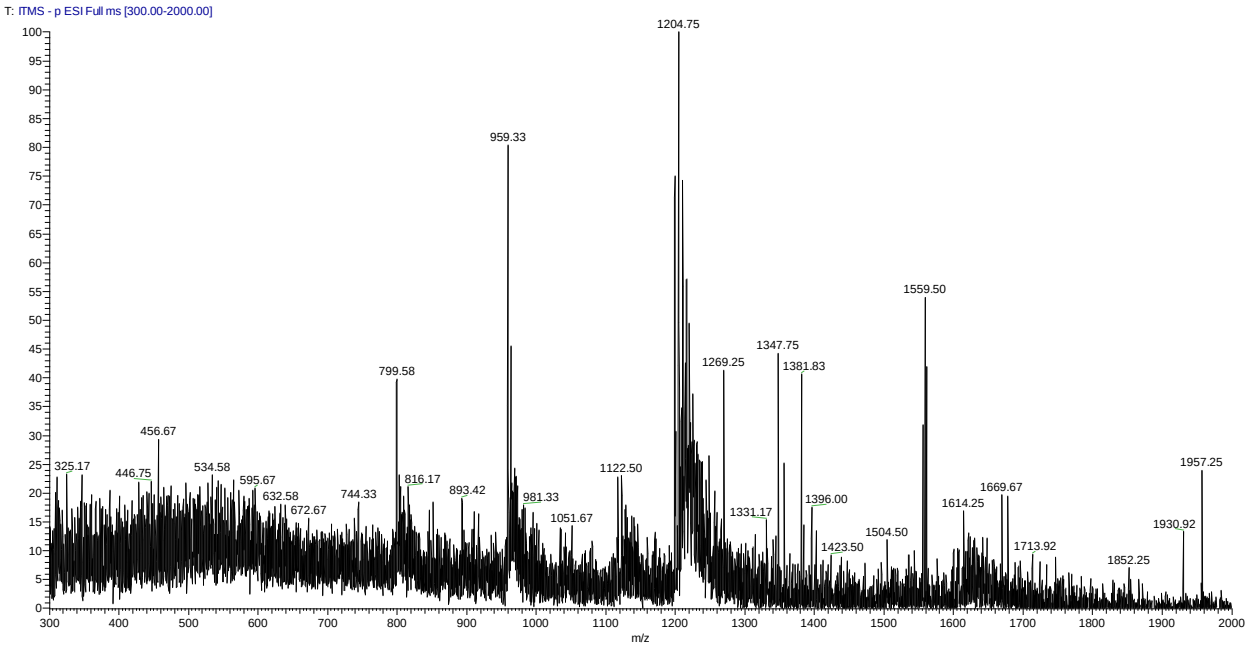

Figure S39. ESI$^-$ MS spectrum for TBA15 FPhOH6HI.

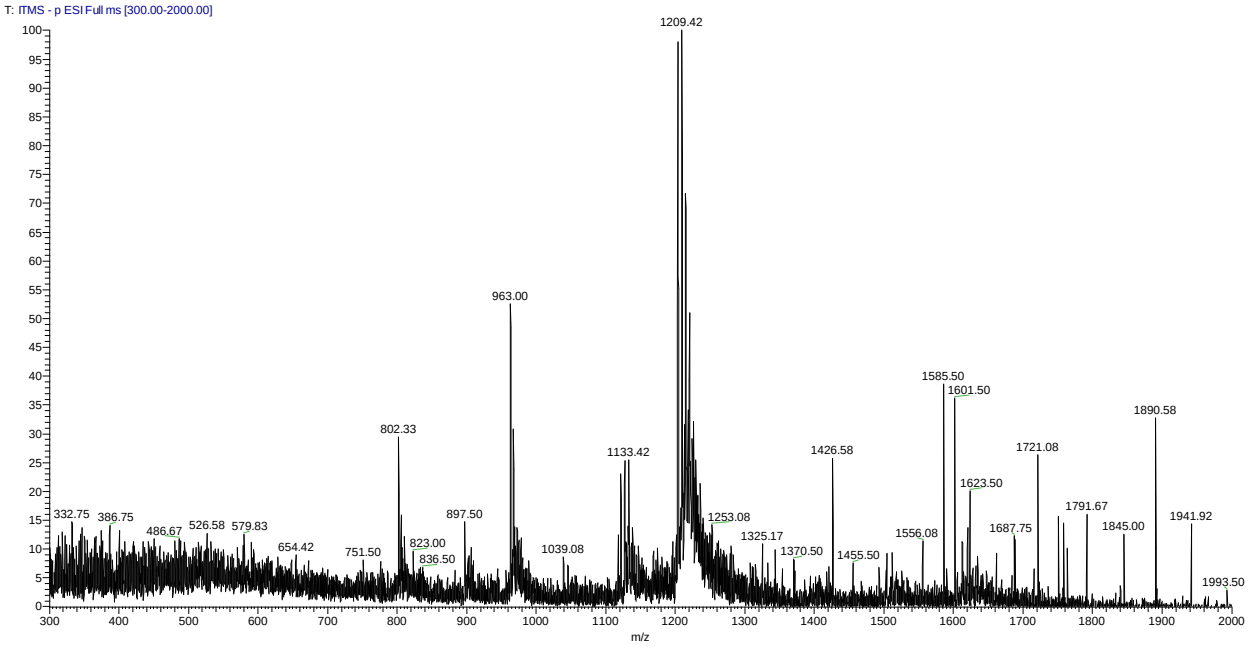

Figure S40. ESI$^-$ MS spectrum for TBA15 DFPhOH6HI.

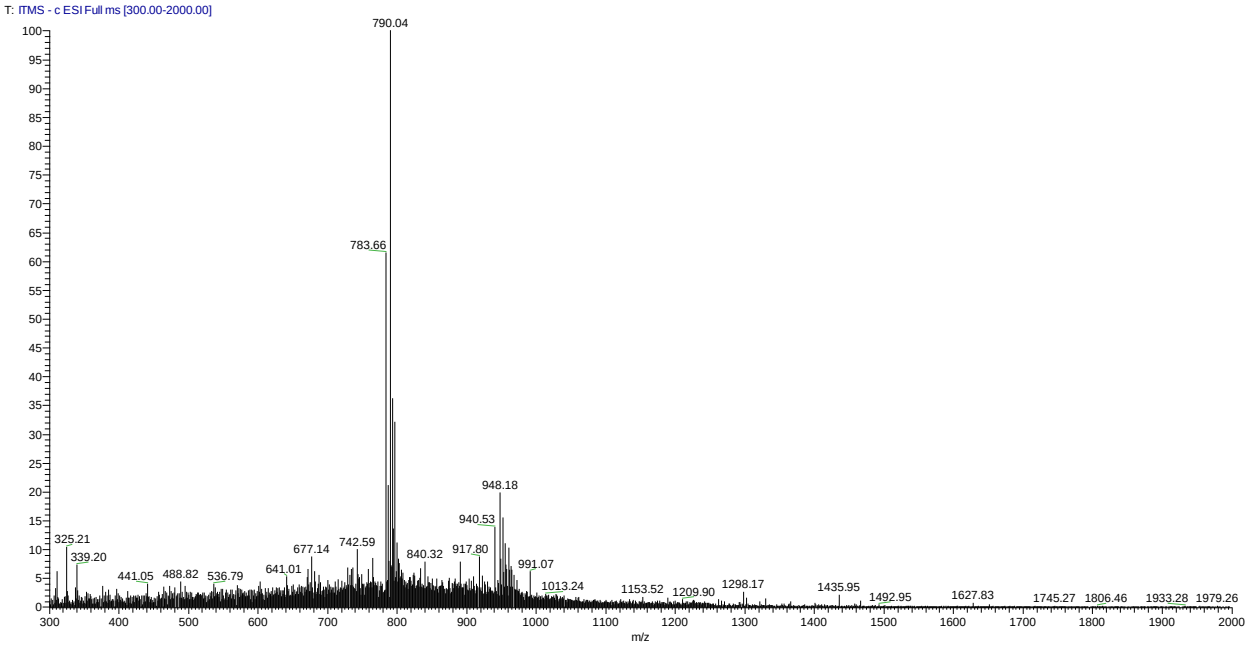

Figure S41. ESI$^-$ MS spectrum for TBA15 T_L 6HI.

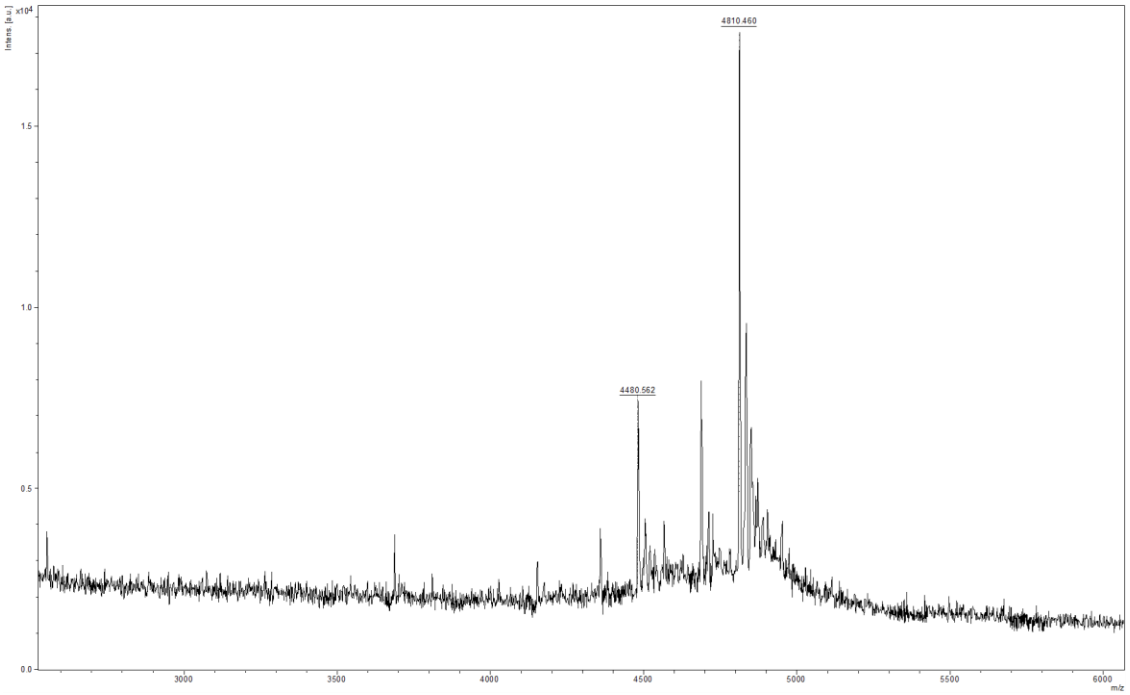

Figure S42. MALDI-TOF MS spectrum for TBA T_L PhOH

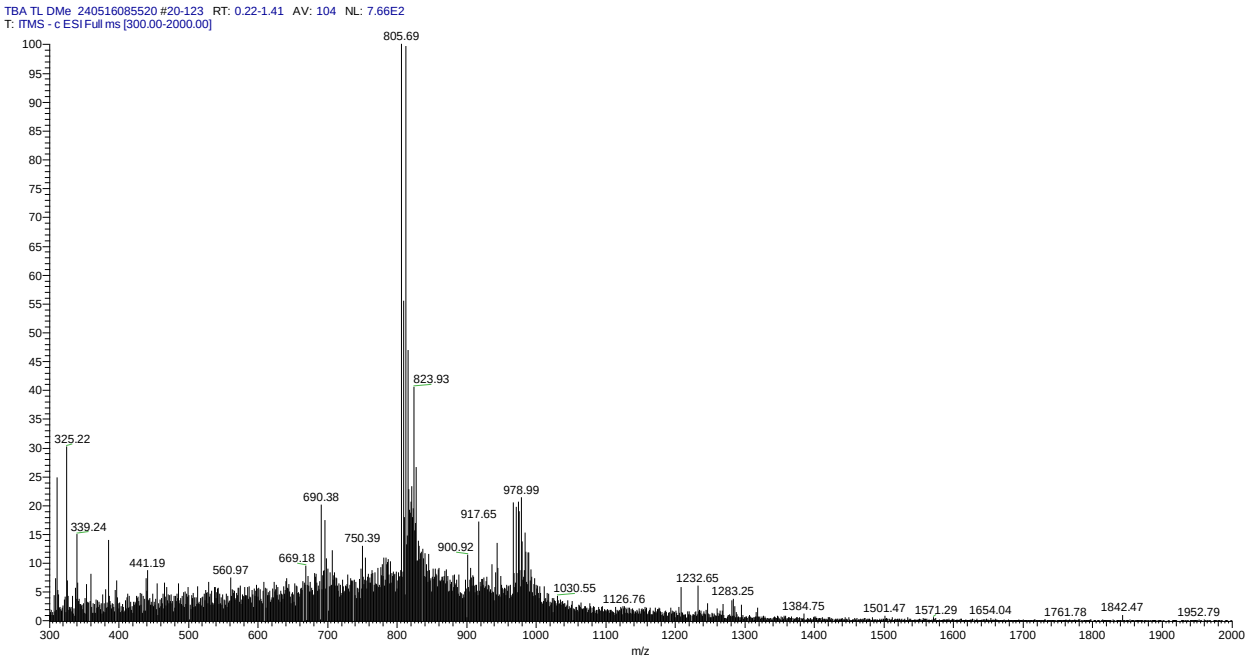

Figure S43. ESI$^-$ MS spectrum for TBA15 T_L DMePhOH6HI.

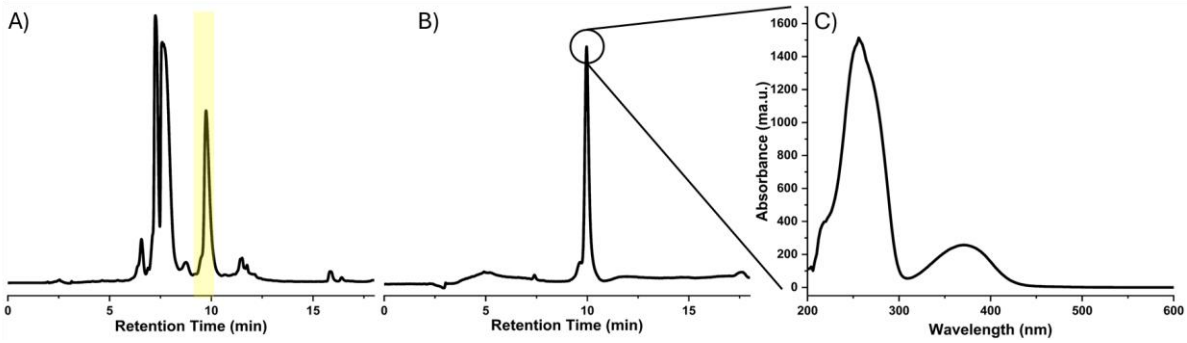

Figure S44. TBA15G8 PhOH A) Crude HPLC trace, post on strand synthesis and ethanol precipitation. Collected fraction is highlighted in yellow. B) HPLC trace of collected, purified product. C) Corresponding UV-Vis Spectra of collected trace.

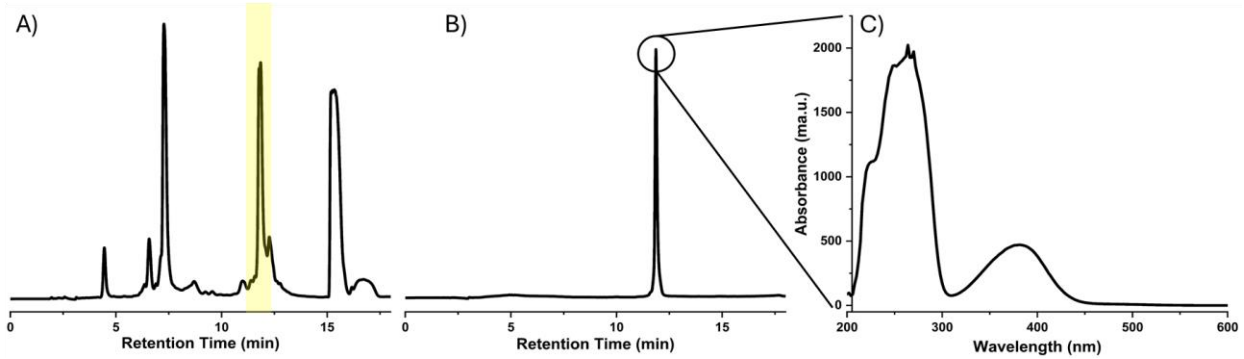

Figure S45. TBA15G8 DMePhOH A) Crude HPLC trace, post on strand synthesis and ethanol precipitation. Collected fraction is highlighted in yellow. B) HPLC trace of collected, purified product. C) Corresponding UV-Vis Spectra of collected trace.

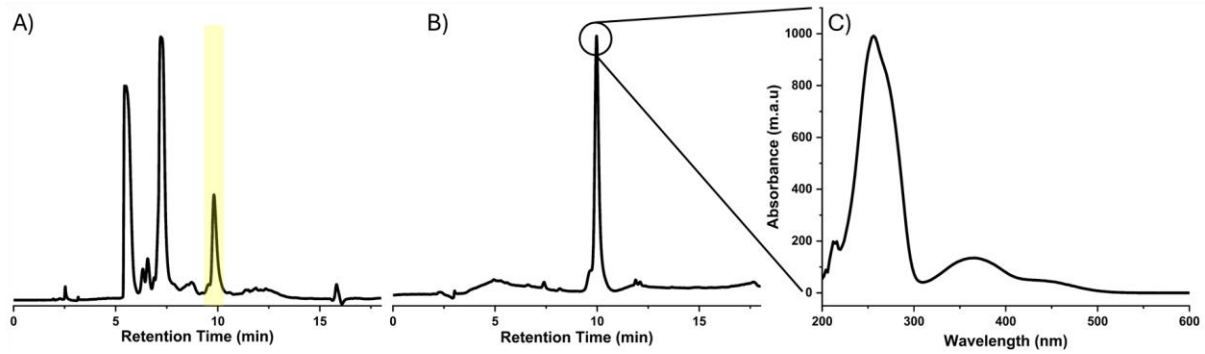

Figure S46. TBA15G8 FPhOH A) Crude HPLC trace, post on strand synthesis and ethanol precipitation. Collected fraction is highlighted in yellow. B) HPLC trace of collected, purified product. C) Corresponding UV-Vis Spectra of collected trace.

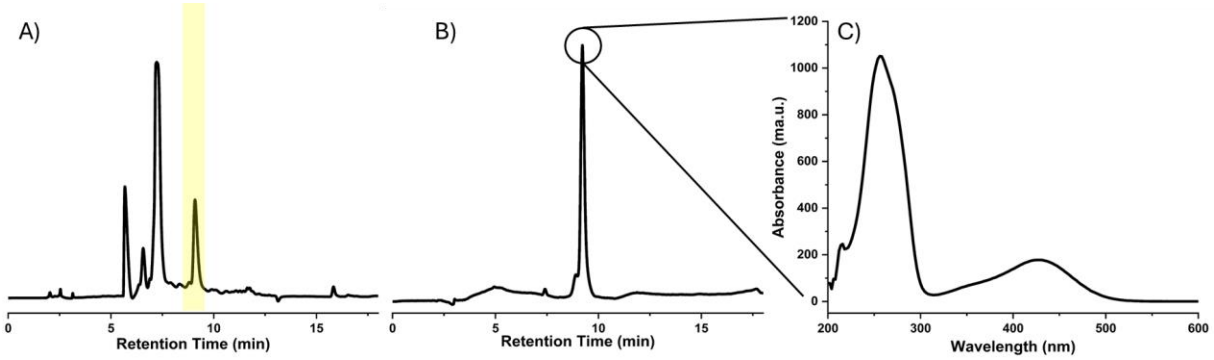

Figure S47. TBA15G8 DFPhOH A) Crude HPLC trace, post on strand synthesis and ethanol precipitation. Collected fraction is highlighted in yellow. B) HPLC trace of collected, purified product. C) Corresponding UV-Vis Spectra of collected trace.

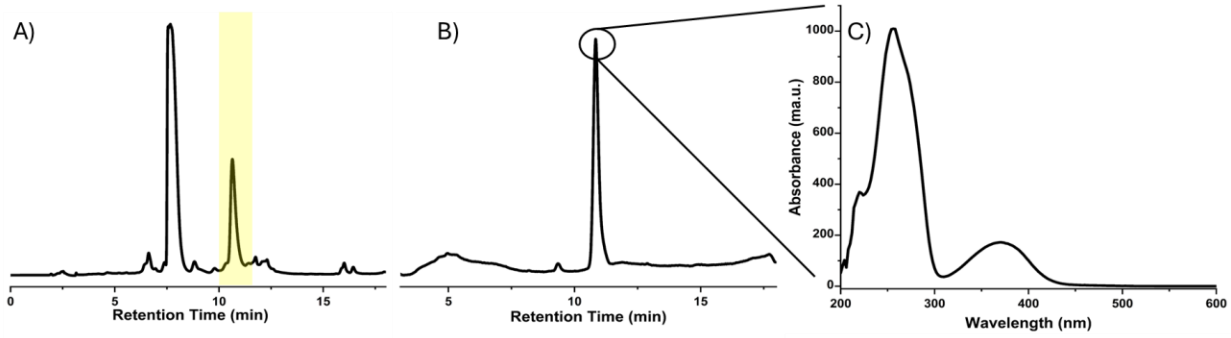

Figure S48. TBA15T$_L$ PhOH A) Crude HPLC trace, post on strand synthesis and ethanol precipitation. Collected fraction is highlighted in yellow. B) HPLC trace of collected, purified product. C) Corresponding UV-Vis Spectra of collected trace.

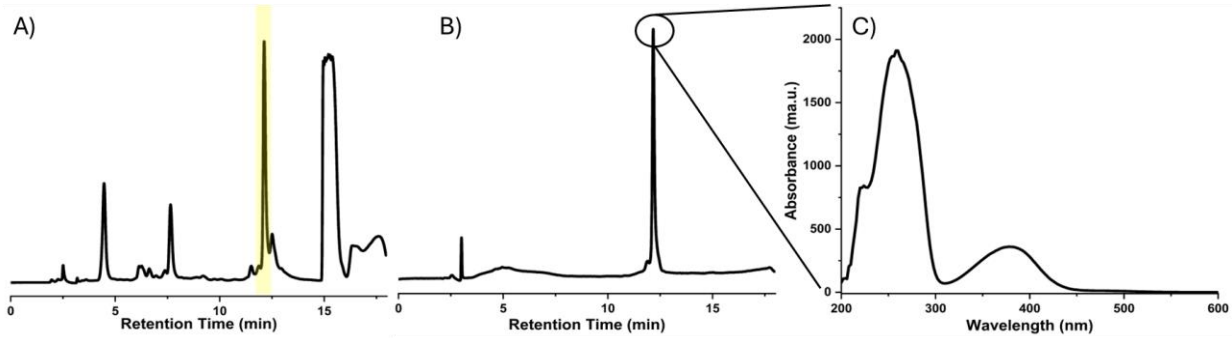

Figure S49. TBA15T$_L$ DMePhOH A) Crude HPLC trace, post on strand synthesis and ethanol precipitation. Collected fraction is highlighted in yellow. B) HPLC trace of collected, purified product. C) Corresponding UV-Vis Spectra of collected trace.

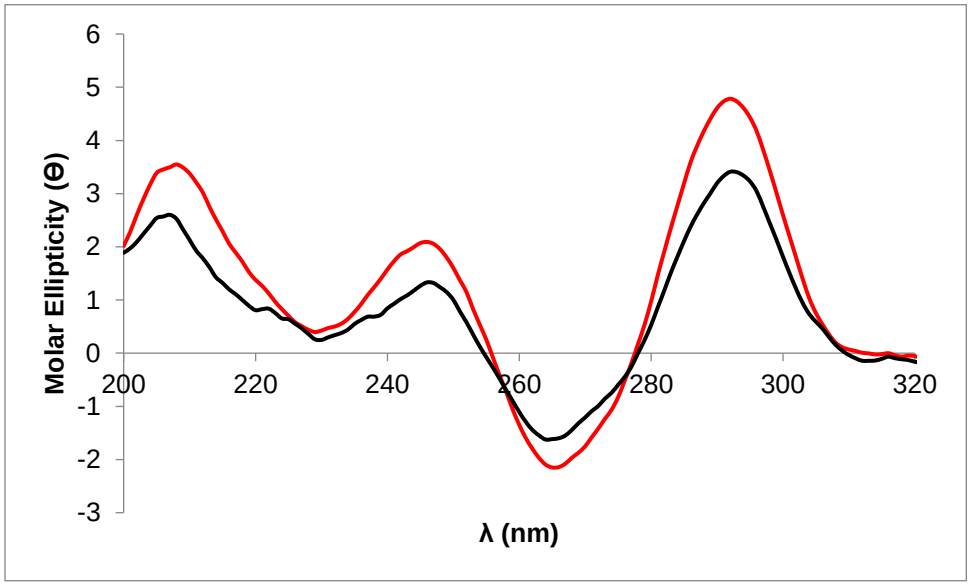

Figure S50. CD spectra for native TBA15 (black trace) vs. G8-DFPhOH6HI-TBA15 (red trace) in 50 mM Tris·HCl, pH 8.0, 50 mM KCl, 50 mM $MgCl_2$, highlighting peaks characteristic of the antiparallel GQ.

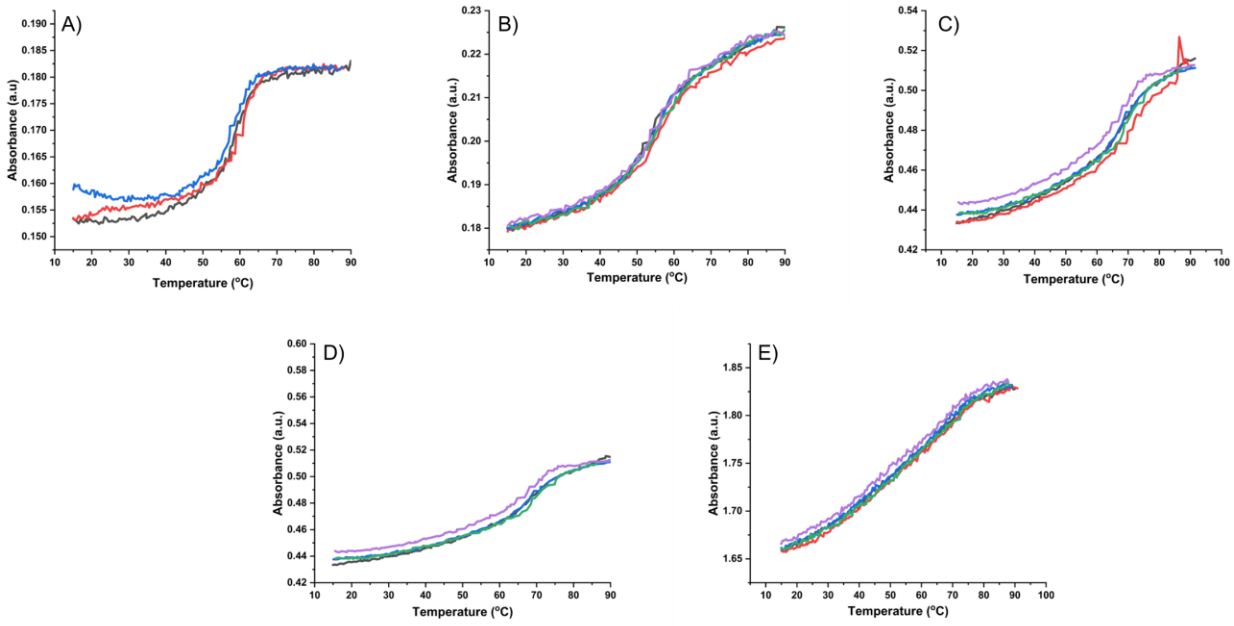

Figure S51. Thermal melting curves for A) TBA15 PhOH with DNA complement, B) TBA15 PhOH with RNA complement, C) TBA15 PhOH with RNA/LNA complement, D) TBA15 T_L PhOH with DNA complement, E) TBA15 T_L PhOH with RNA/LNA complement.

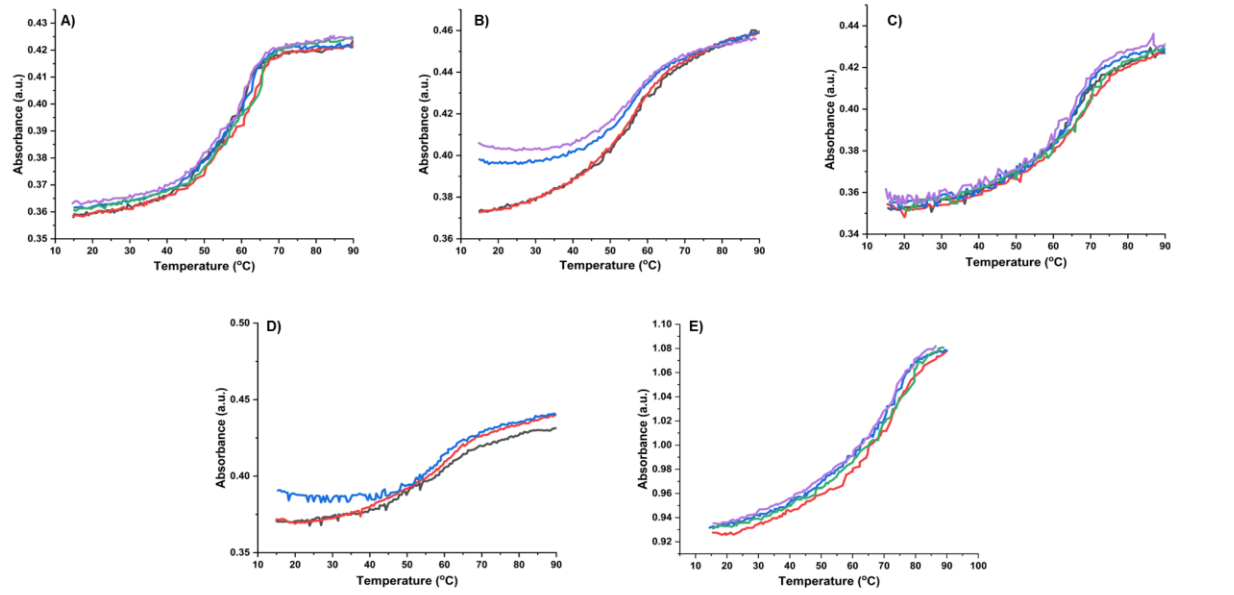

Figure S52. Thermal melting curves for A) TBA15 DMePhOH with DNA complement, B) TBA15 DMePhOH with RNA complement, C) TBA15 DMePhOH with RNA/LNA complement, D) TBA15 T_L DMePhOH with DNA complement, E) TBA15 T_L DMePhOH with RNA/LNA complement.

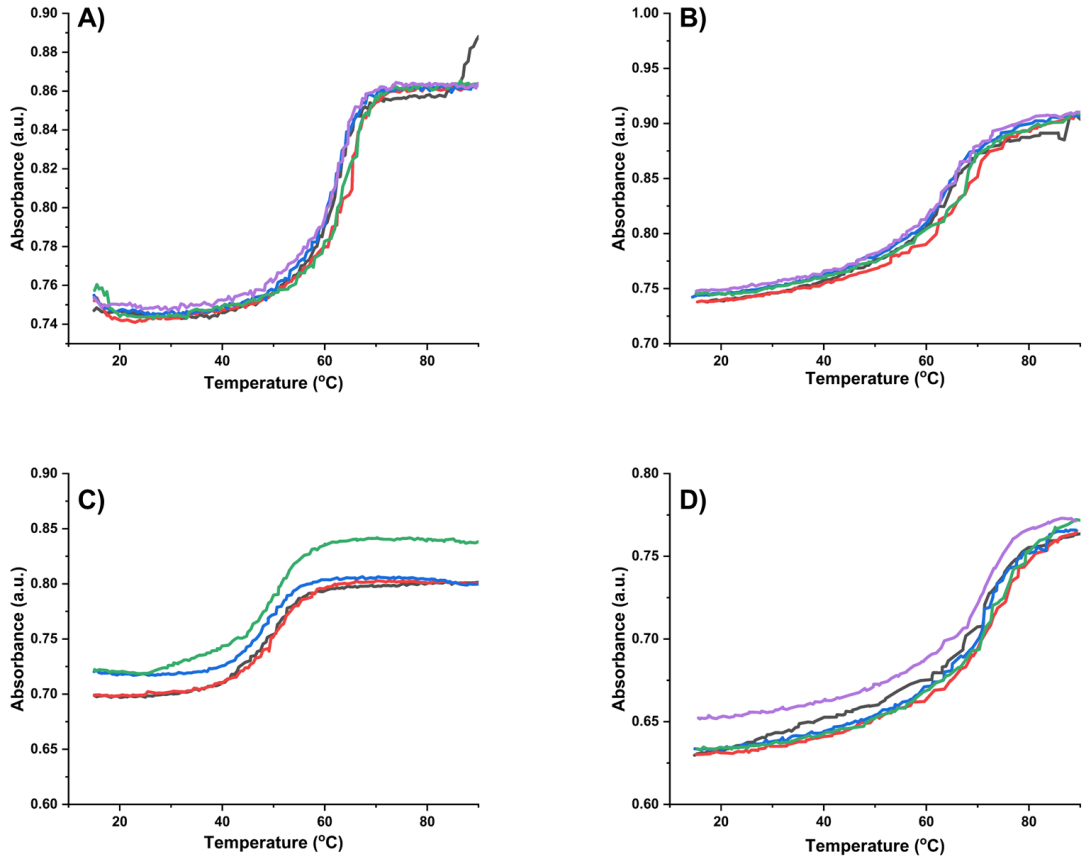

FIgure S53. Thermal melting curves for native TBA15 duplexes with A) DNA complement B) RNA complement C) N-1 complement and D) RNA/LNA complement.

Table S5. Tm values (°C) for TBA15 GQs with probes at the G8-site, λ_{ex} and λ_{em} wavelengths (in nm) for the surrogates and relative emission (I_{rel}).

[G8]	T_m (ΔT_m)[a]	λ_{ex} (nm)	λ_{em} (nm)	I_{rel}[b]
dG	40.1	-	-	-
DFPhOH	48.5 (8.4)	437	565	1.0
FPhOH	46.2 (6.1)	445	564	0.35
DMePhOH	44.3 (4.2)	390	592	0.07
PhOH	45.2 (5.1)	375	561	0.05

[a] T_m values for K^+-TBA15 GQs (2 μM) measured at 295 nm in 25 mM Tris-HCl (pH 8.0, 50 mM KCl, 50 mM $MgCl_2$), heating rate of 0.5 °C min^{-1}, errors are ± 1 °C, ΔT_m = T_m (modified GQ) – 40.1 °C (T_m of native GQ). [b] Relative emission intensity of the modified GQs.

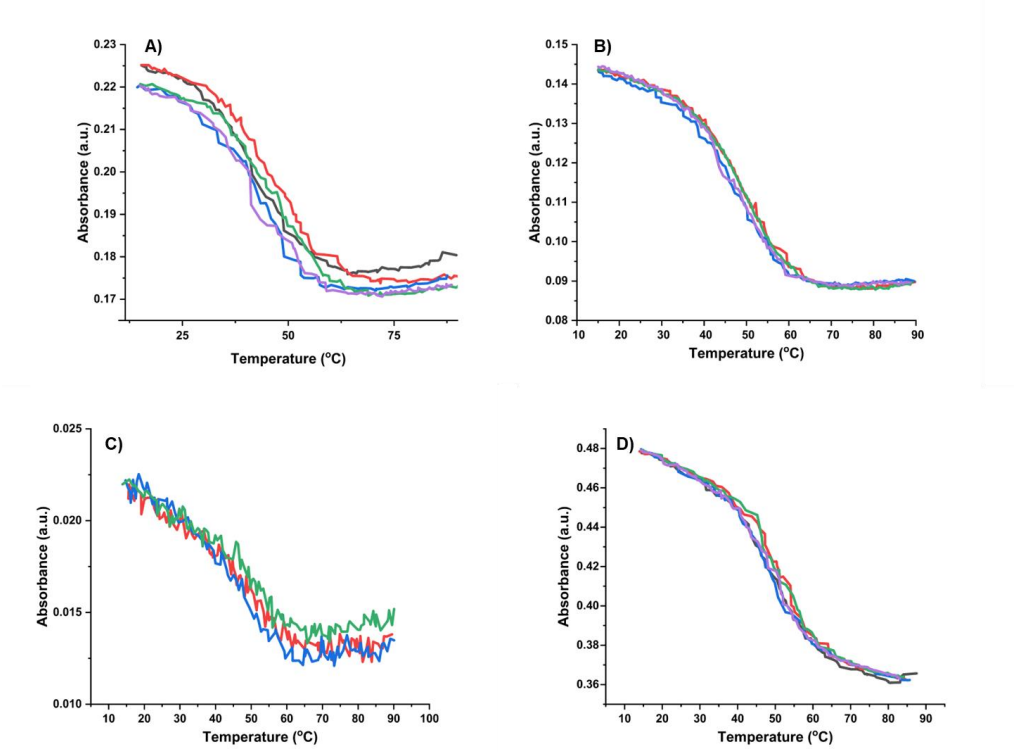

FIgure S54. Thermal melting curves for TBA 15 quadruplexes measured at 295 nm. A) TBA15 PhOH B) TBA15 DMePhOH C) TBA15 FPhOH D) TBA15 DFPhOH

Computational Methodology

Model Building

The starting model of unbound TBA15 (5′–GG-TT-GG-TGT-TT-GG-TT–3′) were extracted from the X-ray crystal structure of TBA bound to thrombin with potassium in the center of the G-tetrad (PDB ID: 4DII).[1] The *S* isomeric form of the dye (PhOH6HI) and the noncanonical nucleic acid residues (2'-OMe-A, 2'-OMe-G, 2'-OMe-C, 2'-OMe-U, LNA-T, and LNA-A) were built using GaussView 6.0.16[2] and the lowest energy conformer found using the technique described in the System Preparation section. The lowest energy conformer of the probe was modeled into TBA15 by aligning the terminal atoms of the dye with that of the dG8 nucleotide which was later deleted in PyMol 3.0.[3] The dye was stacked atop the G-tetrad, as previously described.[4] The duplexes were similarly built with the dye being modeling into *Narl*12 and TBA15, initially constructed with the `fnab` functionality in PyMol 3.0, by replacing dG7 and dG8, respectively. The dye was positioned stacked in the helix, with the carbonyl moiety of the indanone facing the major groove, complementing the natural twist of the duplex, as previously described.[5]

System Preparation

Canonical nucleic acid residues were described using the AMBER force field (OL15). Ion parameters were adopted from Joung and Cheatham for Na^+, Cl^-, and K^+.[6] Each component of the noncanonical nucleic acid residues and dye were first constructed using GaussView 6.0.16.[2] An initial unguided conformational search was performed on the isolated molecules using RDKit with the UFF force field.[7] The 50 lowest energy conformers were further refined with B3LYP[8]-D3 (BJ)[9]/6-31G(d)[10] optimizations performed using Gaussian 16 (C.01).[11] Two structurally distinct minima (conformations) were used for parametrization of the modified nucleotides that correspond to the *syn* and *anti* glycosidic conformations, while three conformations of the dyes were used that capture different low energy backbone conformations. Partial charges were calculated using the PyRED online server,[12] while AMBER atom types were supplemented by GAFF parameters.[13]

Each model was prepared for simulation using the `tleap` module of AMBER 22.[14] Specifically, each system was solvated in a truncated octahedral box of TIP4P-EW water,[15] with the nearest box face being a minimum distance of 10 Å from the solute. Finally, the system was neutralized with Na^+ and brought to a NaCl concentration of 150 mM using the SLTCAP calculator to determine additional ion counts.[16]

Molecular Dynamics Simulation Protocol

Each system was minimized in four stages: 1) solvent and ions were minimized while holding the solute rigid; 2) the hydrogens on the solute were minimized while restraining the rest of the model; 3) all atoms of the solute were minimized while holding the solvent and ions rigid; and 4) the entire system was minimized. Each minimization stage involved 2,000 cycles of steepest descent followed by 2,000 steps of conjugate gradient minimization. At each sub-step, a force constant of 100.0 kcal·mol^{-1}Å^{-2} was used to apply restraints. Heating was next carried out to bring the systems from 0 K to 310 K in 50 K increments, starting at 10 K and using 20,000 steps of heating per segment. The solute was restrained using a 25 kcal·mol^{-1}Å^{-2} force constant during heating. Lastly, five equilibration steps were performed which decreased the restraint on the solute from 20 to 15, 10, 5, and finally to 1.5 kcal·mol^{-1}Å^{-2}. Each of the five rounds of equilibration was run for 10,000 steps. The time step for all minimization, heating, and equilibration was 1 fs. During production, the SHAKE algorithm was used,[17] allowing for a time step of 2 fs.

Each of the 7 *Narl*12 DS models (Figure S13, S15), the 4 TBA15 DS models, and the TBA15 GQ (Figure S14, S16) was simulated in triplicate for 1 μs, which resulted in 3 μs of total simulation time for each system. Each simulation was run as an NPT ensemble at 310 K (using the Langevin thermostat)[18] at 1 bar of pressure (Berendsen barostat),[19] a water density of 0.997 g/mL, and the periodic boundary condition enabled. Frames were saved to disk every 20 ps for analysis, resulting in a total of 20,000 frames per simulation replica. To ensure the integrity of duplexes, restraints were applied to the terminal ends. Specifically, no force was applied when the distances were between 1.80 Å and 3.40 Å. A restoring force is enabled beyond these distances with a maximum application of force (20 kcal·mol^{-1}Å^{-2}) is applied beyond 1.30 Å and 3.90 Å.

Molecular Dynamics Simulation Analysis Protocol

Simulations were analyzed using `cpptraj` from the AMBER suite and a collection of inhouse scripts. Analysis was conducted over the 1 μs of each replica for each system and reported as averages with standard deviations over the dataset.

Trajectory analysis included evaluation of the root-mean-square deviations (RMSDs) of all heavy atoms, each residue, and nucleotide backbone atoms (P, O5′, C5′, C4′, C3′, O3′), and per-residue root-mean-square fluctuation (RMSF). Backbone dihedral angles were calculated, including α = ∠(O3′5′$^{-base}$, P, O5′, C5′), β = ∠(P, O5′, C5′, C4′), γ = ∠(O5′, C5′, C4’, C3’), and δ = ∠(C5′, C4′, C3′, O3′). Hydrogen-bonding occupancies were calculated based on a distance cut-off of < 3.2 Å and an angle cut-off of > 130°. Stacking occupancies were calculated based on the center of mass between the aromatic rings being closer than 5 Å and having an inter-planar angle being < 30° or > 150°. For each duplex system, hierarchical agglomerative clustering was carried out with respect to the RMSD of the dye, and heavy atoms of the flanking nucleotides and opposing nucleotide, if precent. In the case of the TBA15 GQ, hierarchical agglomerative clustering was carried out with respect to the RMSD of the dye, dG1, dG6, dT7, dT9, dG10, and dG15. The clustered structures are supplied as .pdb files. Due to difficulties identifying modified nucleotides with standard tools, helical parameters were calculated using a pseudo-step between the 5′ and 3′-base pairs flanking the probe, which were established using the `vector` and `vectormath` functions in `cpptraj`.

Density Functional Theory Calculations on Free dyes

All density functional theory (DFT) and time-dependent density functional theory (TD-DFT) calculations were performed with the Gaussian 16 C.01 suite of programs.[11] The ground state geometries were optimized using the ωB97X-D functional,[20] with the double-ζ basis set Def2-SVP.[21] Solvent effects (solvent = Water) were considered and involved in all geometry optimizations using the SMD (solvent = Water) model.[22] For a given stationary point, the geometry which gave the lowest energy was selected to represent that compound. Harmonic vibrational frequencies were computed to verify the nature of each stationary point (i.e., all local minima have only real (positive) frequencies). Single-point energies were calculated at the SMD-ωB97X-D[20]/Def2-TZVP[21] level of theory to get more accurate molecular orbital energies. The optimized geometries are available in the supplied .xyz file.

The excited state geometries were optimized with TD-DFT at the ωB97X-D[20]/Def2-SVPP[21] level of theory. The linear response (LR-SMD)[22] formalism for was used for geometry optimization and the corrected linear response (cLR-SMD)[23] was used to calculate the energy in water. To calculate the electronic energy of the 90° twisted intramolecular charge transfer state, the dihedral angle was frozen to ensure the desired dihedral angle. The vertical excitation and deexcitation energies were calculated using the optimized geometries at the M06[24]/Def2-TZVP[21] level of theory using the corrected linear response (cLR-SMD).[23]

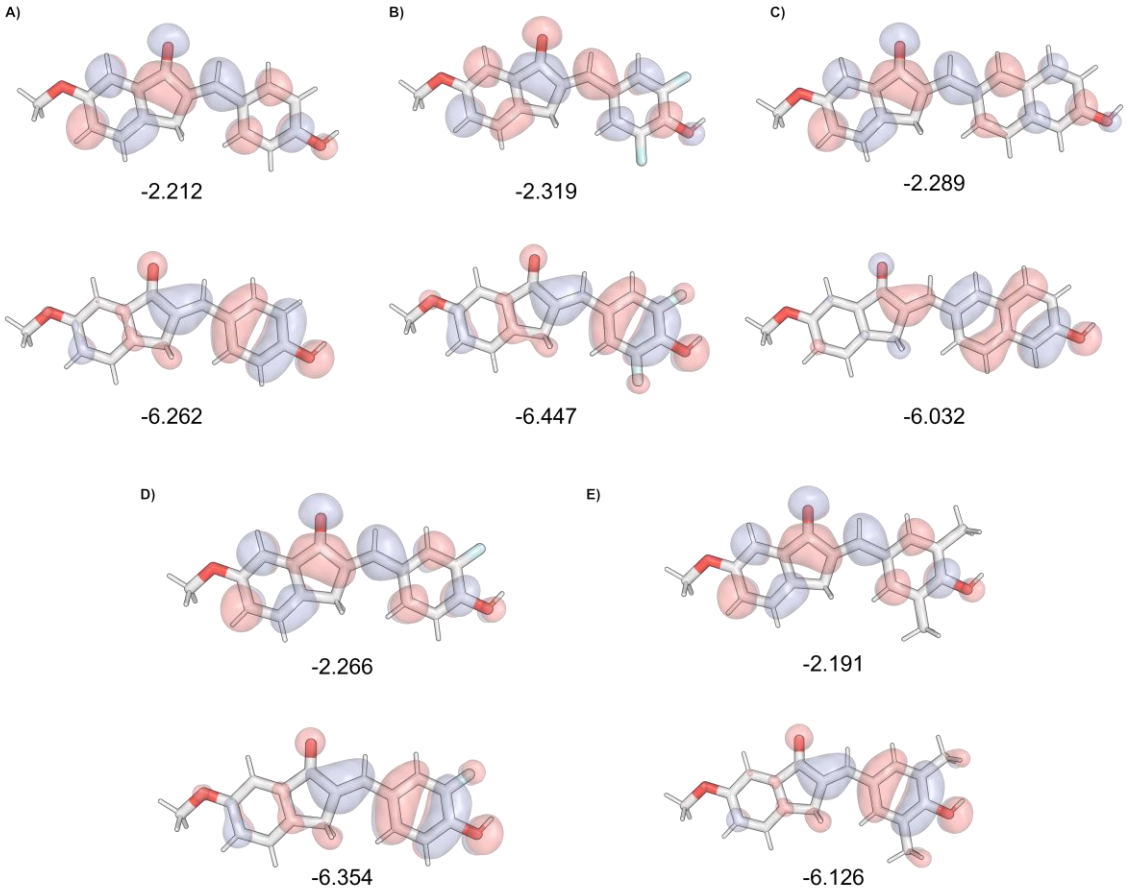

Figure S55. Frontier molecular orbitals (HOMO and LUMO) and their energy gap, in eV, for neutral A) PhOH6HI, B) DFPhOH6HI, C) NapOH6HI, D) FPhOH6HI, E) DMePhOH6HI. Calculations are at the SMD-M06/Def2-TZVP // SMD-ωB97XD/Def2-SVP (water) level of theory.

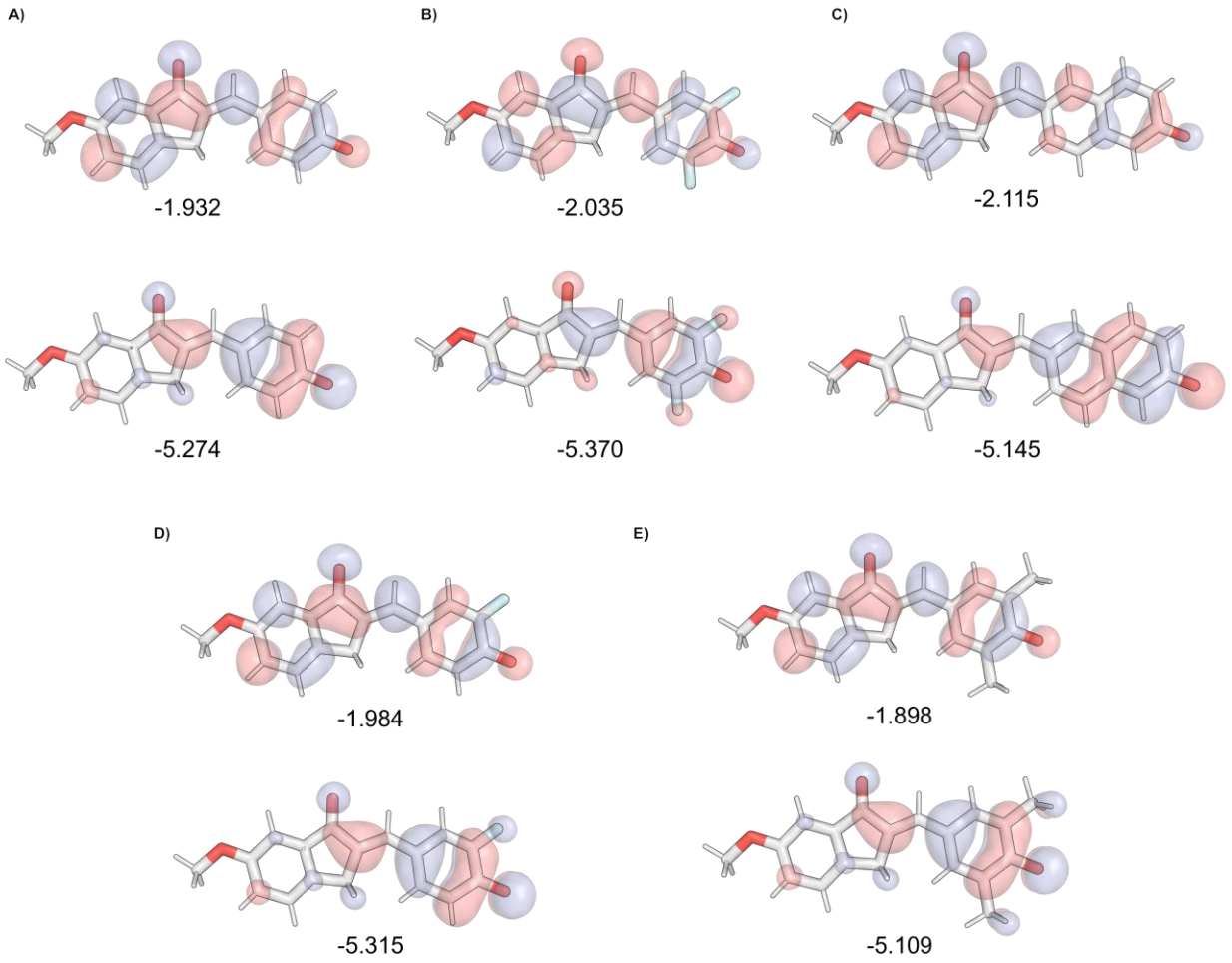

Figure S56. Frontier molecular orbitals (HOMO and LUMO) and their energy gap, in eV, for deprotonated A) PhOH6HI, B) DFPhOH6HI, C) NapOH6HI, D) FPhOH6HI, E) DMePhOH6HI. Calculations are at the SMD-M06/Def2-TZVP // SMD-ωB97XD/Def2-SVP (water) level of theory.

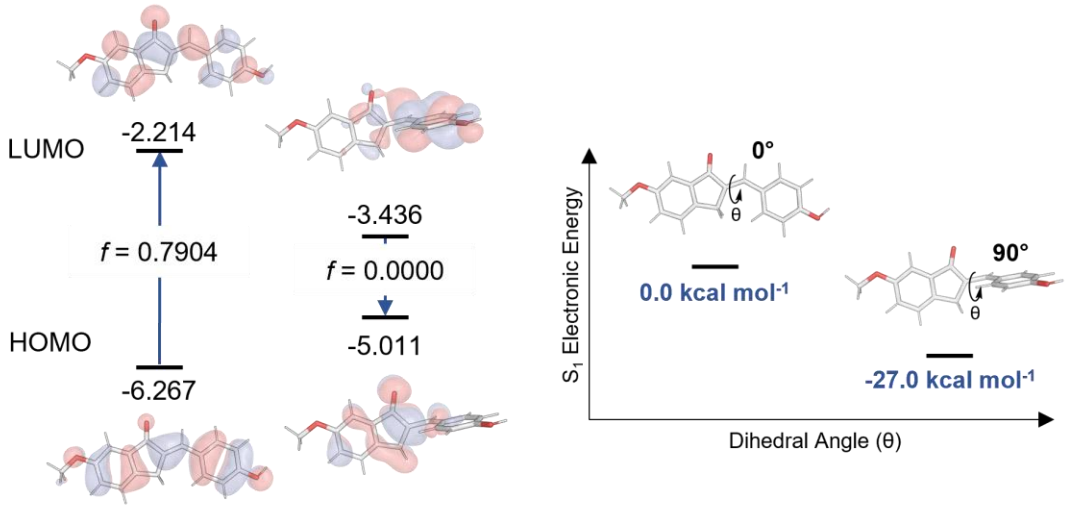

Figure S57. Optimized molecular structures, LUMO, HOMO, and relative energy levels of the ground (S_0) and excited (S_1) states during light absorption (Frank-Condon), and emission (TICT) in water, as evaluated at the SMD-ωB97X-D/Def2-TZVP // SMD-ωB97X-D/Def2-SVP (water) level of theory. The S_1 species at θ = 0° was freely allowed to optimize, but the θ = 90° species had its dihedral frozen during optimization.

Density Functional Theory Calculations on DNA-Dye Complexes

All DFT and TD-DFT calculations were performed with the Gaussian 16 C.01 suite of programs.[11] Initially, hierarchical agglomerative clustering was carried out with respect to the RMSD of the dye with dT8 and dA17 (TXT context) or dG8 and dC17 (GXG context) from the MD simulations. The clustered structures was then subject to ground state geometry optimization using the ωB97X-D functional,[20] with the double-ζ basis set Def2-SVP.[21] Solvent effects (solvent = Water) were considered and involved in all geometry optimizations using the SMD (solvent = Water) model.[22] Single-point energies were calculated at the SMD-ωB97X-D[20]/Def2-TZVP[21]. The vertical excitation was calculated with TD-DFT with the optimized ground-state geometry at the SMD-ωB97X-D[20]/Def2-TZVP[21] level of theory.

DFT calculations on the entire PhOH6HI-modified TBA15 were carried out using ORCA 6.0.0.[25–27] Starting with a hierarchical agglomerative clustered geometry obtained from the MD simulation, a geometry optimization at the semi-empirical GFN2-xTB[28] level of theory with implicit solvation of water specified using the CPCMX model.[29] Harmonic vibrational frequencies were computed to verify the nature of each stationary point (i.e., all local minima have only real (positive) frequencies). Single-point energies were calculated at the CPCM[30]-ωB97X-D[20]/Def2-SVP[21] level of theory to get more accurate molecular orbital energies. The calculations were accelerated using the resolution of identity approximation (RI) for the Coulomb integrals,[31] while the exchange terms were efficiently computed using the 'chain-of-spheres' (COSX) approximation[32] with the Def2/J auxiliary basis set.[33] Converged SCF orbitals were obtained using the `VeryTightSCF` setting in ORCA (energy change = 10^{-9} Eh).

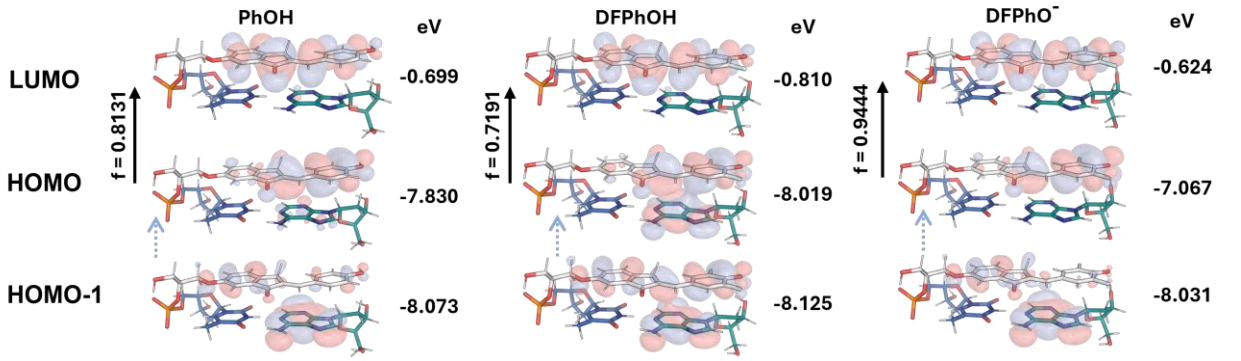

Figure S58. Minimum energy structures for PhOH, DFPhOH, and DFPhO– flanked by dT as evaluated at the SMD-ωB97X-D/Def2-TZVP // SMD-ωB97X-D/Def2-SVP (water) level of theory with their HOMO-1, HOMO, and LUMO energy levels (isovalue = 0.02). The oscillator strength *f* ($S_0 \rightarrow S_1$) was determined through a TD-DFT calculation at the SMD-ωB97X-D/Def2-TZVP level of theory.

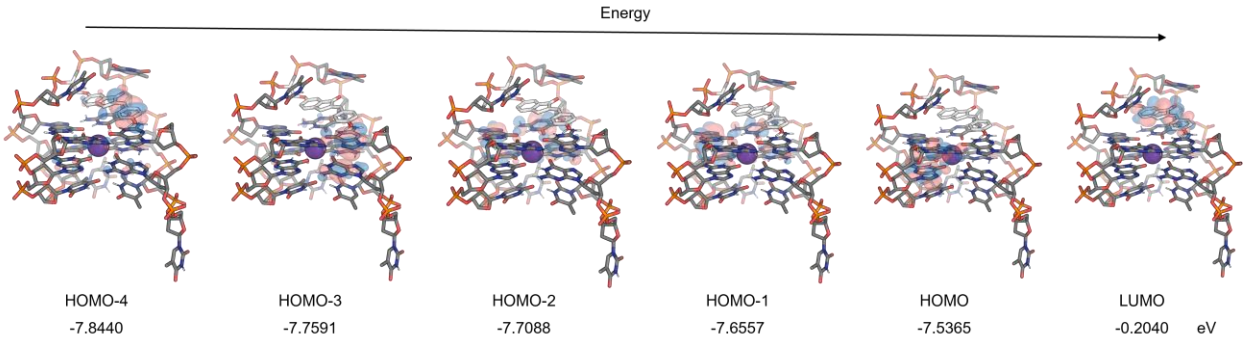

Figure S59. Minimum energy structure of PhOH6HI-modifed TBA15 GQ with K^+ as evaluated at the CPCM-ωB97X-D/Def2-SVP // CPCMX-GFN2-xTB (water) level of theory with the HOMO-4, HOMO-3, HOMO-2, HOMO-1, and LUMO energy levels (isovalue = 0.02). Similar to our other DFT calculations on the duplexes, the push-pull character of the probe can be visualized through the MO isosurfaces. The MO centered on the phenolic donor (HOMO-4) and the MO centered on the indanone acceptor (LUMO) are likely the orbitals involved in the photoexcitation. We predict there are several MOs higher in energy than HOMO-4. The HOMO-3 centered on DG5 is likely the source of PET quenching due to the higher energy, proximity, and good orbital overlap with HOMO-4.

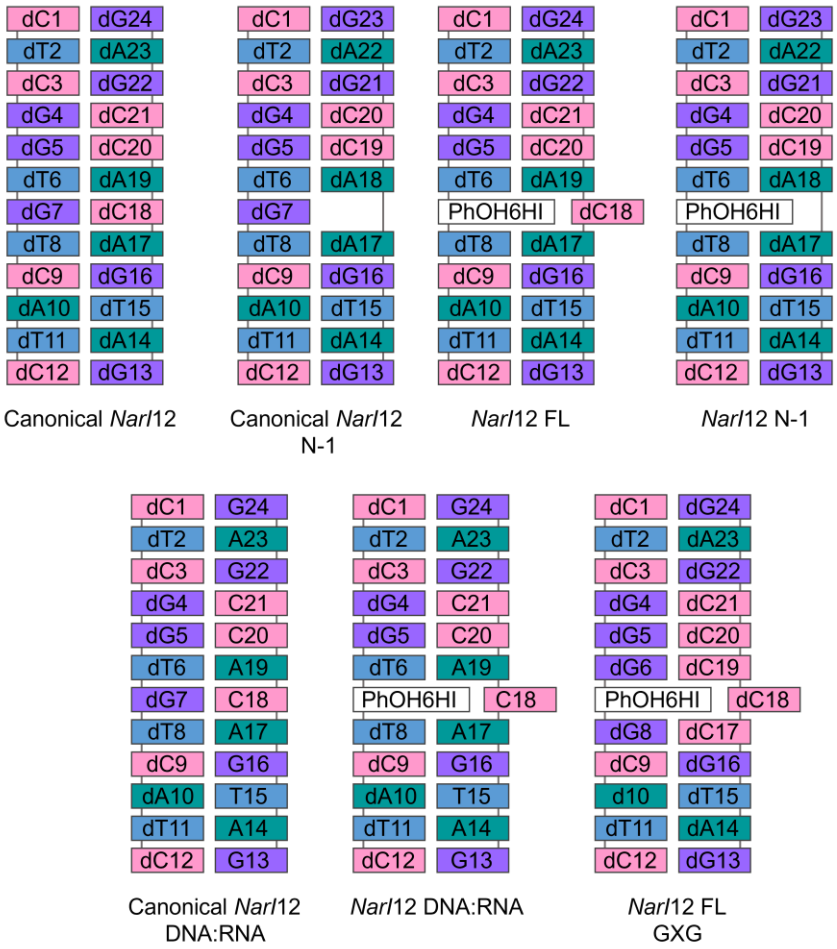

Figure S60. Schematics of the *Narl*12 DS systems considered in the present study, including residue numbering.

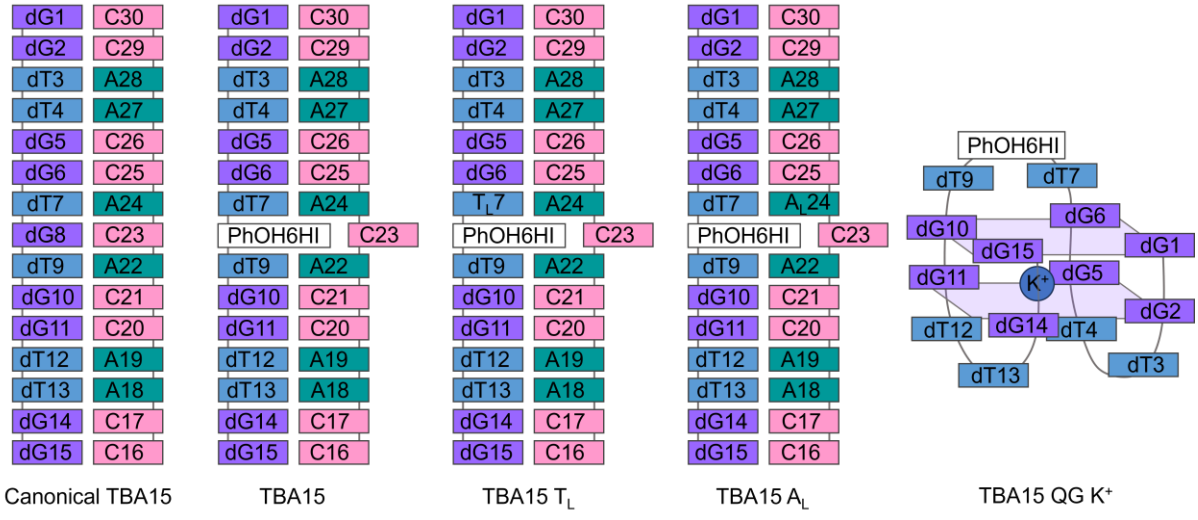

Figure S61. Schematics of the TBA15 DS and TBA15 GQ K^+ systems considered in the present study, including residue numbering.

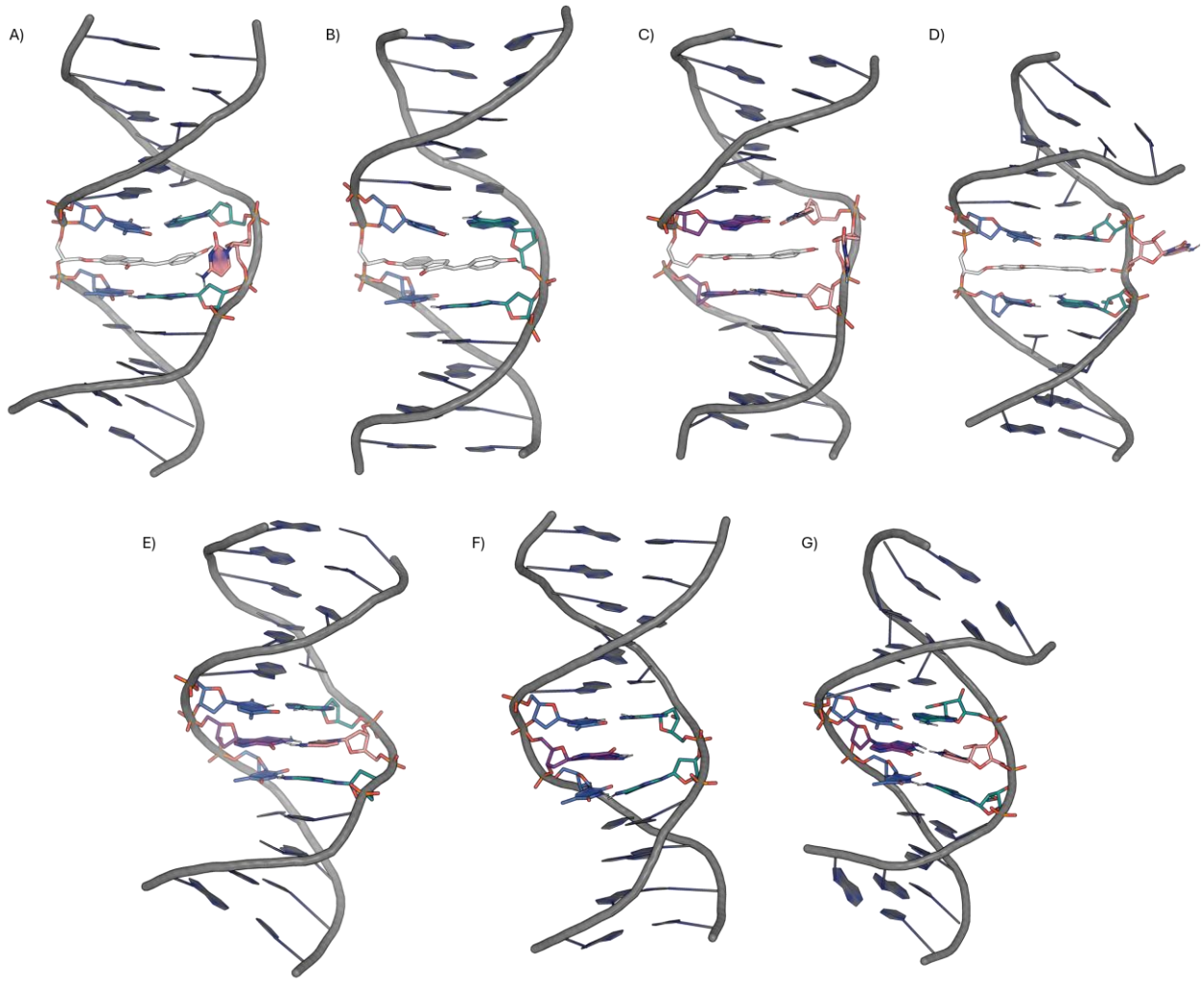

Figure S62. Representative MD structures of *Narl*12 containing A) PhOH6HI (grey) at *G7* opposite dC18 (pink), B) PhOH6HI (grey) at *G7* opposite N-1, C) PhOH6HI (grey) at *G7* flanked by dG6 and dG8, D) PhOH6HI (grey) at *G7* opposite 2'-OMe C18, E) canonical nucleotide dG7 (purple) opposite dC18 (pink), F) canonical nucleotide dG7 (purple) opposite a N-1, and G) canonical nucleotide dG7 (purple) opposite 2'-OMe C18 (pink). Sequences shown as cartoon for residues distal to the modification site and stick representation for the G7:C18 and flanking base pairs. Water, ions, and non-polar hydrogens hidden for clarity.

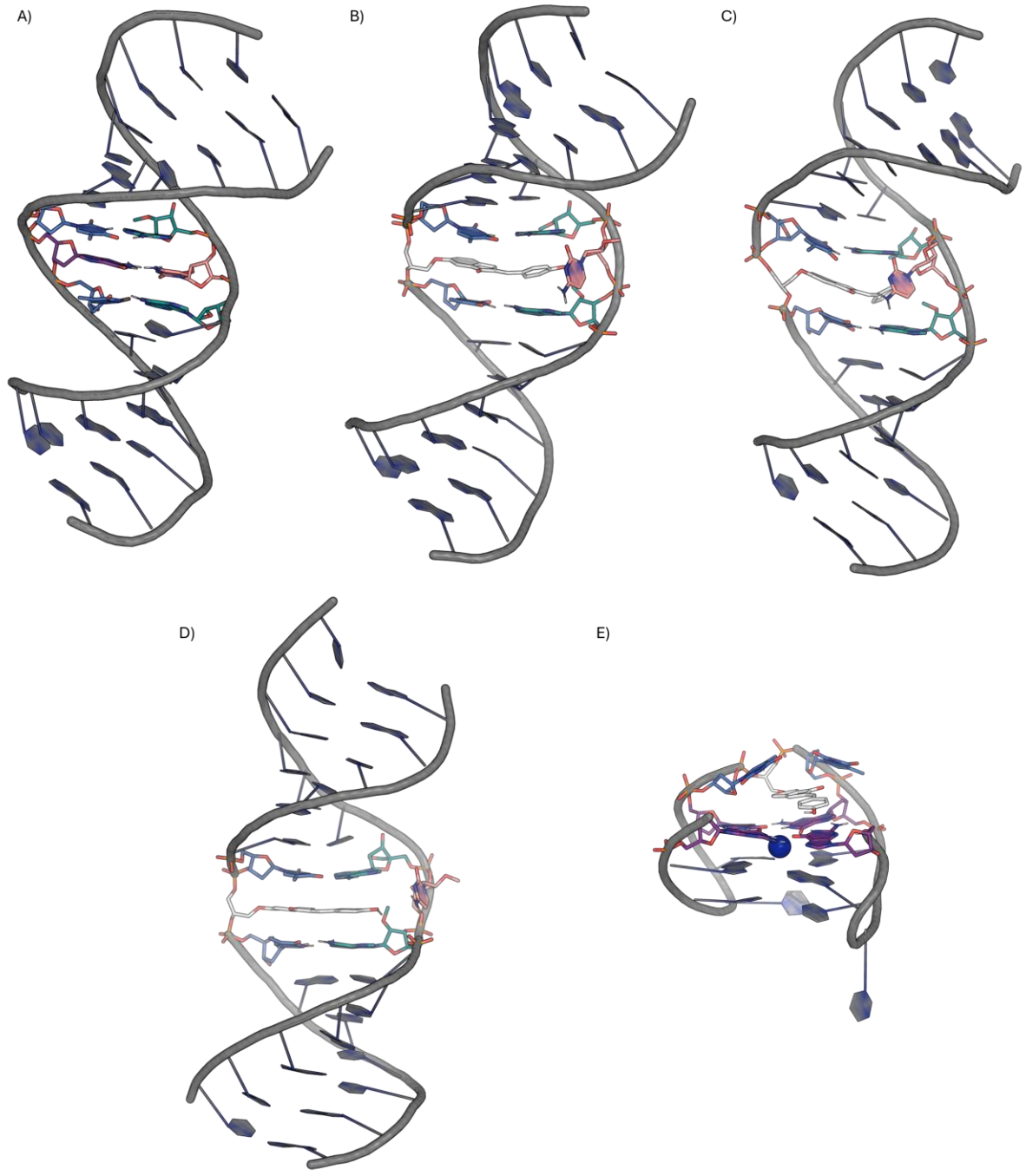

Figure S63. Representative MD structures of TBA15 containing A) canonical nucleotides dG8 (purple) opposite dC18 (pink), B) PhOH6HI (grey) at *G8* opposite C23 (pink), C) PhOH6HI (grey) at *G8* opposite C23 (pink) flanked by T_L7, D) PhOH6HI (grey) at *G8* flanked by A_L24, and E) PhOH6HI (grey) at *G8* in the TBA15 GQ with K^+. Sequences shown as cartoon for residues distal to the modification site and stick representation for the G8:C23 and flanking/neighbouring base pairs. Water, ions, and non-polar hydrogens hidden for clarity.

Table S6. Helical twist (deg.) for *Narl*12 systems (std. dev in paratheses).

Base pair	*Narl*12 Canonical	*Narl*12 N-1 Canonical	*Narl*12 FL	*Narl*12 N-1	*Narl*12 DNA:RNA *(no dye)*	*Narl*12 DNA:RNA	GXG *Narl*12
5-6	36.0 (5.5)	34.4 (5.4)	37.8 (9.2)	35.4 (8.2)	30.1 (3.8)	35.5 (4.5)	41.7 (5.2)
6-7	24.4 (3.2)	48.4 (9.6) [a]	31.2 (15.7) [a]	37.2 (8.6) [a]	30.7 (4.5)	14.1 (3.7)[a]	28.4 (8.9) [a]
7-8	32.2 (5.1)				29.9 (5.1)		
8-9	35.6 (5.0)	34.2 (6.4)	33.3 (5.1)	30.9 (6.3)	29.3 (5.7)	28.1 (4.7)	31.8 (5.5)

[a] The twist from pairs 6-8.

Table S7. Helical twist (deg.) for TBA15 systems (std. dev in paratheses).

Base pair	TBA15 Canonical	TBA15	TBA15 A_L	TBA15 T_L
5-6	29.6 (4.0)	34.3 (3.7)	32.4 (3.8)	32.0 (4.0)
6-7	31.2 (4.6)	36.4 (8.9)[a]	29.3 (11.8)[a]	34.6 (9.4)[a]
7-8	30.2 (4.7)			
8-9	31.2 (5.0)	30.4 (5.2)	30.1 (4.9)	27.9 (4.5)

[a] The twist from pairs 7-9.

Table S8. Rise, in angstroms, for *Narl*12 systems (std. dev in paratheses).

Base pair	*Narl*12 Canonical	*Narl*12 N-1 Canonical	*Narl*12 FL	*Narl*12 N-1	*Narl*12 DNA:RNA *(no dye)*	*Narl*12 DNA:RNA	GXG *Narl*12
1-2	4.2 (0.4)	4.2 (0.4)	4.2 (0.4)	4.2 (0.4)	4.2 (0.5)	4.2 (0.5)	4.2 (0.4)
2-3	4.0 (0.4)	4.0 (0.4)	4.0 (0.4)	4.0 (0.4)	3.9 (0.3)	4.0 (0.5)	4.0 (0.4)
3-4	4.3 (0.4)	4.3 (0.4)	4.3 (0.4)	4.3 (0.4)	4.9 (0.4)	5.0 (0.5)	4.2 (0.4)
4-5	4.1 (0.3)	4.1 (0.3)	4.2 (0.3)	4.2 (0.3)	4.3 (0.2)	4.3 (0.2)	4.1 (0.3)
5-6	3.8 (0.2)	3.8 (0.3)	3.9 (0.3)	4.3 (0.8)	3.9 (0.3)	4.0 (0.3)	3.9 (0.3)
6-7	4.3 (0.4)	5.9 (2.7)	NA	NA	4.6 (0.4)	NA	NA
7-8	3.9 (0.3)	5.1 (2.6)	NA	NA	3.8 (0.3)	NA	NA
8-9	3.9 (0.3)	4.3 (0.8)	3.9 (0.3)	4.0 (0.3)	4.0 (0.4)	4.1 (0.3)	3.8 (0.3)
9-10	4.6 (0.4)	4.6 (0.5)	4.6 (0.4)	4.6 (0.4)	4.7 (0.3)	4.8 (0.3)	4.4 (0.4)
10-11	3.8 (0.2)	3.8 (0.2)	3.8 (0.2)	3.8 (0.2)	3.7 (0.2)	3.8 (0.2)	3.7 (0.2)
11-12	4.0 (0.4)	4.0 (0.4)	4.0 (0.4)	4.0 (0.4)	4.1 (0.3)	4.2 (0.3)	4.0 (0.3)
13-14	4.1 (0.3)	4.1 (0.4)	4.1 (0.3)	4.1 (0.3)	4.4 (0.3)	4.4 (0.3)	4.1 (0.3)
14-15	3.7 (0.2)	3.7 (0.2)	3.7 (0.2)	3.7 (0.2)	3.8 (0.2)	3.8 (0.2)	3.7 (0.2)
15-16	4.1 (0.4)	4.2 (0.4)	4.2 (0.4)	4.2 (0.4)	4.6 (0.3)	4.6 (0.3)	4.3 (0.4)
16-17	4.1 (0.3)	4.1 (0.4)	4.2 (0.4)	4.1 (0.3)	4.3 (0.3)	4.3 (0.3)	3.8 (0.3)
17-18	3.7 (0.2)	4.6 (1.1)	NA	NA	3.9 (0.2)	NA	NA
18-19	4.5 (0.4)	3.8 (0.3)	NA	NA	4.7 (0.3)	NA	NA
19-20	3.7 (0.3)	4.0 (0.4)	3.7 (0.3)	4.0 (0.4)	3.8 (0.2)	3.8 (0.2)	4.2 (0.4)
20-21	4.1 (0.4)	4.2 (0.4)	4.0 (0.3)	4.2 (0.4)	4.4 (0.3)	4.4 (0.3)	4.0 (0.4)
21-22	4.3 (0.4)	4.0 (0.3)	4.2 (0.4)	4.0 (0.3)	4.6 (0.4)	4.6 (0.4)	4.3 (0.3)
22-23	4.0 (0.3)	3.9 (0.3)	4.0 (0.3)	3.9 (0.3)	4.3 (0.3)	4.2 (0.3)	4.0 (0.3)
23-24	3.9 (0.3)	NA	3.9 (0.3)	NA	4.4 (0.4)	4.5 (0.8)	3.9 (0.3)

Table S9. Rise, in angstroms, for TBA15 systems (std. dev in paratheses).

Base pair	TBA15 Canonical	TBA15	TBA15 A_L	TBA15 T_L
1-2	4.2 (0.3)	4.2 (0.3)	4.2 (0.3)	4.3 (0.5)
2-3	3.9 (0.3)	3.9 (0.3)	3.8 (0.3)	3.8 (0.3)
3-4	4.1 (0.3)	4.0 (0.3)	4.0 (0.4)	4.1 (0.3)
4-5	4.7 (0.3)	4.6 (0.3)	4.7 (0.3)	4.6 (0.3)
5-6	4.3 (0.3)	4.3 (0.3)	4.2 (0.2)	4.2 (0.3)
6-7	3.8 (0.2)	4.0 (0.3)	4.0 (0.3)	3.8 (0.3)
7-8	4.6 (0.4)	NA	NA	NA
8-9	3.7 (0.2)	NA	NA	NA

9-10	4.6 (0.4)	4.5 (0.4)	4.4 (0.4)	4.5 (0.4)
10-11	4.3 (0.2)	4.2 (0.3)	4.3 (0.2)	4.3 (0.3)
11-12	3.9 (0.2)	3.9 (0.3)	3.9 (0.2)	3.9 (0.3)
12-13	4.1 (0.3)	4.1 (0.3)	4.1 (0.3)	4.1 (0.3)
13-14	4.5 (0.3)	4.5 (0.3)	4.5 (0.3)	4.5 (0.3)
14-15	4.3 (0.3)	4.3 (0.3)	4.3 (0.3)	4.3 (0.3)
16-17	4.4 (0.3)	4.4 (0.3)	4.4 (0.3)	4.3 (0.3)
17-18	4.7 (0.3)	4.7 (0.3)	4.7 (0.4)	4.7 (0.3)
18-19	4.1 (0.2)	4.1 (0.2)	4.1 (0.2)	4.1 (0.2)
19-20	3.8 (0.2)	3.9 (0.3)	3.9 (0.2)	3.9 (0.2)
20-21	4.4 (0.3)	4.5 (0.4)	4.4 (0.3)	4.5 (0.4)
21-22	4.9 (0.5)	4.7 (0.4)	4.9 (0.3)	4.7 (0.4)
22-23	3.8 (0.2)	NA	NA	NA
23-24	4.7 (0.4)	NA	NA	NA
24-25	3.8 (0.2)	3.7 (0.2)	3.8 (0.2)	3.8 (0.2)
25-26	4.4 (0.3)	4.2 (0.3)	4.3 (0.3)	4.2 (0.3)
26-27	4.9 (0.4)	4.8 (0.4)	4.9 (0.5)	4.7 (0.3)
27-28	4.2 (0.3)	4.2 (0.3)	4.3 (0.3)	4.2 (0.2)
28-29	4.0 (0.3)	4.0 (0.3)	4.0 (0.3)	4.0 (0.3)
29-30	4.2 (0.3)	4.2 (0.4)	4.2 (0.3)	4.3 (0.3)

Table S10. P′ to P′ distance, in angstroms, for *Narl*12 systems (std. dev in paratheses).

Base pair	*Narl*12 Canonical	*Narl*12 N-1 Canonical	*Narl*12 FL	*Narl*12 N-1	*Narl*12 DNA:RNA *(no dye)*	*Narl*12 DNA:RNA	GXG *Narl*12
2-3	6.7 (0.3)	6.7 (0.3)	6.7 (0.3)	6.8 (0.3)	6.6 (0.3)	6.6 (0.3)	6.8 (0.3)
3-4	6.7 (0.3)	6.7 (0.3)	6.7 (0.3)	6.7 (0.3)	6.7 (0.3)	6.7 (0.3)	6.7 (0.3)
4-5	6.9 (0.3)	6.9 (0.3)	6.9 (0.3)	6.8 (0.3)	6.9 (0.3)	6.9 (0.3)	6.8 (0.3)
5-6	6.9 (0.3)	6.9 (0.3)	6.9 (0.3)	6.8 (0.3)	6.6 (0.3)	6.8 (0.3)	7.0 (0.3)
6-7	6.8 (0.3)	6.5 (0.4)	6.1 (0.4)	6.3 (0.4)	6.7 (0.3)	6.1 (0.4)	6.3 (0.4)
7-8	6.9 (0.3)	6.7 (0.6)	6.0 (0.2)	6.0 (0.2)	6.7 (0.3)	6.1 (0.2)	6.0 (0.3)
8-9	6.9 (0.3)	6.6 (0.4)	6.9 (0.2)	6.8 (0.3)	6.7 (0.3)	6.7 (0.2)	6.8 (0.3)
9-10	6.8 (0.3)	6.8 (0.3)	6.8 (0.3)	6.8 (0.3)	6.7 (0.3)	6.7 (0.3)	6.8 (0.3)
10-11	7.0 (0.3)	6.9 (0.3)	7.0 (0.3)	6.9 (0.3)	6.8 (0.3)	6.8 (0.3)	6.9 (0.3)
11-12	6.6 (0.3)	6.6 (0.3)	6.6 (0.3)	6.6 (0.3)	6.9 (0.3)	6.8 (0.3)	6.6 (0.3)
14-15	7.0 (0.3)	7.0 (0.3)	7.0 (0.3)	7.0 (0.2)	5.7 (0.3)	5.8 (0.3)	7.0 (0.3)
15-16	6.7 (0.3)	6.7 (0.3)	6.7 (0.3)	6.8 (0.3)	6.0 (0.3)	6.0 (0.4)	6.8 (0.3)
16-17	6.7 (0.3)	6.8 (0.3)	6.7 (0.3)	6.7 (0.3)	6.1 (0.4)	6.1 (0.3)	6.7 (0.3)
17-18	6.9 (0.3)	6.9 (0.3)	6.5 (0.3)	6.7 (0.3)	6.0 (0.4)	6.2 (0.3)	6.4 (0.3)
18-19	6.7 (0.3)	6.8 (0.3)	6.7 (0.4)	6.6 (0.4)	6.2 (0.3)	6.0 (0.2)	6.6 (0.3)
19-20	6.9 (0.3)	6.8 (0.3)	6.9 (0.3)	6.8 (0.4)	6.0 (0.4)	5.7 (0.3)	6.8 (0.4)
20-21	6.8 (0.3)	6.7 (0.3)	6.9 (0.3)	6.7 (0.3)	6.2 (0.3)	6.0 (0.3)	6.7 (0.3)
21-22	6.7 (0.3)	6.8 (0.3)	6.7 (0.3)	6.8 (0.3)	5.9 (0.3)	5.9 (0.3)	6.7 (0.3)
22-23	6.8 (0.3)	6.9 (0.3)	6.8 (0.3)	6.9 (0.3)	6.0 (0.3)	6.0 (0.3)	6.8 (0.3)
23-24	6.9 (0.3)	NA	6.9 (0.3)	NA	7.0 (0.3)	6.8 (0.5)	6.9 (0.3)

Table S11. P′ to P′ distance, in angstroms, for TBA15 systems (std. dev in paratheses).

Base pair	TBA15 Canonical	TBA15	TBA15 A_L	TBA15 T_L
2-3	6.9 (0.3)	6.9 (0.3)	6.9 (0.3)	6.9 (0.3)
3-4	6.7 (0.3)	6.7 (0.3)	6.7 (0.3)	6.7 (0.3)
4-5	6.7 (0.3)	6.7 (0.3)	6.7 (0.3)	6.8 (0.3)
5-6	6.8 (0.3)	6.8 (0.2)	6.8 (0.2)	6.8 (0.2)
6-7	6.6 (0.3)	6.7 (0.3)	6.8 (0.3)	6.6 (0.3)
7-8	6.7 (0.3)	6.1 (0.4)	6.0 (0.4)	5.7 (0.6)
8-9	6.8 (0.3)	6.0 (0.3)	6.0 (0.2)	5.7 (0.4)

9-10	6.7 (0.3)	6.5 (0.4)	6.6 (0.3)	5.7 (0.3)
10-11	6.8 (0.3)	6.9 (0.3)	6.9 (0.3)	6.8 (0.3)
11-12	6.7 (0.3)	6.7 (0.3)	6.7 (0.3)	6.7 (0.3)
12-13	6.7 (0.3)	6.7 (0.3)	6.7 (0.3)	6.7 (0.3)
13-14	6.8 (0.3)	6.8 (0.3)	6.7 (0.3)	6.8 (0.3)
14-15	6.9 (0.2)	6.9 (0.2)	6.9 (0.2)	6.9 (0.2)
17-18	5.8 (0.3)	5.8 (0.3)	5.8 (0.3)	5.8 (0.3)
18-19	6.0 (0.3)	6.0 (0.3)	5.9 (0.4)	5.9 (0.4)
19-20	6.1 (0.3)	6.1 (0.3)	6.1 (0.3)	6.1 (0.3)
20-21	6.1 (0.3)	6.2 (0.3)	6.2 (0.3)	6.1 (0.3)
21-22	6.0 (0.3)	5.8 (0.3)	6.0 (0.3)	5.8 (0.3)
22-23	5.9 (0.3)	5.7 (0.6)	6.3 (0.6)	5.6 (0.3)
23-24	6.2 (0.3)	6.6 (0.3)	6.4 (0.3)	6.6 (0.3)
24-25	5.9 (0.4)	5.9 (0.4)	6.4 (0.3)	5.9 (0.3)
25-26	6.2 (0.3)	6.0 (0.3)	5.9 (0.4)	5.7 (0.3)
26-27	6.0 (0.3)	6.0 (0.3)	6.0 (0.3)	5.9 (0.3)
27-28	6.0 (0.3)	6.0 (0.3)	6.0 (0.4)	6.0 (0.3)
28-29	6.0 (0.3)	6.0 (0.3)	6.0 (0.3)	6.0 (0.3)
29-30	5.8 (0.3)	5.9 (0.3)	5.8 (0.3)	5.9 (0.4)

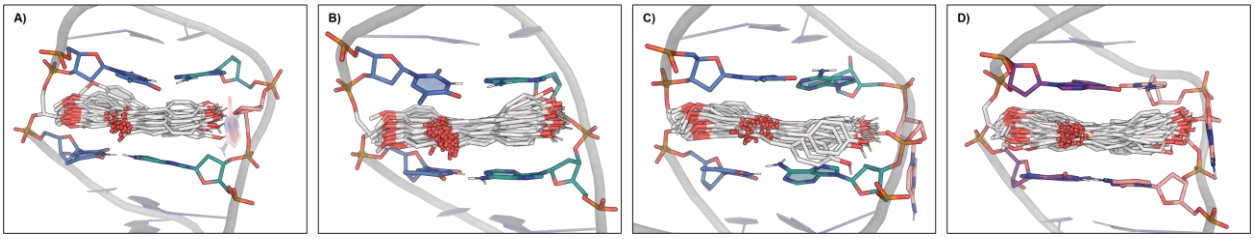

Figure S64. 100 Frame overlay (top) for A) PhOH6HI (grey) at *G7* opposite dC18 (pink), B) PhOH6HI (grey) at *G7* opposite N-1, C) PhOH6HI (grey) at G7 opposite 2'-OMe C18 (pink), and D) PhOH6HI (grey) at *G7* flanked by dG6 and dG8.

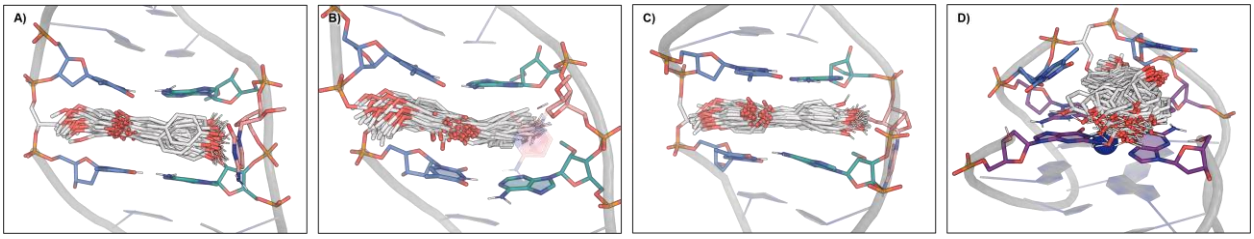

Figure S65. 100 Frame overlay for A) PhOH6HI (grey) at *G8*, B) PhOH6HI (grey) at *G8* flanked by T_L, C) PhOH6HI (grey) at *G8* interstrand flanked by A_L and D) PhOH6HI (grey) at *G8* TBA15 GQ with K^+

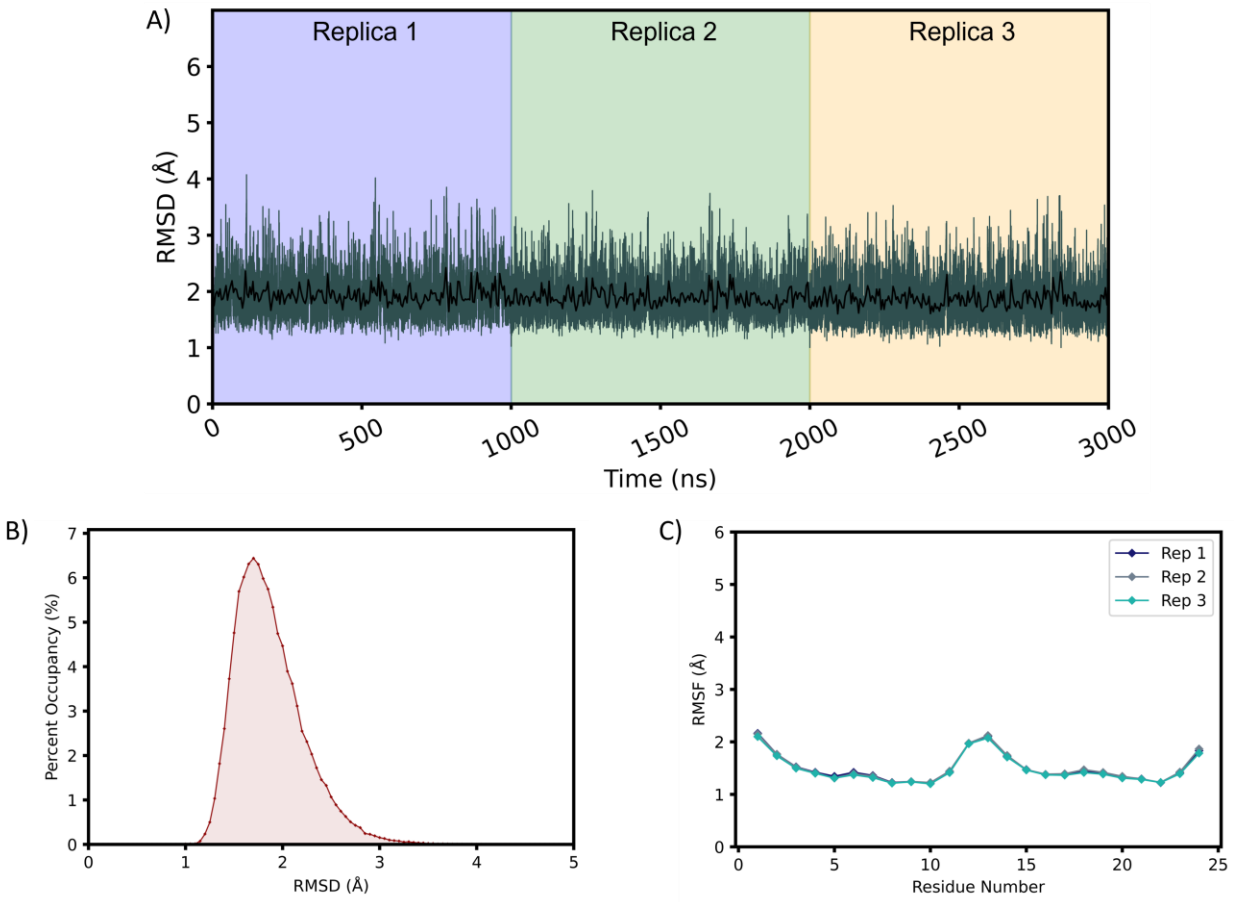

Figure S66. Data for the unmodified *Narl*12 DG opposite dC. A) All heavy atom RMSDs across the three MD production simulation replicas, B) histogram of RMSD distribution across all replicates, and C) RMSF.

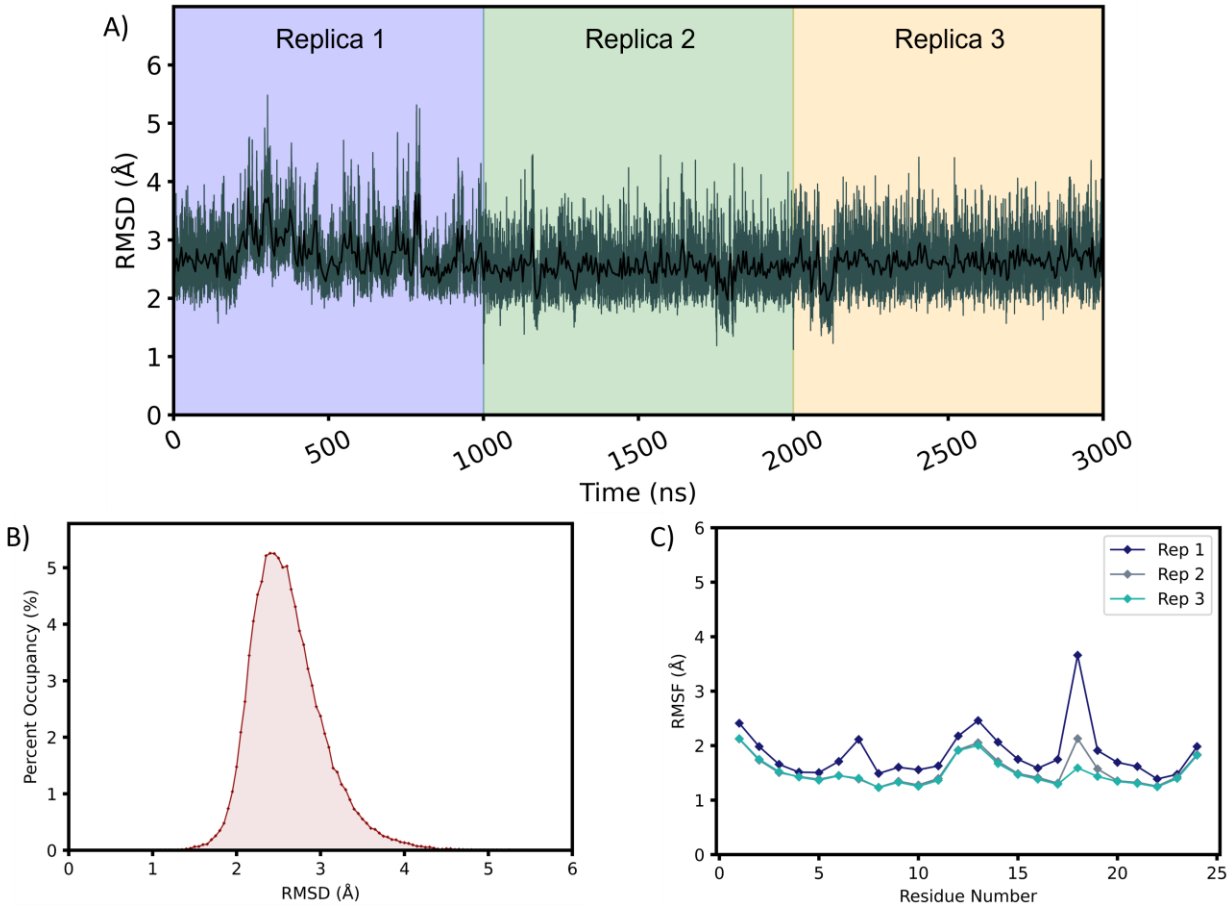

Figure S67. Data for the *Narl*12 PhOH6HI opposite dC. A) All heavy atom RMSDs across the three MD production simulation replicas, B) histogram of RMSD distribution across all replicates, and C) RMSF.

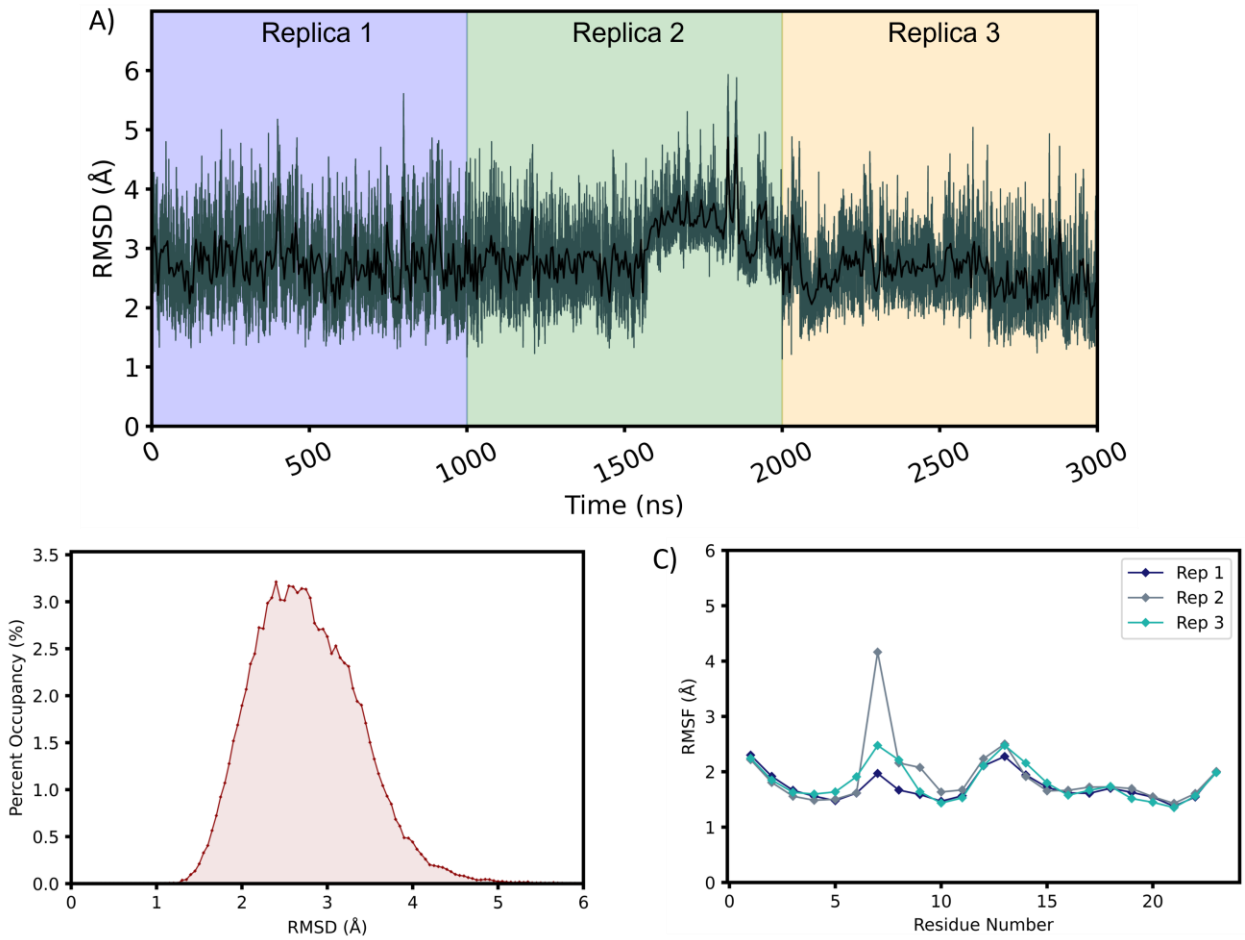

Figure S68. Data for the unmodified *Narl*12 dG truncated. A) All heavy atom RMSDs across the three MD production simulation replicas, B) histogram of RMSD distribution across all replicates, and C) RMSF.

In the second replica, dG7 momentarily lost stacking and shuffled into the minor groove before returning back to stacking with the flanking nucleotides.

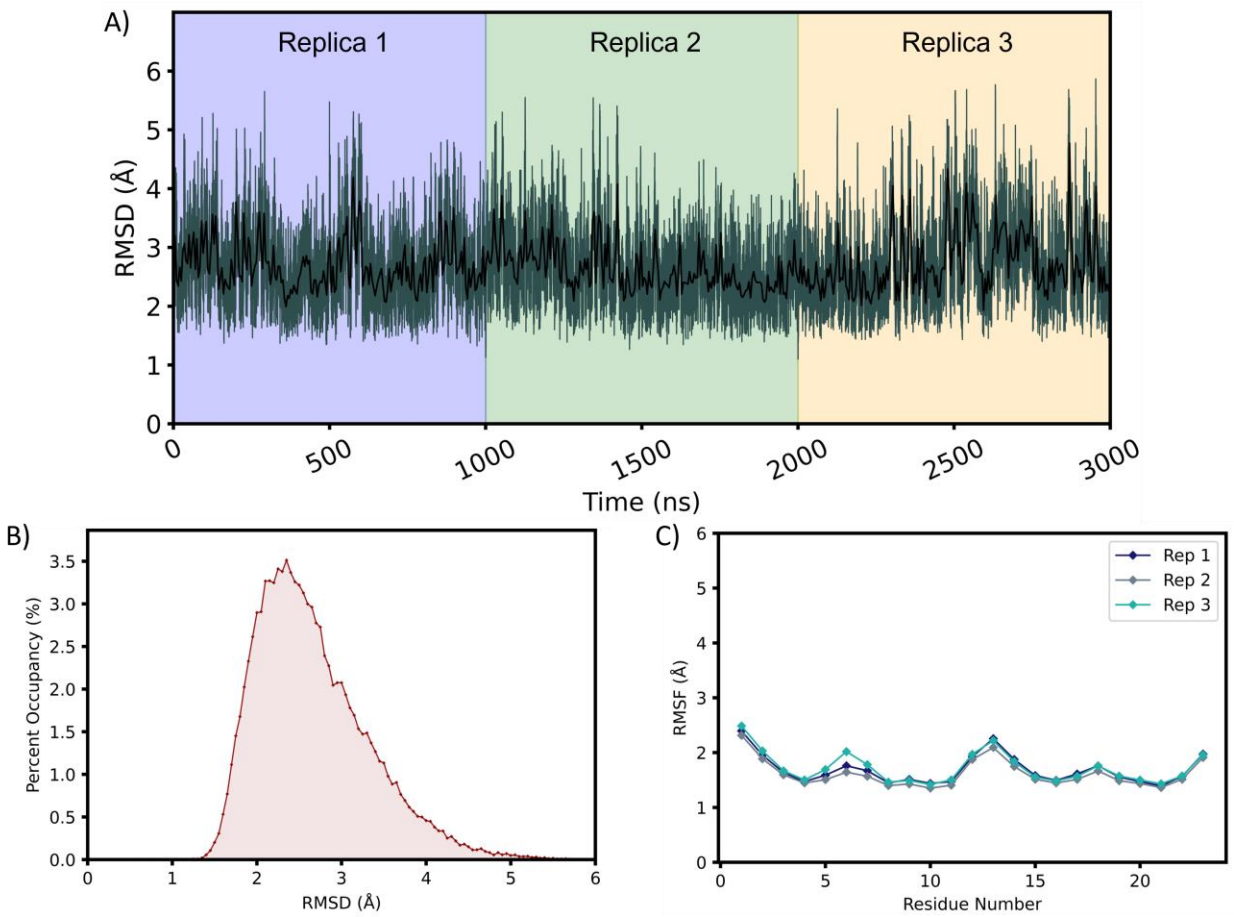

Figure S69. Data for the *Narl*12 PhOH6HI N-1. A) All heavy atom RMSDs across the three MD production simulation replicas, B) histogram of RMSD distribution across all replicates, and C) RMSF.

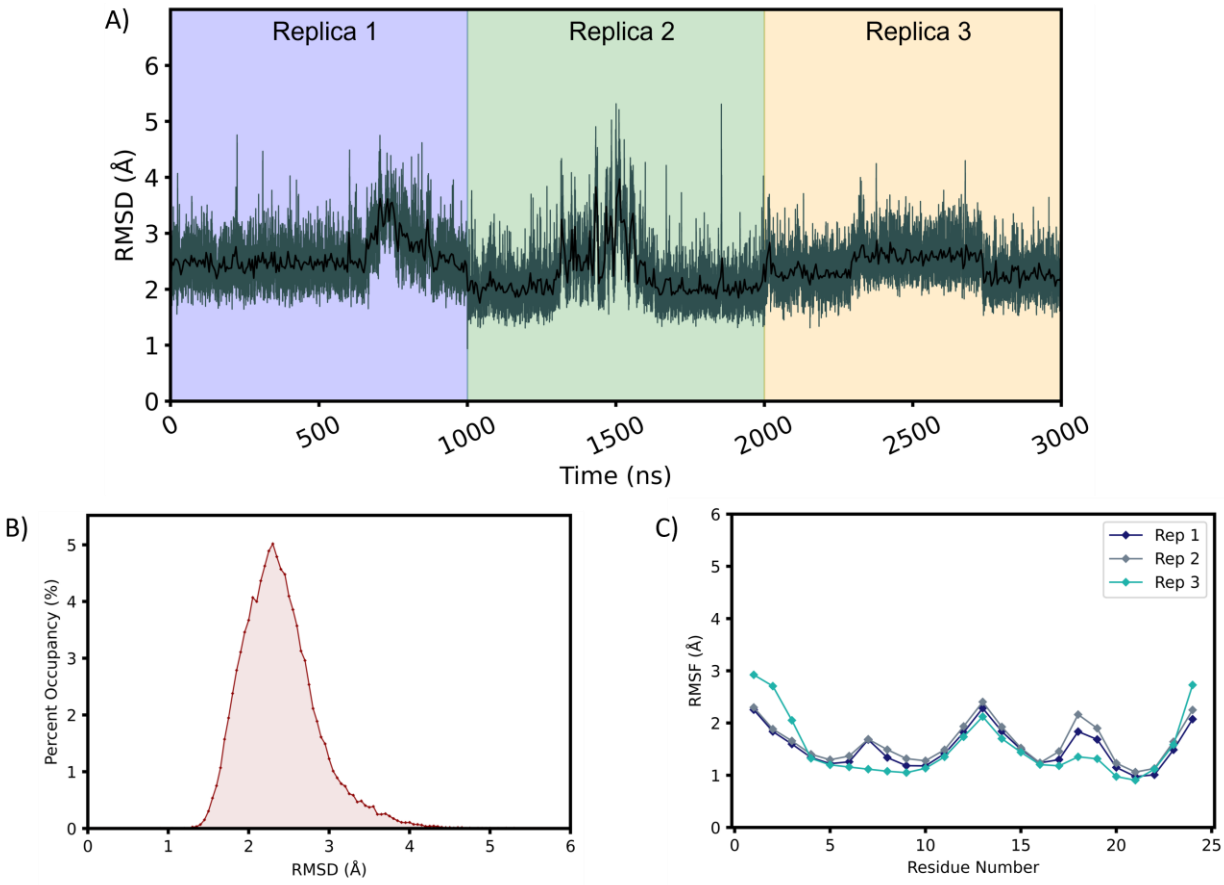

Figure S70. Data for the unmodified *Narl*12 DG across 2'-OMe C. A) All heavy atom RMSDs across the three MD production simulation replicas, B) histogram of RMSD distribution across all replicates, and C) RMSF.

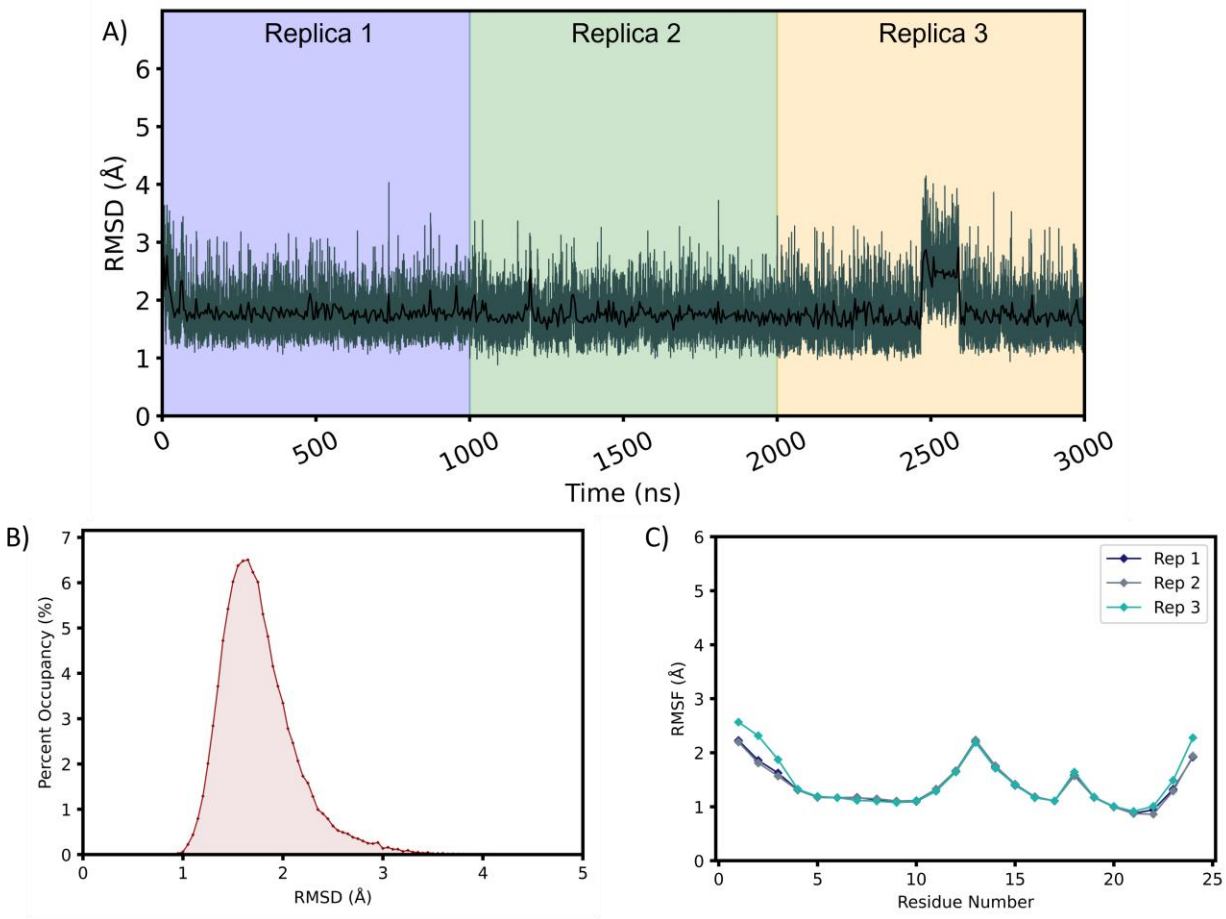

Figure S71. Data for the *Narl*12 PhOH6HI across 2'-OMe C. A) All heavy atom RMSDs across the three MD production simulation replicas, B) histogram of RMSD distribution across all replicates, and C) RMSF.

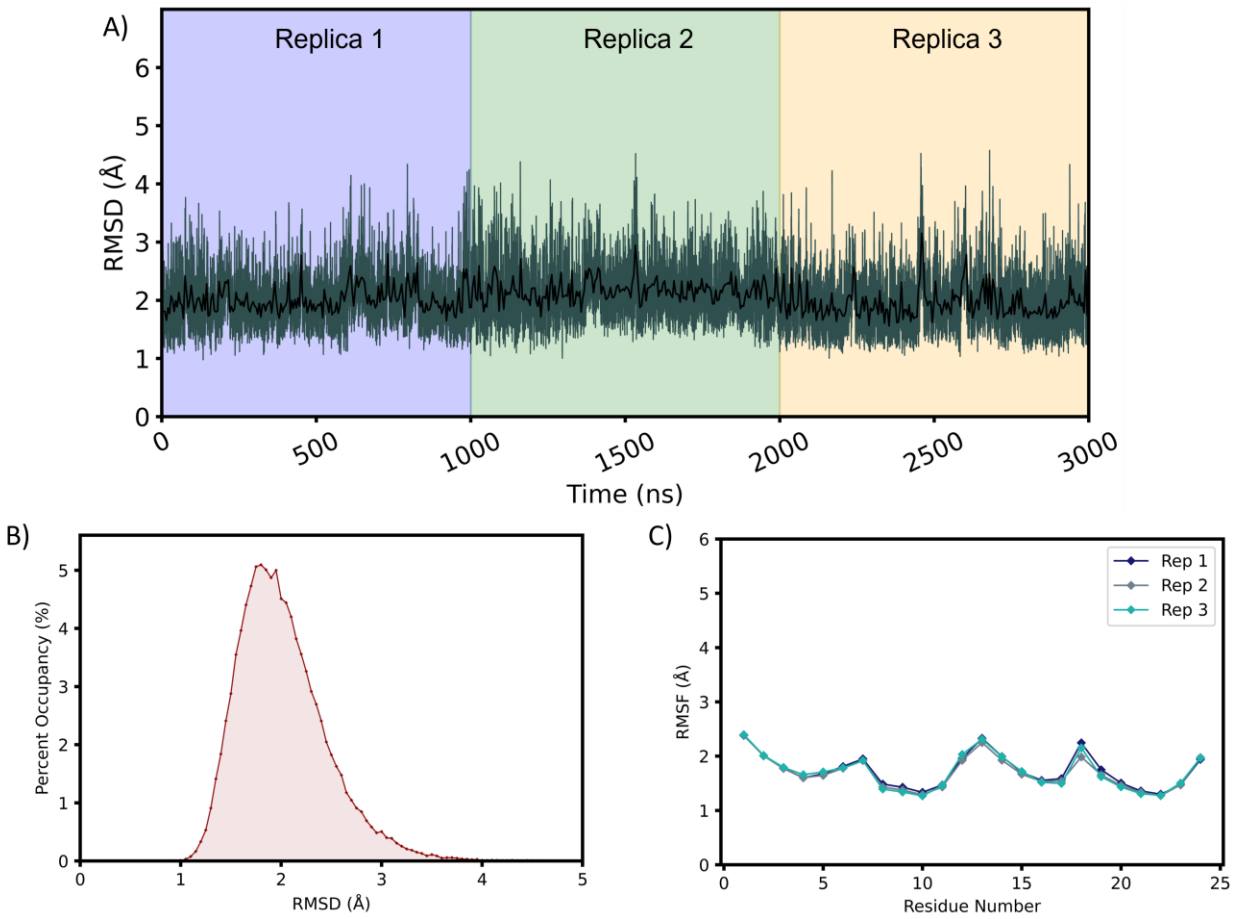

Figure S72. Data for the *Narl*12 PhOH6HI flanked by dG6 and dG8. A) All heavy atom RMSDs across the three MD production simulation replicas, B) histogram of RMSD distribution across all replicates, and C) RMSF.

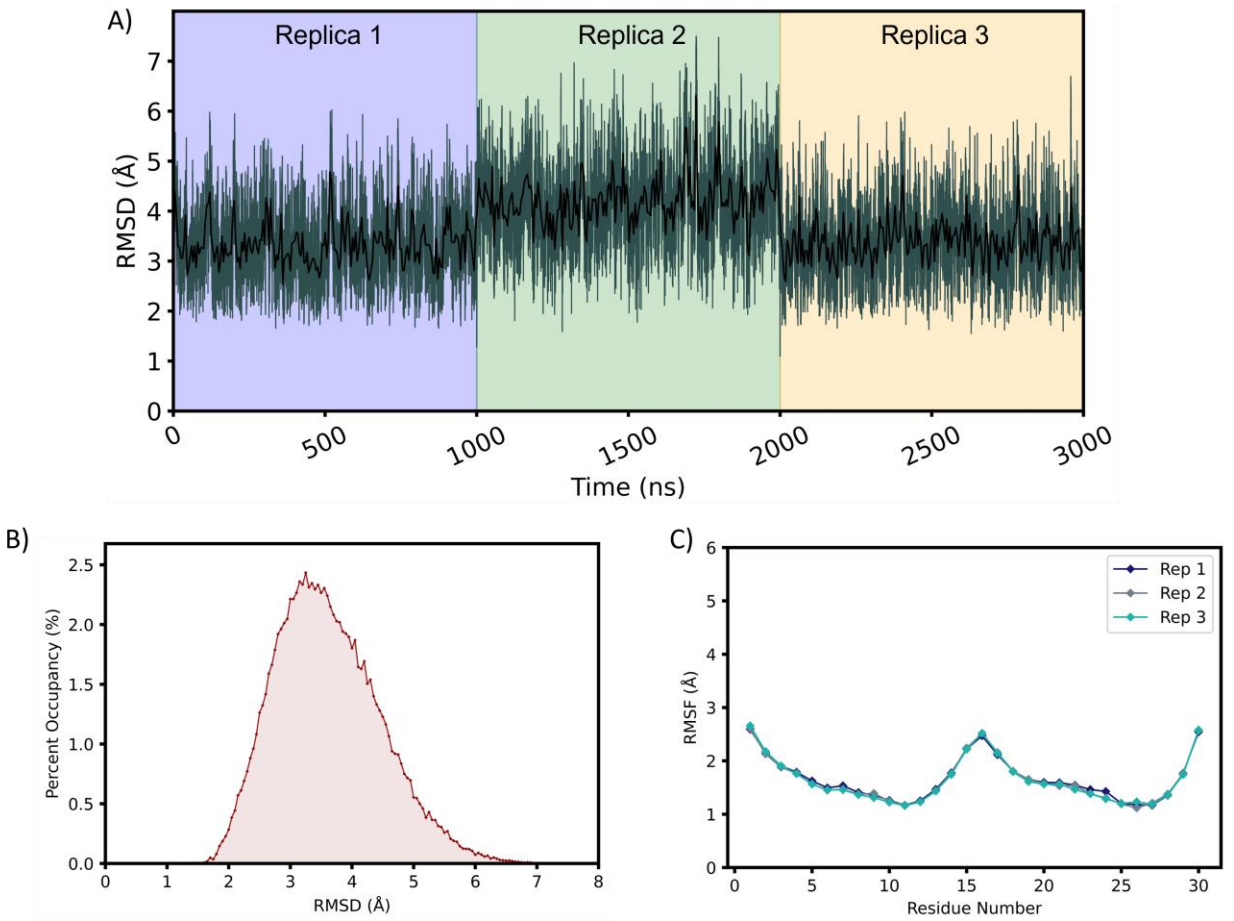

Figure S73. Data for the unmodified TBA15 DG across 2'-OMe C. A) All heavy atom RMSDs across the three MD production simulation replicas, B) histogram of RMSD distribution across all replicates, and C) RMSF.

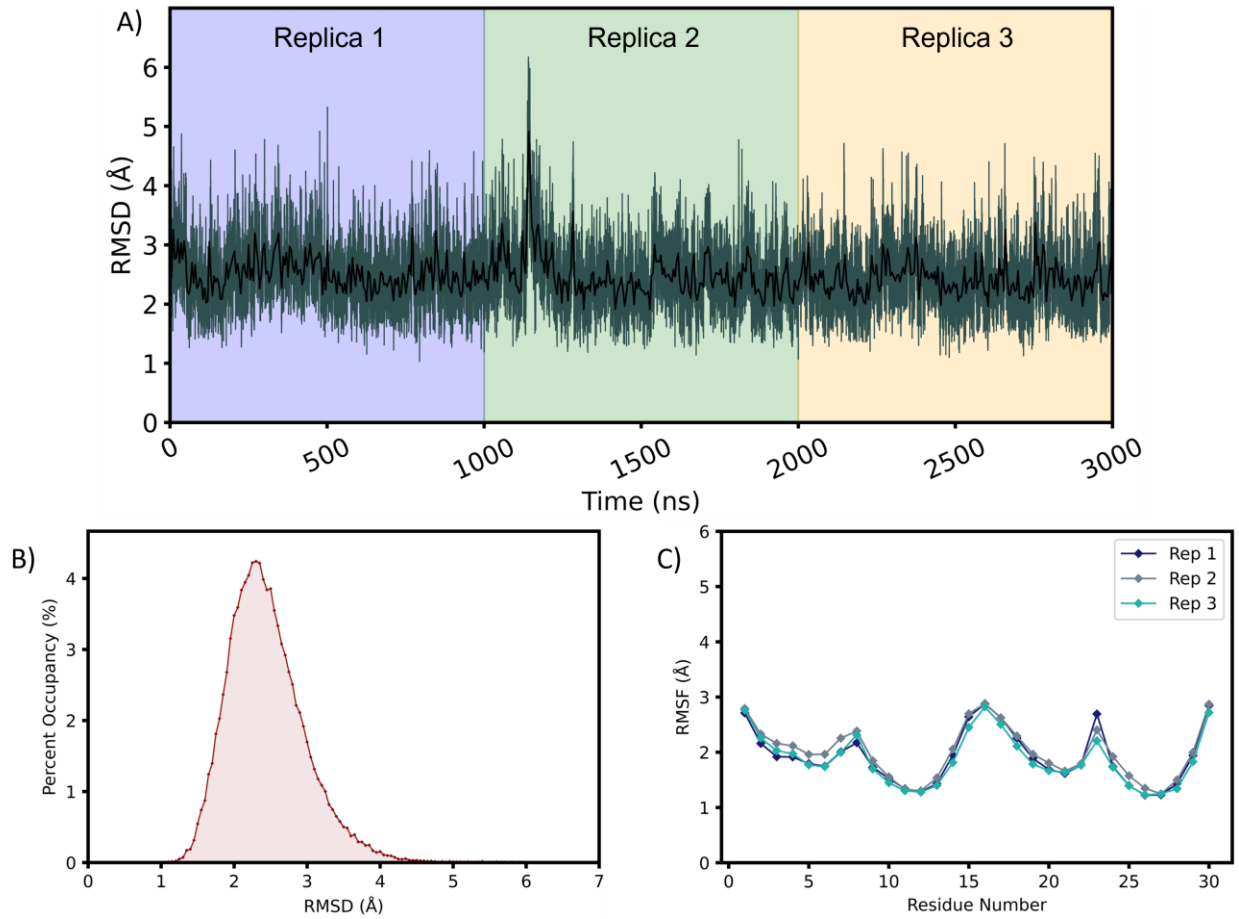

Figure S74. Data for the TBA15 PhOH6HI across 2'-OMe C. A) All heavy atom RMSDs across the three MD production simulation replicas, B) histogram of RMSD distribution across all replicates, and C) RMSF.

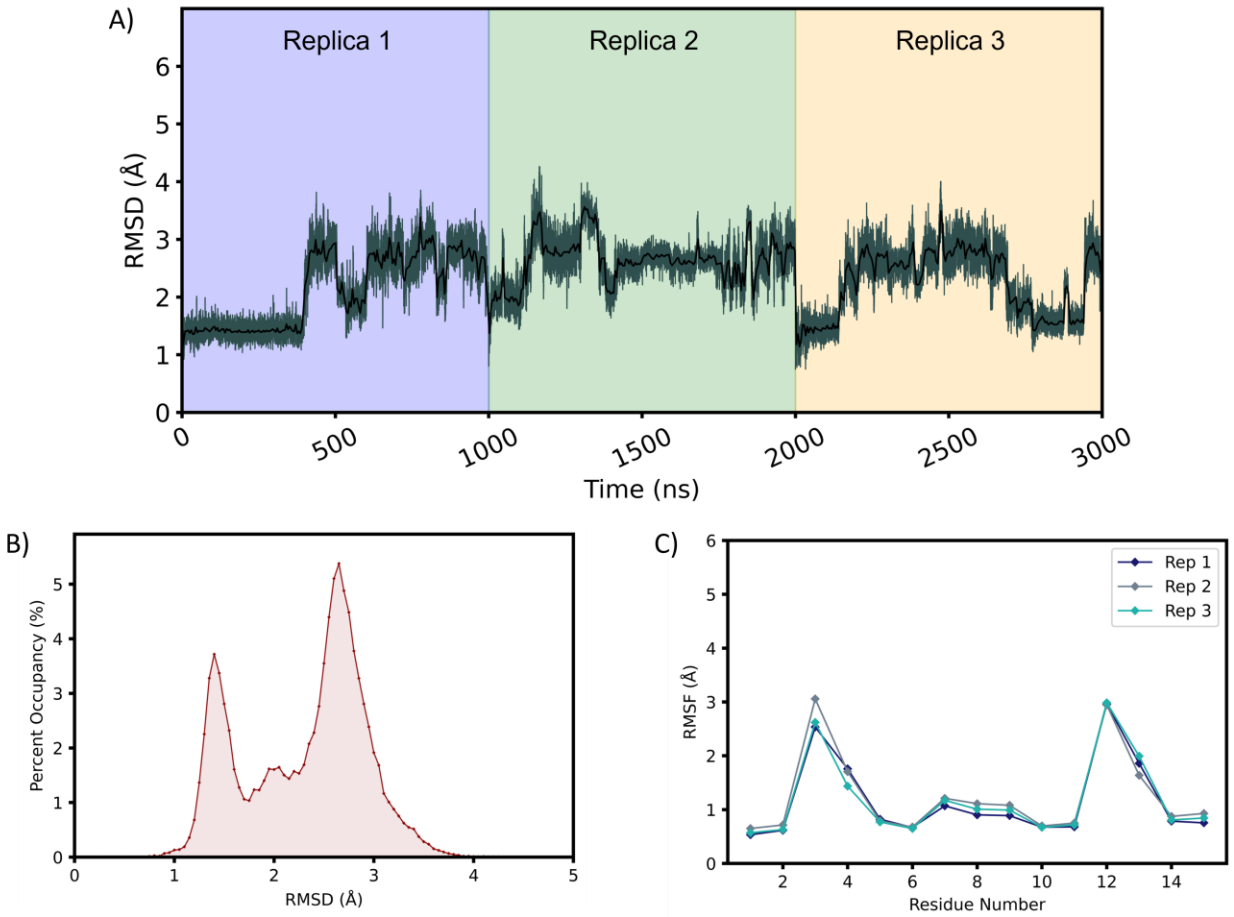

Figure S75. Data for the TBA15 GQ with K^+. A) All heavy atom RMSDs across the three MD production simulation replicas, B) histogram of RMSD distribution across all replicates, and C) RMSF.

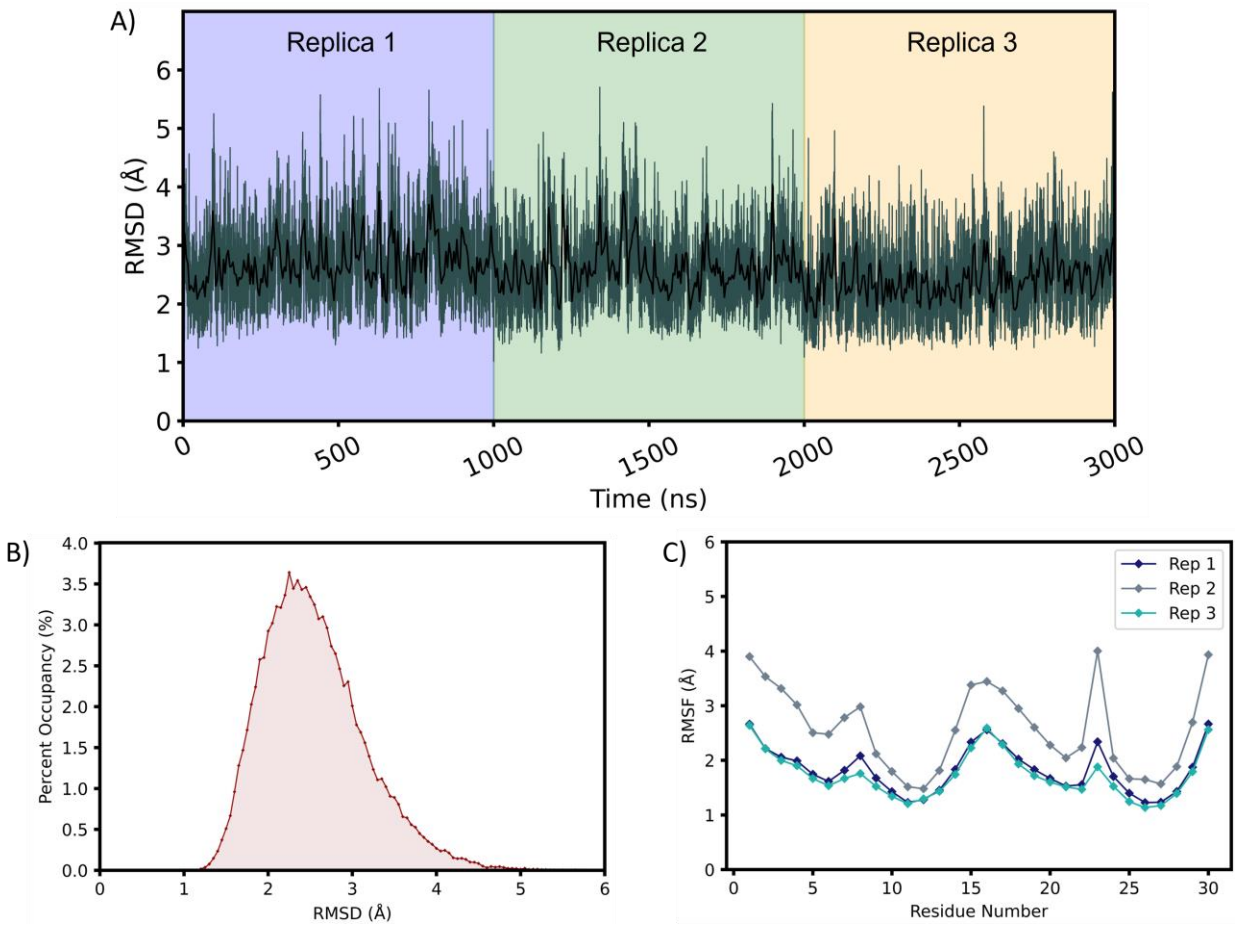

Figure S76. Data for the TBA15 PhOH6HI flanked by T_L opposite 2'-OMe C. A) All heavy atom RMSDs across the three MD production simulation replicas, B) histogram of RMSD distribution across all replicates, and C) RMSF.

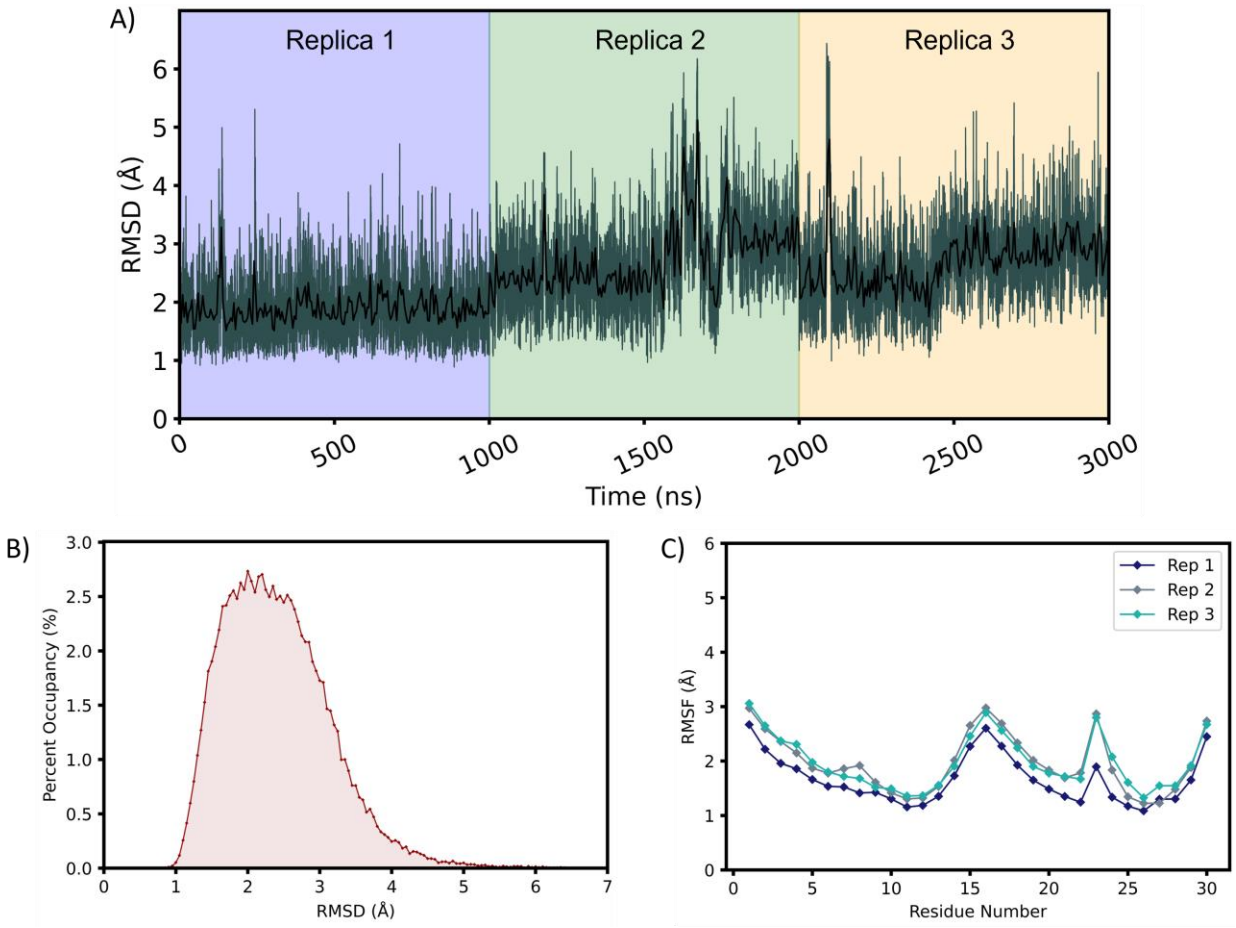

Figure S77. Data for the TBA15 PhOH6HI opposite 2'-OMe C interstrand flanked by A_L. A) All heavy atom RMSDs across the three MD production simulation replicas, B) histogram of RMSD distribution across all replicates, and C) RMSF.

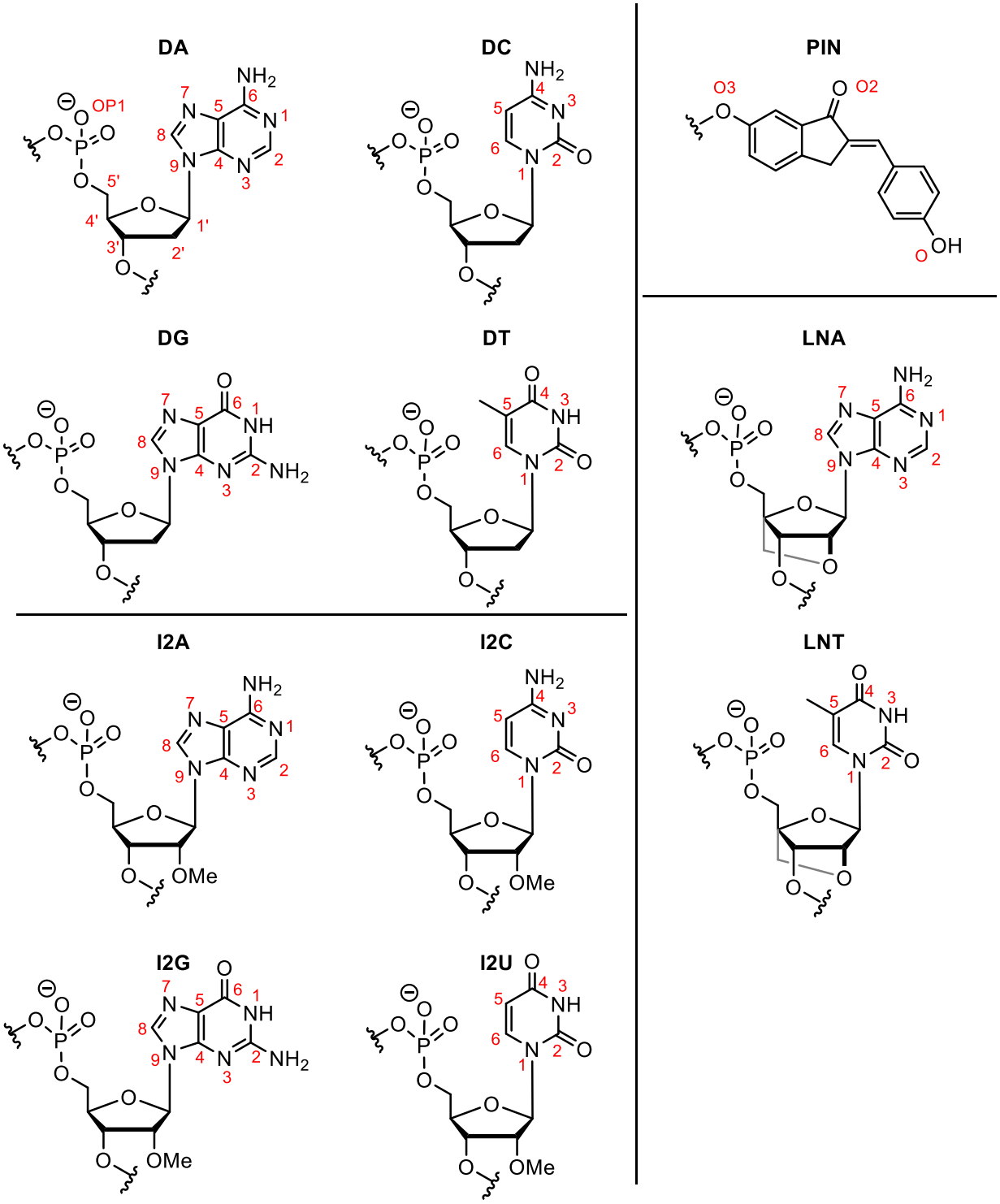

Figure S78. Naming conventions of the nucleic acids and probes, as well as the numbering used for hydrogen-bond analysis in this study.

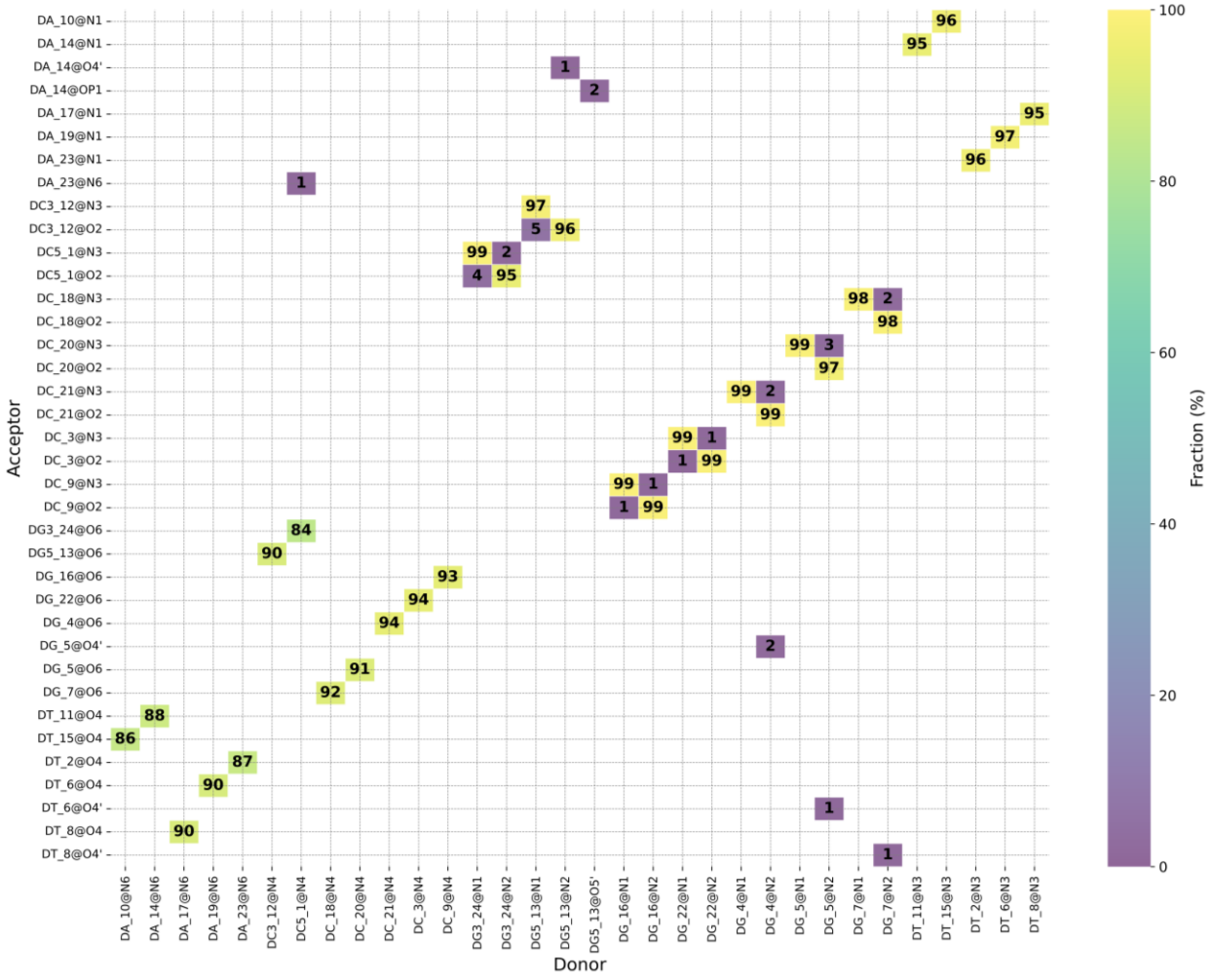

Figure S79. Occupancies of hydrogen bonds for the unmodified *Narl*12 dG opposite dC reported as the average of the three replicates.

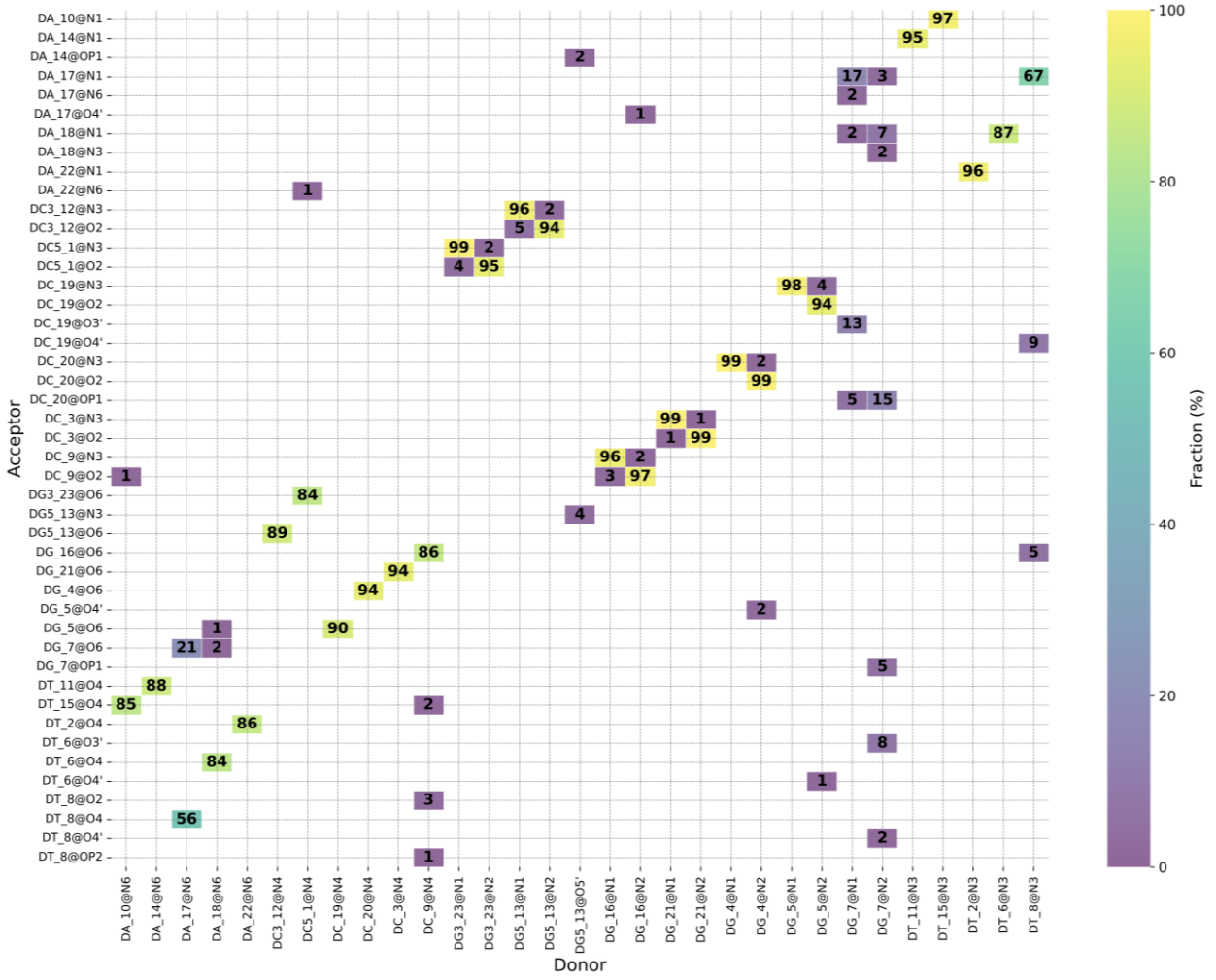

Figure S80. Occupancies of hydrogen bonds for the unmodified *Narl*12 dG N-1 reported as the average of the three replicates.

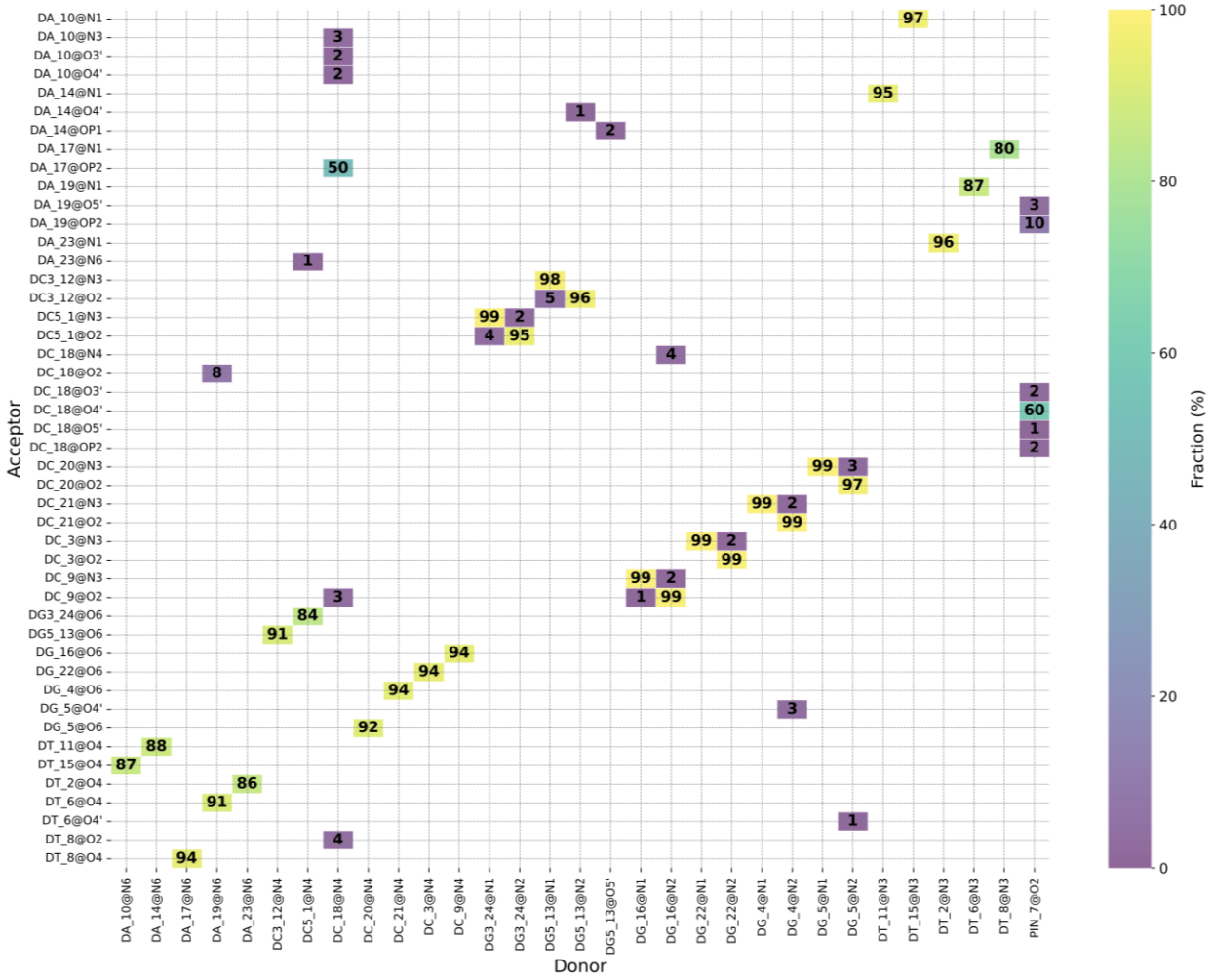

Figure S81. Occupancies of hydrogen bonds for the *Narl*12 PhOH6HI opposite dC reported are as average of the three replicates.

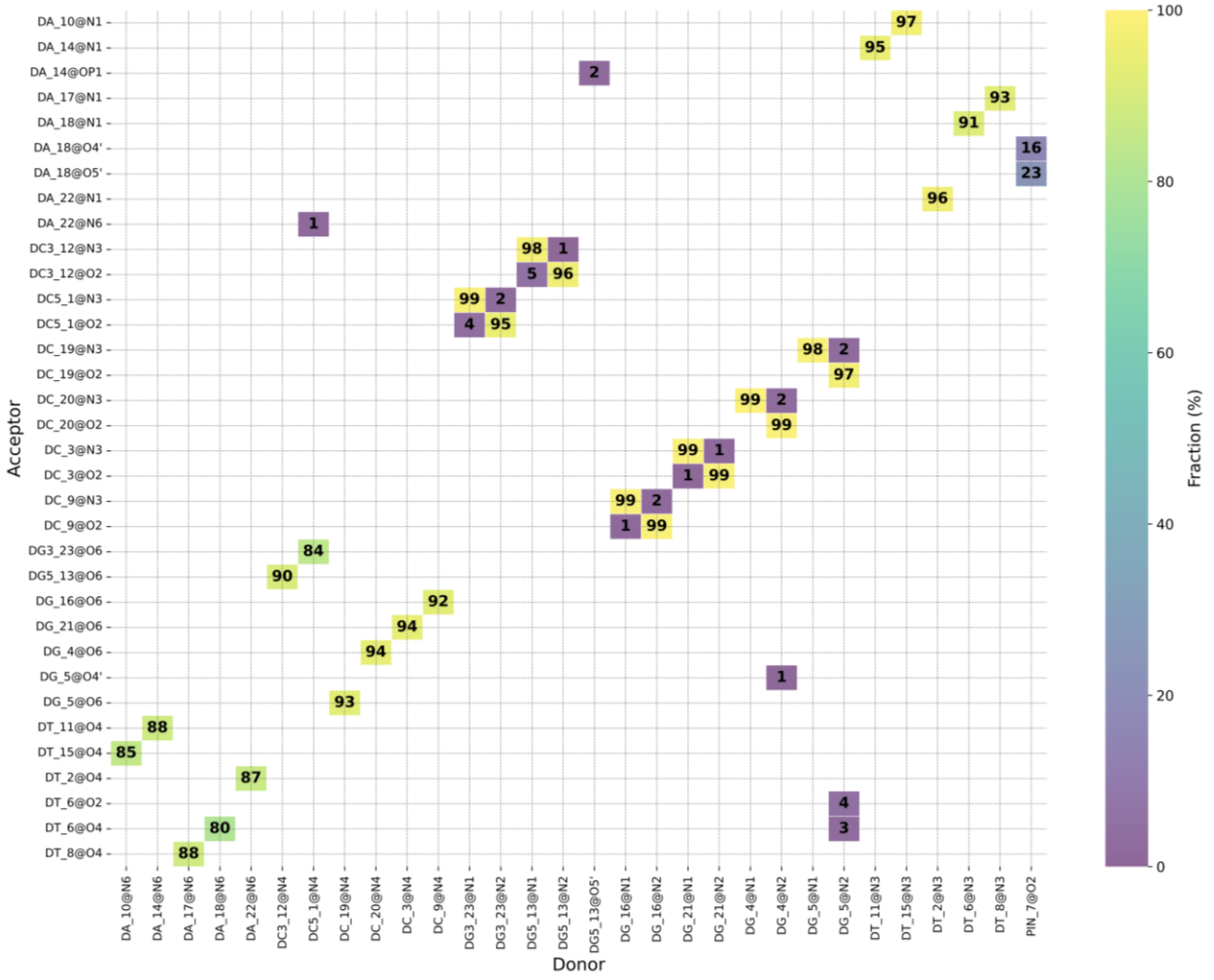

Figure S82. Occupancies of hydrogen bonds for the *Narl*12 PhOH6HI N-1 reported as the average of the three replicates.

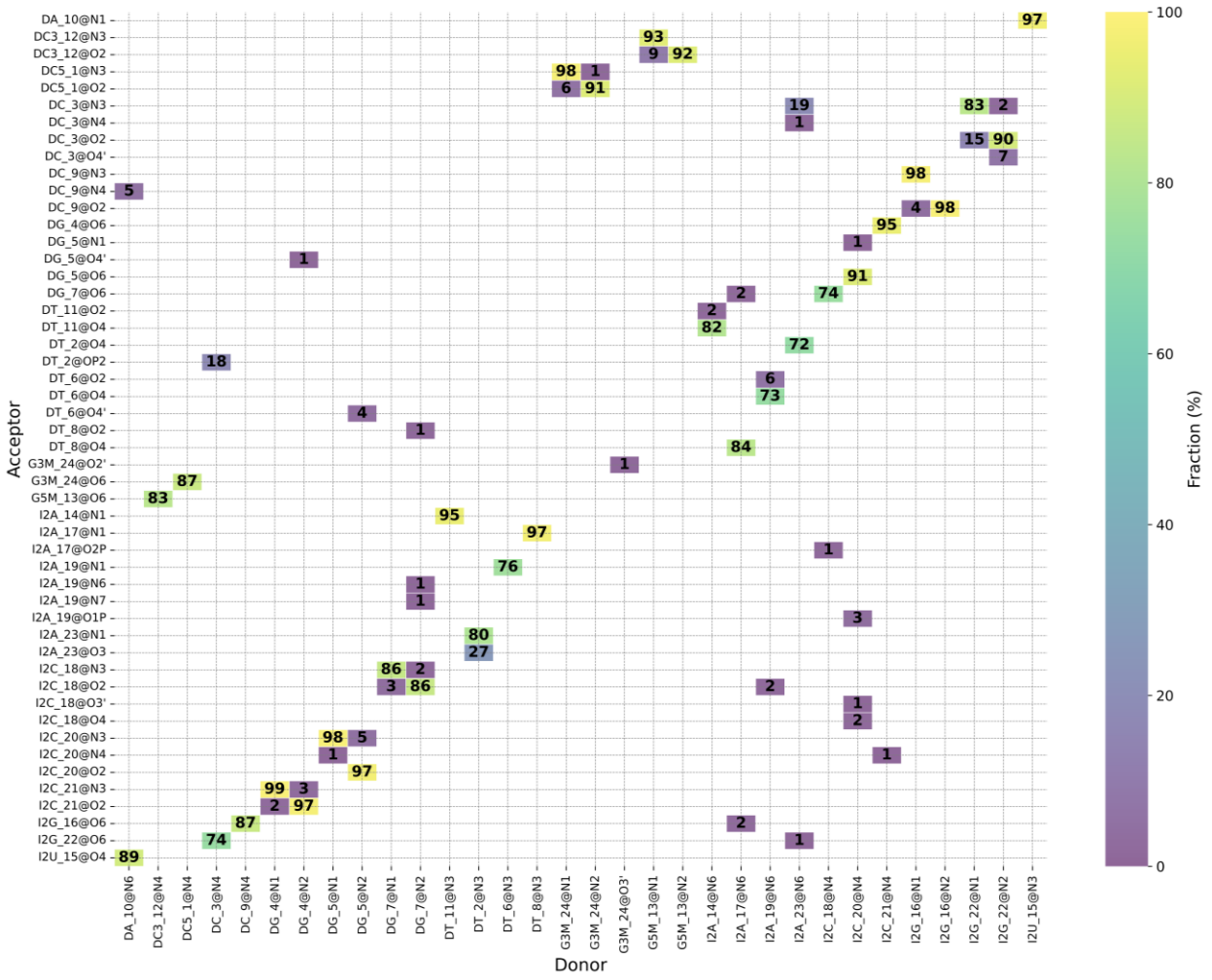

Figure S83. Occupancies of hydrogen bonds for the *Narl*12 dG opposite C reported as the average of the three replicates.

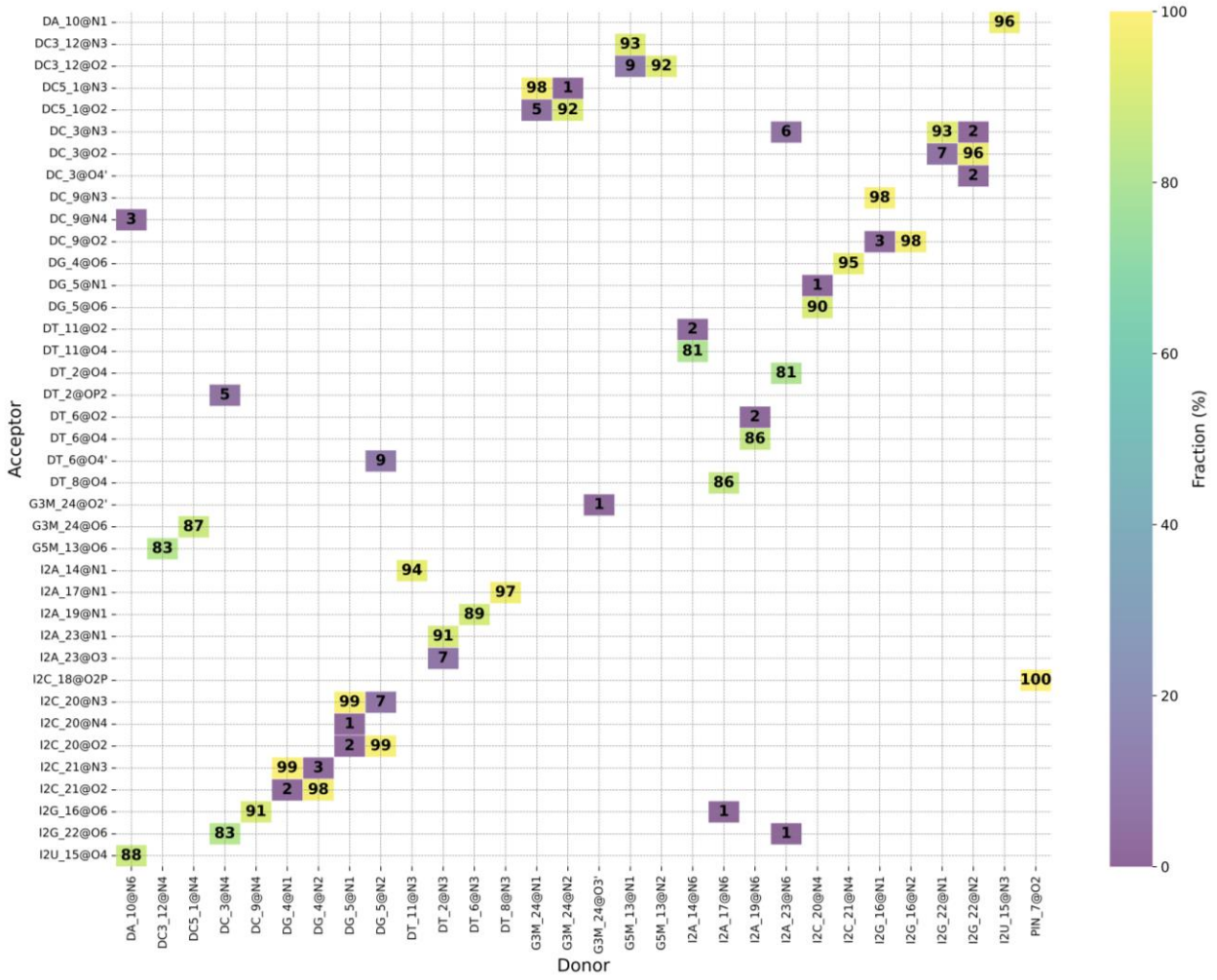

Figure S84. Occupancies of hydrogen bonds for the *Narl*12 PhOH6HI opposite C reported as the average of the three replicates.

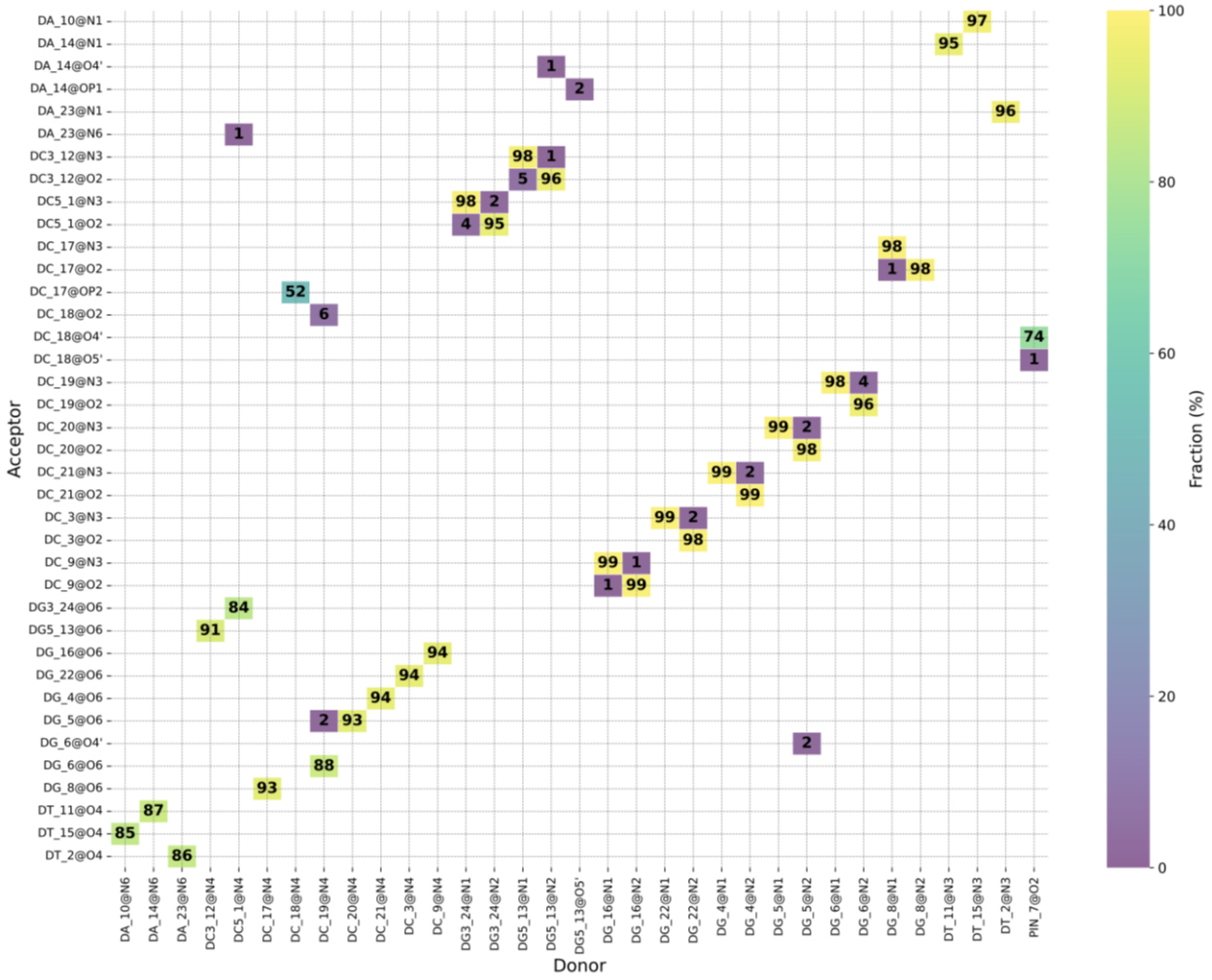

Figure S85. Occupancies of hydrogen bonds for the *Narl*12 PhOH6HI flanked by dG6 and dG8 reported as the average of the three replicates.

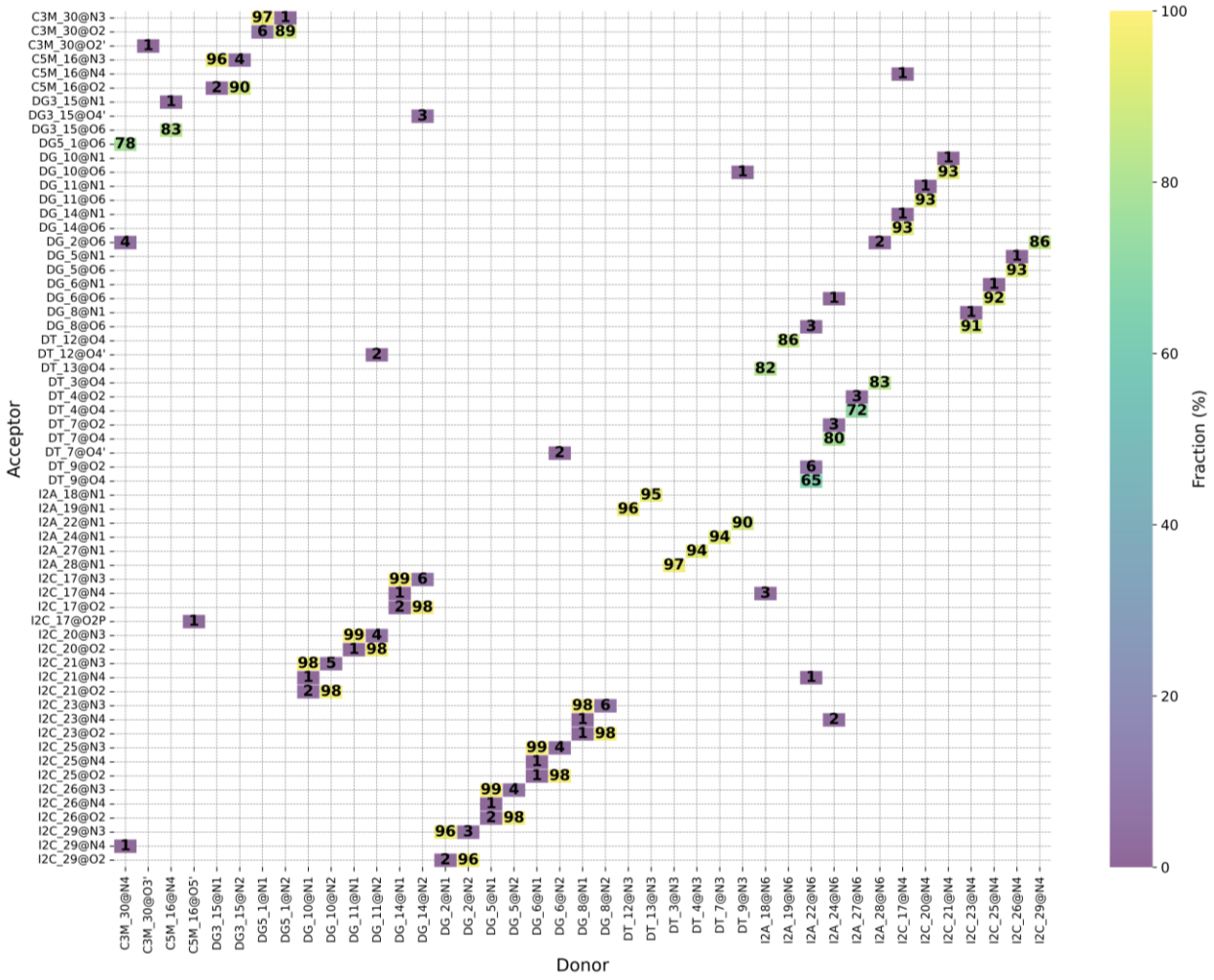

Figure S86. Occupancies of hydrogen bonds for the unmodified TBA15 dG opposite C reported as the average of the three replicates.

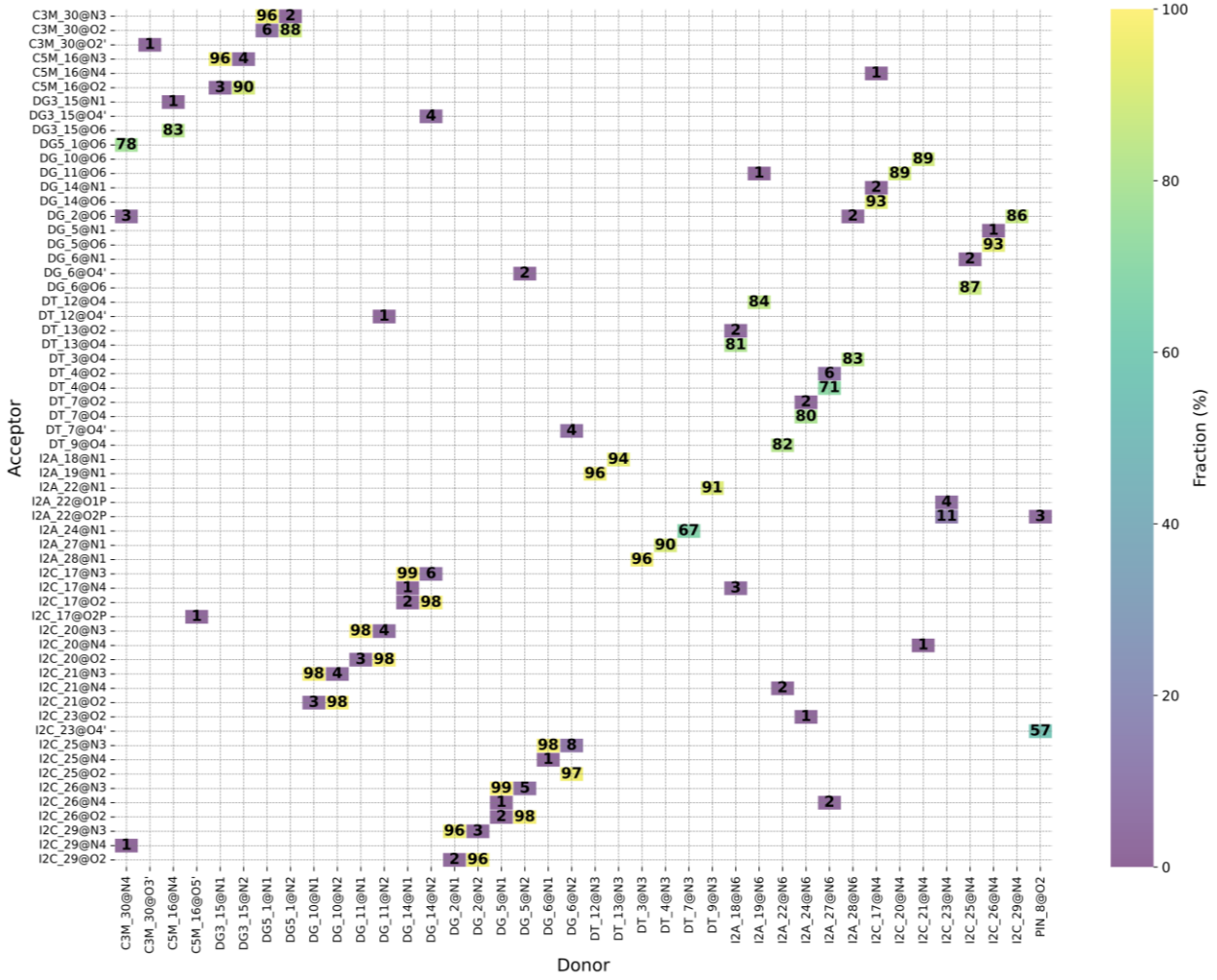

Figure S87. Occupancies of hydrogen bonds for the TBA15 PhOH6HI opposite C reported as the average of the three replicates.

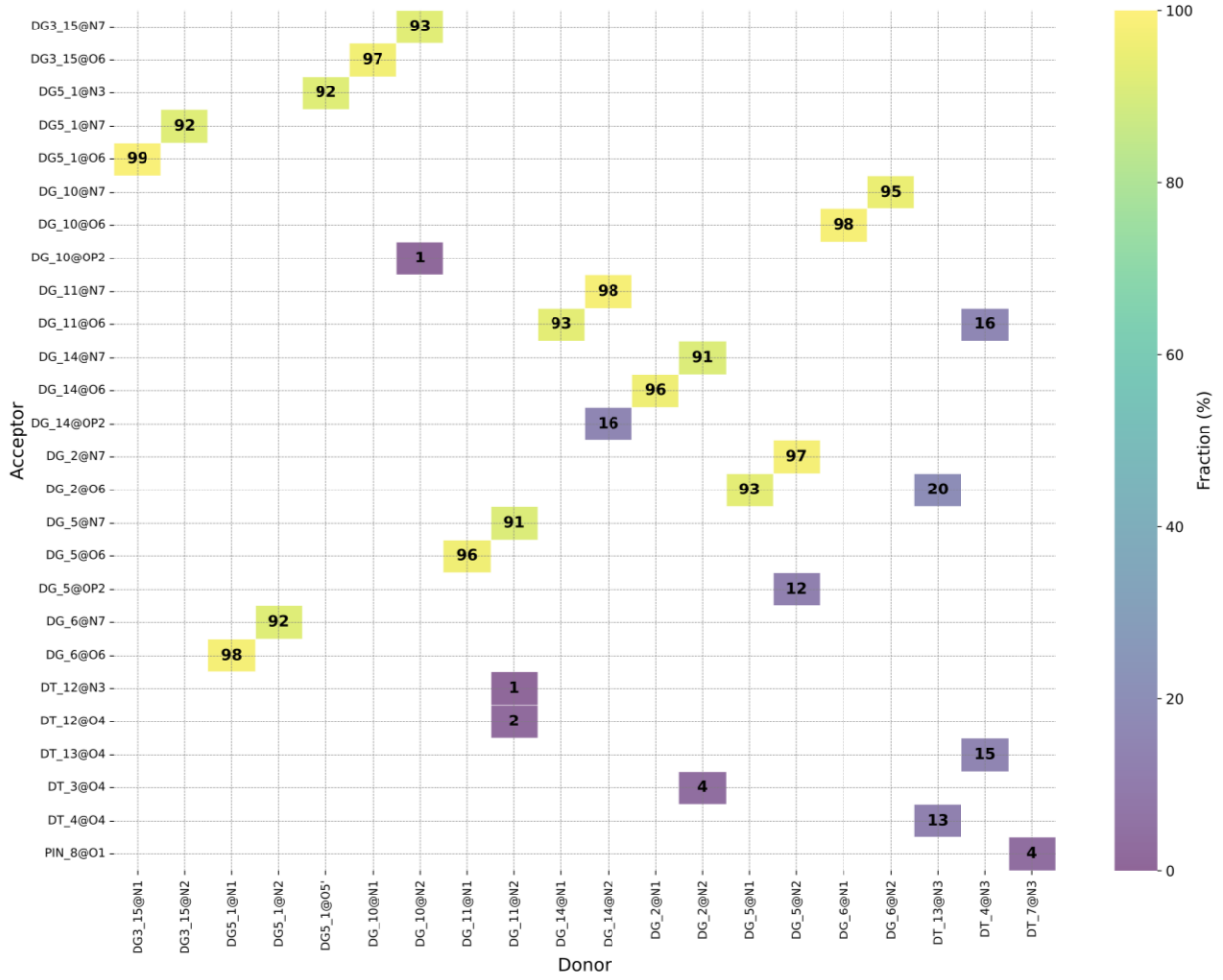

Figure S88. Occupancies of hydrogen bonds for the TBA15 GQ with K^+ reported as the average of the three replicates.

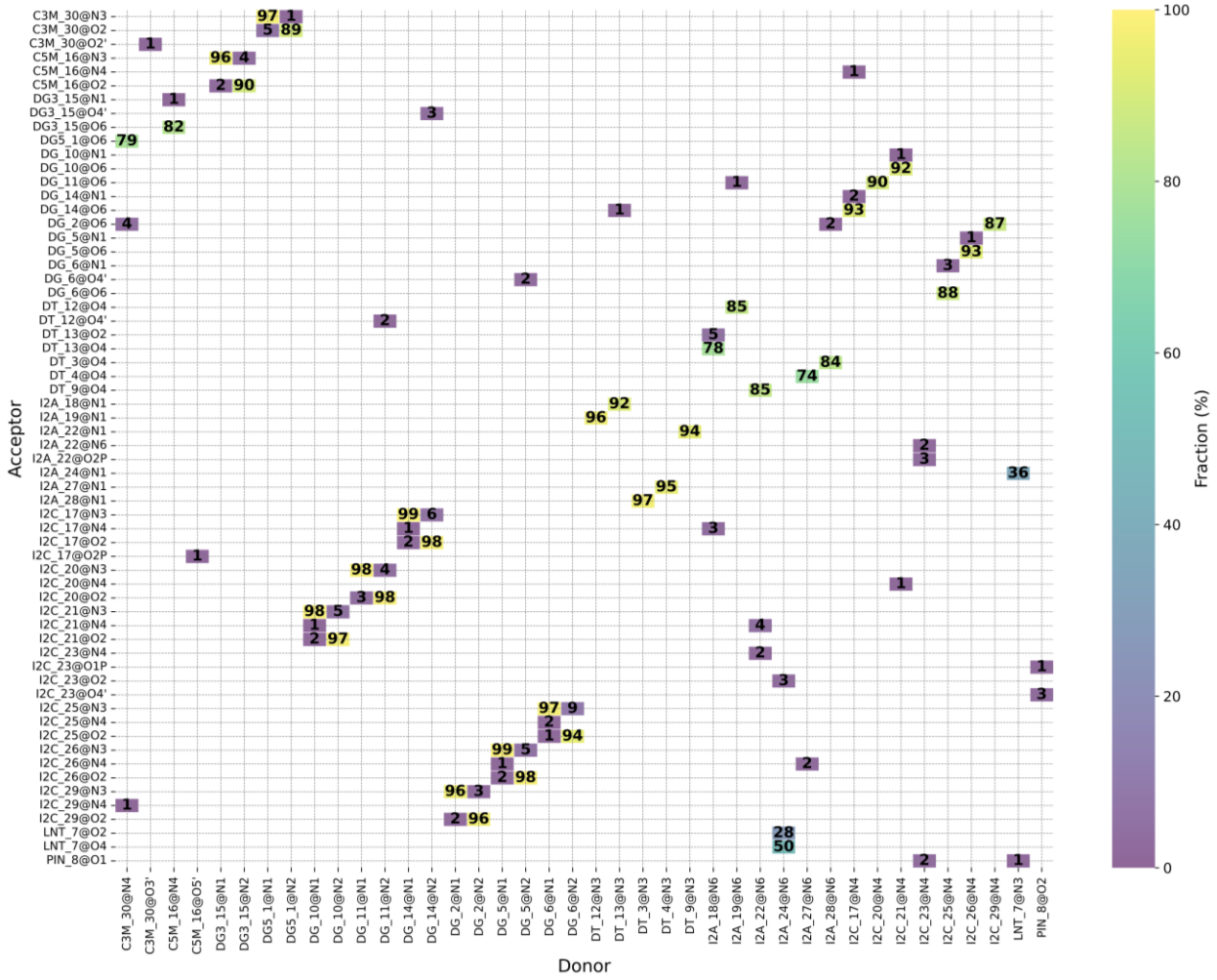

Figure S89. Occupancies of hydrogen bonds for the TBA15 PhOH6HI flanked by T_L opposite C reported as the average of the three replicates.

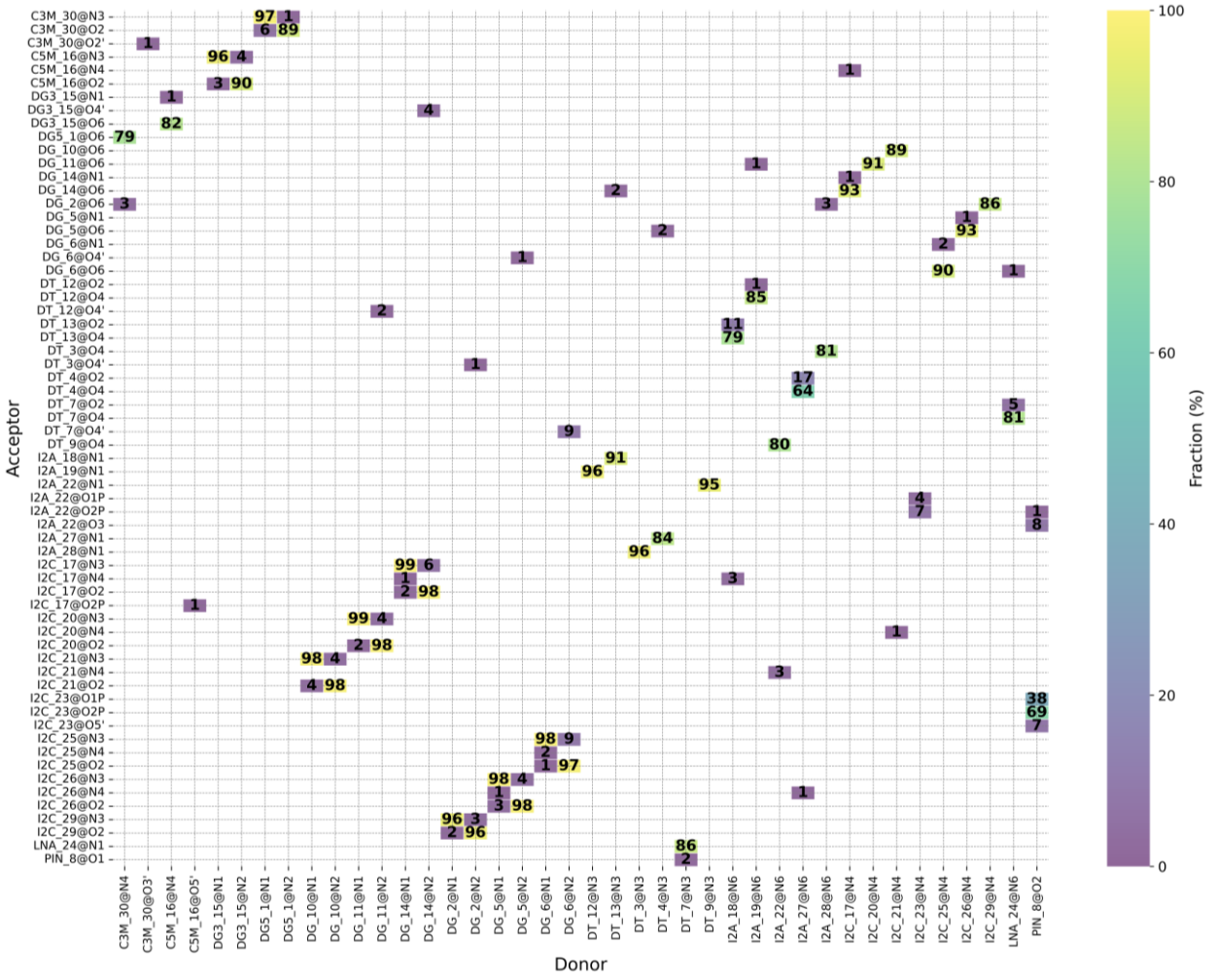

Figure S90. Occupancies of hydrogen bonds for the TBA15 PhOH6HI opposite C interstrand flanked by A_L reported as the average of the three replicates.

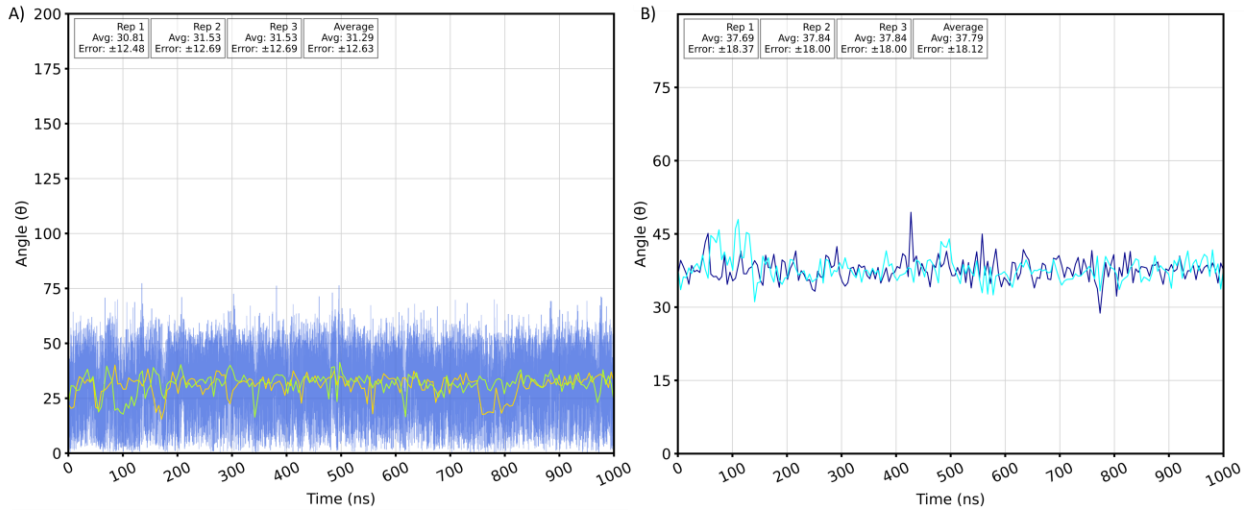

Figure S91. Data for the *Narl*12 PhOH6HI opposite dC. A) The co-planar angle between the indanone and phenol moiety, with the 5 ns running average plotted on top of the raw data (blue). B) The dihedral angle of the rotatable σ-bond bridging the two aryl moieties of the PhOH6HI. The running average of every 5 ns is plotted.

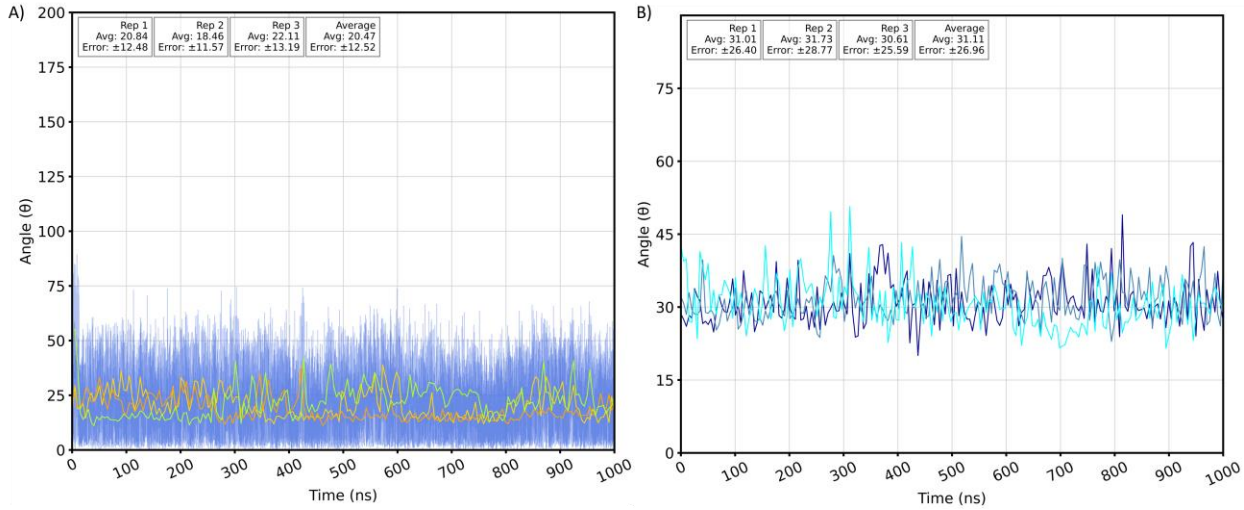

Figure S92. Data for the *Narl*12 PhOH6HI N-1. A) The co-planar angle between the indanone and phenol moiety, with the 5 ns running average plotted on top of the raw data (blue). B) The dihedral angle of the rotatable σ-bond bridging the two aryl moieties of the PhOH6HI. The running average of every 5 ns is plotted.

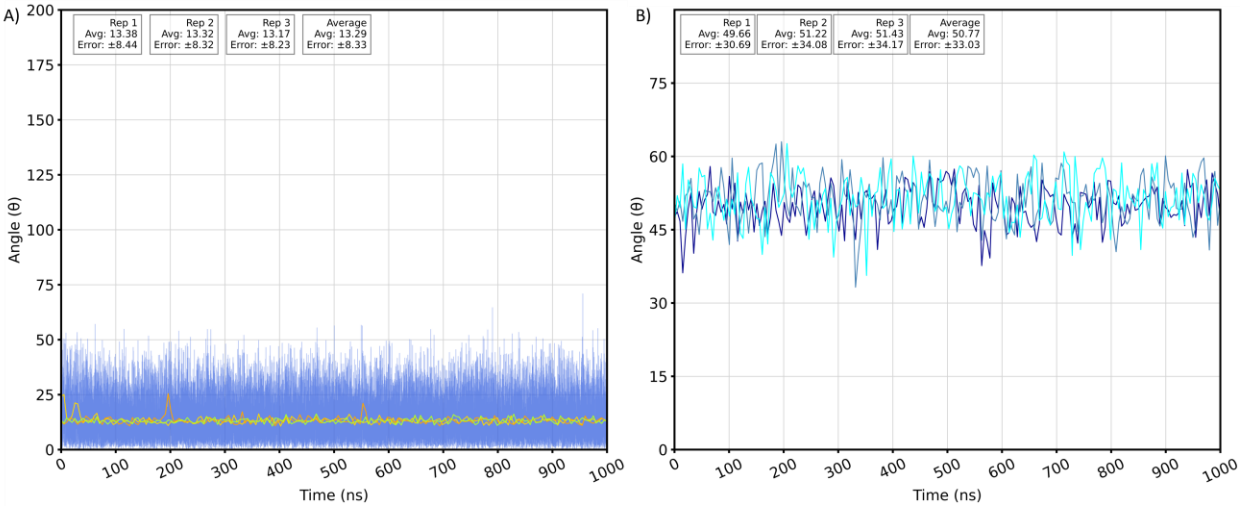

Figure S93. Data for the *Narl*12 PhOH6HI opposite C. A) The co-planar angle between the indanone and phenol moiety, with the 5 ns running average plotted on top of the raw data (blue). B) The dihedral angle of the rotatable σ-bond bridging the two aryl moieties of the PhOH6HI. The running average of every 5 ns is plotted.

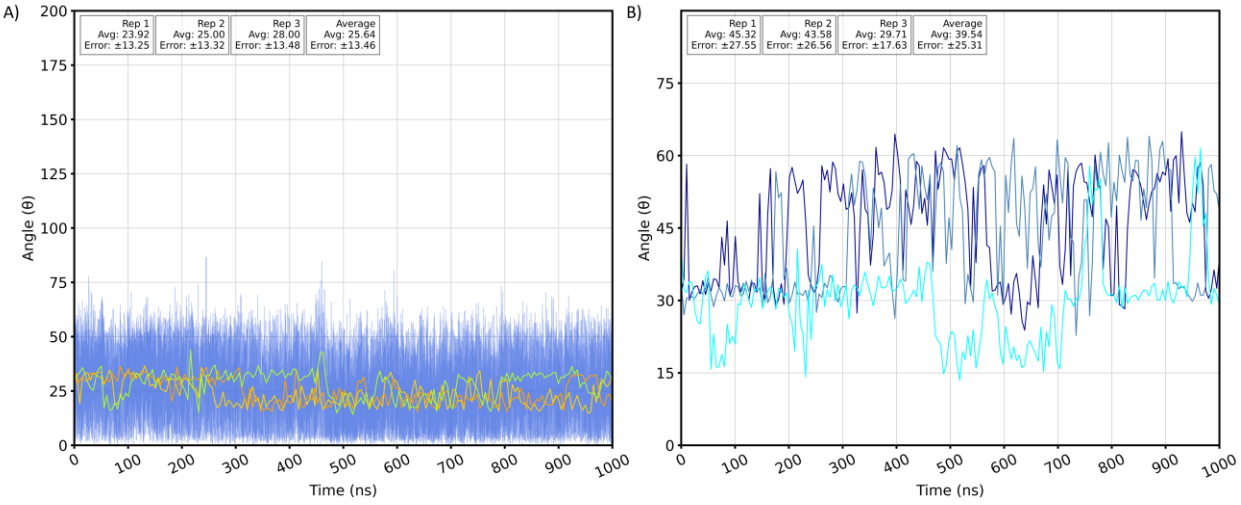

Figure S94. Data for the *Narl*12 PhOH6HI flanked by dG6 and dG8. A) The co-planar angle between the indanone and phenol moiety, with the 5 ns running average plotted on top of the raw data (blue). B) The dihedral angle of the rotatable σ-bond bridging the two aryl moieties of the PhOH6HI. The running average of every 5 ns is plotted.

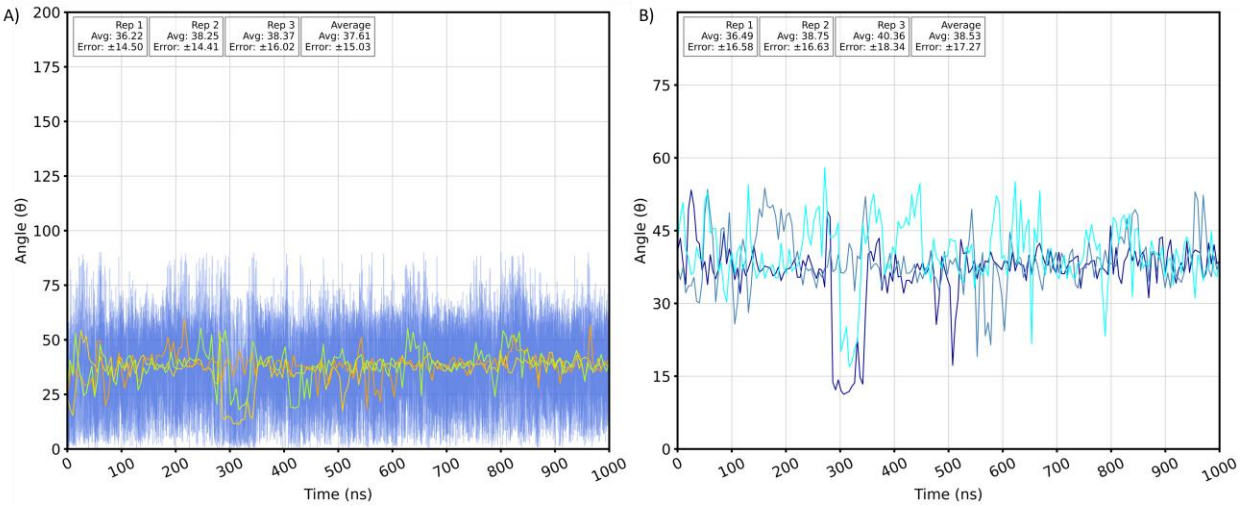

Figure S95. Data for the TBA15 PhOH6HI opposite C. A) The co-planar angle between the indanone and phenol moiety, with the 5 ns running average plotted on top of the raw data (blue). B) The dihedral angle of the rotatable σ-bond bridging the two aryl moieties of the PhOH6HI. The running average of every 5 ns is plotted.

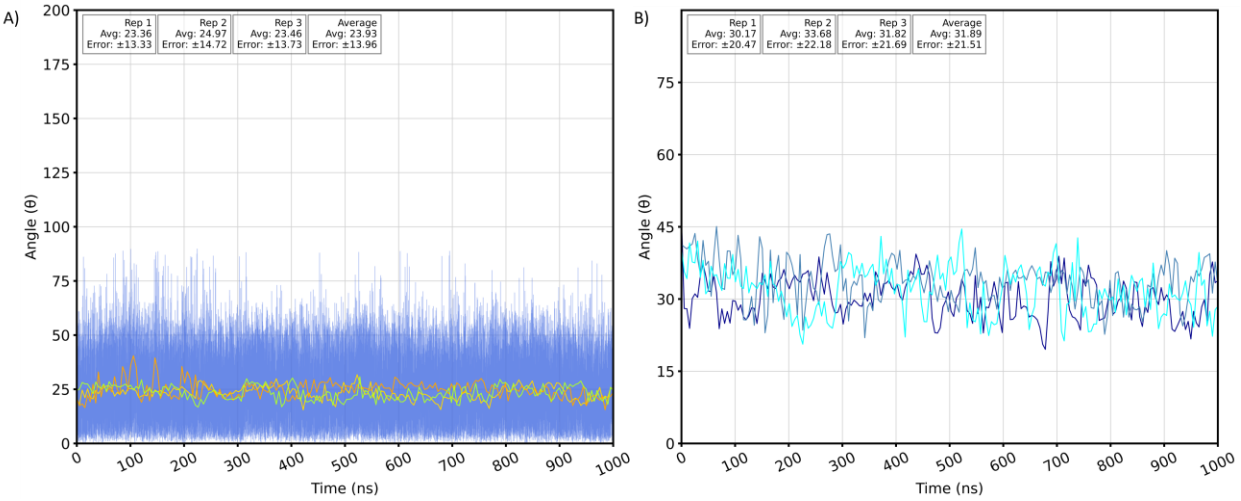

Figure S96. Data for the TBA15 GQ with K^+ system. A) The co-planar angle between the indanone and phenol moiety, with the 5 ns running average plotted on top of the raw data (blue). B) The dihedral angle of the rotatable σ-bond bridging the two aryl moieties of the PhOH6HI. The running average of every 5 ns is plotted.

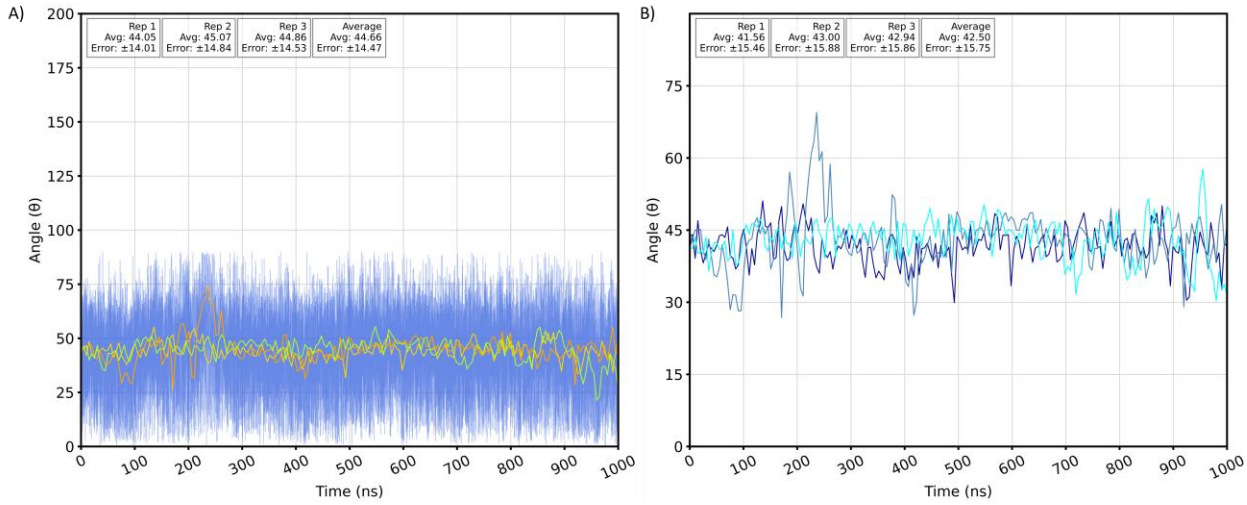

Figure S97. Data for the TBA15 PhOH6HI flanked by T_L opposite C. A) The co-planar angle between the indanone and phenol moiety, with the 5 ns running average plotted on top of the raw data (blue). B) The dihedral angle of the rotatable σ-bond bridging the two aryl moieties of the PhOH6HI. The running average of every 5 ns is plotted.

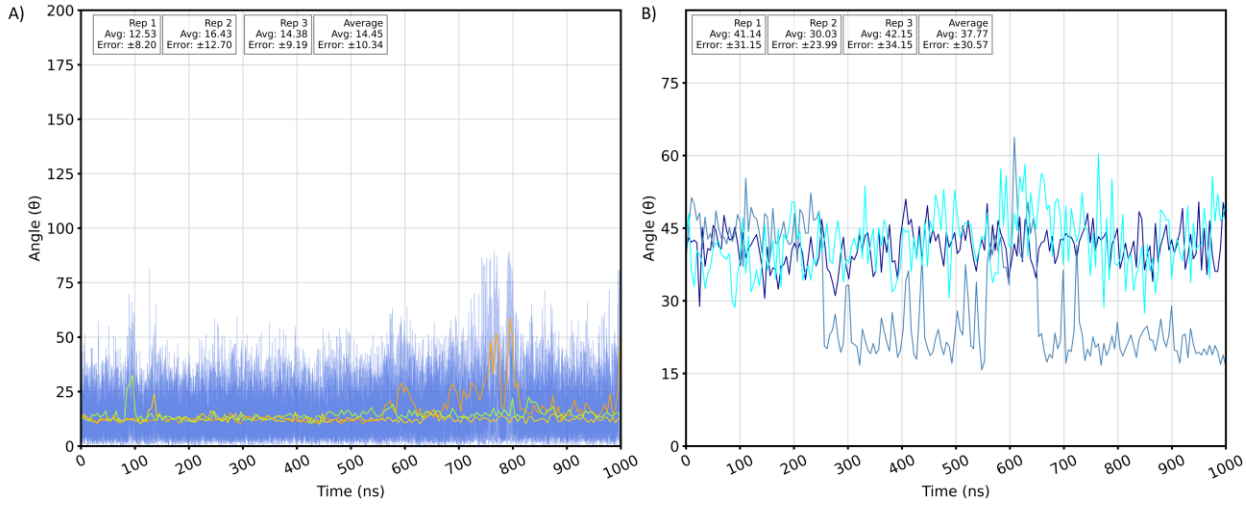

Figure S98. Data for the TBA15 PhOH6HI opposite C interstrand flanked by A_L. A) The co-planar angle between the indanone and phenol moiety, with the 5 ns running average plotted on top of the raw data (blue). B) The dihedral angle of the rotatable σ-bond bridging the two aryl moieties of the PhOH6HI. The running average of every 5 ns is plotte

References

(1) Russo Krauss, I.; Merlino, A.; Randazzo, A.; Novellino, E.; Mazzarella, L.; Sica, F. High-Resolution Structures of Two Complexes between Thrombin and Thrombin-Binding Aptamer Shed Light on the Role of Cations in the Aptamer Inhibitory Activity. *Nucleic Acids Res* **2012**, *40*, 8119–8128.

(2) GaussView, Version 6, Dennington, Roy; Keith, Todd A.; Millam, John M. Semichem Inc., Shawnee Mission, KS, 2016.

(3) DeLano, W. L. PyMOL: An Open-Source Molecular Graphics. *CCP4 Newslet. Pro. Crystallogr.* **2002**, *40*, 82–92.

(4) Van Riesen, A. J.; Fadock, K. L.; Deore, P. S.; Desoky, A.; Manderville, R. A.; Sowlati-Hashjin, S.; Wetmore, S. D. Manipulation of a DNA Aptamer–Protein Binding Site through Arylation of Internal Guanine Residues. *Org Biomol Chem* **2018**, *16*, 3831–3840.

(5) Johnson, R. E.; Murray, M. T.; Bycraft, L. J.; Wetmore, S. D.; Manderville, R. A. A Modular Aldol Approach for Internal Fluorescent Molecular Rotor Chalcone Surrogates for DNA Biosensing Applications. *Chem Sci* **2023**, *14*, 4832–4844.

(6) Peng, T.; Chang, T.-M.; Sun, X.; Nguyen, A. V; Dang, L. X. Development of Ions-TIP4P-Ew Force Fields for Molecular Processes in Bulk and at the Aqueous Interface Using Molecular Simulations. *J Mol Liq* **2012**, *173*, 47–54.

(7) Rappe, A. K.; Casewit, C. J.; Colwell, K. S.; Goddard, W. A. I. I. I.; Skiff, W. M. UFF, a Full Periodic Table Force Field for Molecular Mechanics and Molecular Dynamics Simulations. *J Am Chem Soc* **1992**, *114*, 10024–10035.

(8) Becke, A. D. Density-functional Thermochemistry. III. The Role of Exact Exchange. *J Chem Phys* **1993**, *98*, 5648–5652.

(9) Grimme, S.; Ehrlich, S.; Goerigk, L. Effect of the Damping Function in Dispersion Corrected Density Functional Theory. *J Comput Chem* **2011**, *32*, 1456–1465.

(10) Ditchfield, R.; Hehre, W. J.; Pople, J. A. Self-Consistent Molecular-Orbital Methods. IX. An Extended Gaussian-Type Basis for Molecular-Orbital Studies of Organic Molecules. *J Chem Phys* **1971**, *54*, 724–728.

(11) Gaussian 16, R. C. 01, F. M. J. ; T. G. W. ; S. H. B. ; S. G. E. ; R. M. A. ; C. J. R. ; S. G. ; B. V. ; P. G. A. ; N. H. ; L. X. ; C. M. ; M. A. V. ; B. J. ; J. B. G. Gaussian.

(12) Vanquelef, E.; Simon, S.; Marquant, G.; Garcia, E.; Klimerak, G.; Delepine, J. C.; Cieplak, P.; Dupradeau, F.-Y. R.E.D. Server: A Web Service for Deriving RESP and ESP Charges and Building Force Field Libraries for New Molecules and Molecular Fragments. *Nucleic Acids Res* **2011**, *39*, W511–W517.

(13) Wang, J.; Wolf, R. M.; Caldwell, J. W.; Kollman, P. A.; Case, D. A. Development and Testing of a General Amber Force Field. *J Comput Chem* **2004**, *25*, 1157–1174.

(14) D.A. Case, H. M. A. K. B. I. Y. B.-S. J. T. B. S. R. B. D. S. C. T. E. C. I. G. A. C. V. W. D. C. T. A. D. R. E. D. G. Amber22.

(15) Horn, H. W.; Swope, W. C.; Pitera, J. W.; Madura, J. D.; Dick, T. J.; Hura, G. L.; Head-Gordon, T. Development of an Improved Four-Site Water Model for Biomolecular Simulations: TIP4P-Ew. *J Chem Phys* **2004**, *120*, 9665–9678.

(16) Schmit, J. D.; Kariyawasam, N. L.; Needham, V.; Smith, P. E. SLTCAP: A Simple Method for Calculating the Number of Ions Needed for MD Simulation. *J Chem Theory Comput* **2018**, *14*, 1823–1827.

(17) Kräutler, V.; van Gunsteren, W. F.; Hünenberger, P. H. A Fast SHAKE Algorithm to Solve Distance Constraint Equations for Small Molecules in Molecular Dynamics Simulations. *J Comput Chem* **2001**, *22*, 501–508.

(18) Davidchack, R. L.; Handel, R.; Tretyakov, M. V. Langevin Thermostat for Rigid Body Dynamics. *J Chem Phys* **2009**, *130*, 234101.

(19) Berendsen, H. J. C.; Postma, J. P. M.; van Gunsteren, W. F.; DiNola, A.; Haak, J. R. Molecular Dynamics with Coupling to an External Bath. *J Chem Phys* **1984**, *81*, 3684–3690.

(20) Chai, J.-D.; Head-Gordon, M. Long-Range Corrected Hybrid Density Functionals with Damped Atom–Atom Dispersion Corrections. *Physical Chemistry Chemical Physics* **2008**, *10*, 6615–6620.

(21) Weigend, F.; Ahlrichs, R. Balanced Basis Sets of Split Valence, Triple Zeta Valence and Quadruple Zeta Valence Quality for H to Rn: Design and Assessment of Accuracy. *Physical Chemistry Chemical Physics* **2005**, *7*, 3297–3305.

(22) Marenich, A. V; Cramer, C. J.; Truhlar, D. G. Universal Solvation Model Based on Solute Electron Density and on a Continuum Model of the Solvent Defined by the Bulk Dielectric Constant and Atomic Surface Tensions. *J Phys Chem B* **2009**, *113*, 6378–6396.

(23) Caricato, M.; Mennucci, B.; Tomasi, J.; Ingrosso, F.; Cammi, R.; Corni, S.; Scalmani, G. Formation and Relaxation of Excited States in Solution: A New Time Dependent Polarizable Continuum Model Based on Time Dependent Density Functional Theory. *J Chem Phys* **2006**, *124*, 124520.

(24) Zhao, Y.; Truhlar, D. G. The M06 Suite of Density Functionals for Main Group Thermochemistry, Thermochemical Kinetics, Noncovalent Interactions, Excited States, and Transition Elements: Two New Functionals and Systematic Testing of Four M06-Class Functionals and 12 Other Functionals. *Theor Chem Acc* **2008**, *120*, 215–241.

(25) Neese, F. The ORCA Program System. *WIREs Computational Molecular Science* **2012**, *2*, 73–78.

(26) Neese, F. Software Update: The ORCA Program System—Version 5.0. *WIREs Computational Molecular Science* **2022**, *12*, e1606.

(27) Neese, F.; Wennmohs, F.; Becker, U.; Riplinger, C. The ORCA Quantum Chemistry Program Package. *J Chem Phys* **2020**, *152*, 224108.

(28) Bannwarth, C.; Ehlert, S.; Grimme, S. GFN2-XTB—An Accurate and Broadly Parametrized Self-Consistent Tight-Binding Quantum Chemical Method with Multipole Electrostatics and Density-Dependent Dispersion Contributions. *J Chem Theory Comput* **2019**, *15*, 1652–1671.

(29) Stahn, M.; Ehlert, S.; Grimme, S. Extended Conductor-like Polarizable Continuum Solvation Model (CPCM-X) for Semiempirical Methods. *J Phys Chem A* **2023**, *127*, 7036–7043.

(30) Barone, V.; Cossi, M. Quantum Calculation of Molecular Energies and Energy Gradients in Solution by a Conductor Solvent Model. *J Phys Chem A* **1998**, *102*, 1995–2001.

(31) Neese, F. An Improvement of the Resolution of the Identity Approximation for the Formation of the Coulomb Matrix. *J Comput Chem* **2003**, *24*, 1740–1747.

(32) Helmich-Paris, B.; de Souza, B.; Neese, F.; Izsák, R. An Improved Chain of Spheres for Exchange Algorithm. *J Chem Phys* **2021**, *155*, 104109.

(33) Weigend, F. Accurate Coulomb-Fitting Basis Sets for H to Rn. *Physical Chemistry Chemical Physics* **2006**, *8*, 1057–1065.